Ludwig-Maximilians-Universität München
Fakultät für Physik

Master Thesis

Alignment reconstruction of Micromegas detectors of the ATLAS New Small Wheel Upgrade

Alignierung von Micromegas Detektoren für das ATLAS New Small Wheel Upgrade

Fabian Vogel

Betreuer
Prof. Dr. Otmar Biebel

September 8, 2020

Abstract

For the upcoming New Small Wheel Upgrade of the ATLAS detector system large area MICROmesh GAseous Structure (Micromegas) detectors are developed and built. These detectors have to provide a position resolution of $< 100\,\mu$m. The detectors consist of four active detection volumes. To ensure this resolution an alignment of the modules with a precision of the same order is necessary. This is done for the alignment of single readout layers and for the alignment of the readout layers with respect to each other.
For quality control the alignment of the modules has to be reconstructed. The first approach is an optical alignment reconstruction using so-called Rasmasks. These masks have nominal positions on the readout layers and by measuring their position using optical devices (Contact-CCDs or a telecentric camera) deviations of 7 μm can be resolved. Comparisons of the reconstructions using the different devices are performed. Investigations on the thermal expansion of the readout panels are done by reconstructing the Rasmask positions at different temperatures.
A second approach is the alignment reconstruction by muon tracks in the Cosmic Ray Facility (CRF). Reference tracks reconstructed by Monitored Drift Tubes (MDTs) are compared to the measured positions inside the Micromegas detector placed in between the reference chambers. The track is reconstructed with a resolution of 20 μm.
Studies on the comparability of the optical alignment reconstruction and the alignment reconstruction using cosmic muons is done for single layers and for the alignment of multiple layers with respect to each other.

Kurzfassung

Für das anstehende New Small Wheel Upgrade des ATLAS Detektorsystems werden großflächige MICROmesh GAseous Structure (Micromegas) Detektoren entwickelt und gebaut. Diese Detektoren haben eine Positionsauflösung von besser als 100 μm. Ein Detektor besteht aus vier aktiven Detektorvolumina. Um die Positionsauflösung für alle Lagen zu garantieren, ist eine präzise Alignierung in der selben Größenordnung notwendig. Dies wird sowohl für eine Detektorlage als auch für die Alignierung der Lagen zueinander gemacht.
Zur Qualitätskontrolle ist eine Rekonstruktion dieser Alignierung notwendig. Der erste Ansatz basiert auf einer optischen Rekonstruktionsmethode unter Verwendung sogenannter Rasmasks. Diese besitzen nominelle Positionen auf den Ausleselagen. Ihre tatsächlichen Positionen werden unter Verwendung optischer Geräte (Kontakt-CCDs oder telezentrischer Objektive) mit einer Genauigkeit von 7 μm aufgelöst. Die Vergleichbarkeit der beiden optischen Methoden wird geprüft. Ebenso werden Studien zur thermischen Ausdehnung der Auslesepanele durch Rekonstruktion der Rasmask Positionen bei unterschiedlichen Temperaturen durchgeführt.
Ein weiterer Ansatz zur Rekonstruktion der Alignierung ist die Verwendung von Myonspuren in einer Cosmic Ray Facility (CRF). Durch Monitored Drift Tubes (MDTs) rekonstruierte Referenzspuren werden mit den in den Micromegas Modulen gemessenen Punkten verglichen. Diese Module werden zwischen zwei Referenzkammern platziert. Die kombinierte Referenzspur kann mit einer Genauigkeit von 20 μm bestimmt werden.
Studien zur Vergleichbarkeit der Rekonstruktion mit optischen Methoden und mit kosmischen Myonen werden sowohl für die Alignierung in einer Ausleselage als auch für die Alignierung der Lagen zueinander durchgeführt.

Table of Contents

Chapter 1

Motivation

The Standard Model is the best approach of describing three out of four fundamental forces today, yet it lacks the capability to describe subjects like dark matter, black holes as well as the gravitational force. Therefore many theoretical frameworks of physics beyond the Standard Model (BSM) are emerging. Hence experimental physicists constantly improve or invent methods to probe BSM physics. Particle physicists at CERN[1] for example raise the centre of mass energy of the particles in collider experiments as well as the instantaneous luminosity, a parameter describing the flux density of particle events at the collision point [see **Herr and Muratori 2006**], to increase the chances of discovering new physics.

A sketch of the Large Hadron Collider (LHC) complex in Geneva (Switzerland) with its main experiments is shown in figure 1.1. It collides two proton beams with a total centre-of-mass energy of $\sqrt{s} = 13\,\mathrm{TeV}$ and an instantaneous luminosity of $\mathcal{L} = 2 \times 10^{-34}\,\mathrm{cm^{-2}s^{-1}}$ (for Run 2, 2015-2018) [**Steerenberg 2018**]. For the upcoming years an upgrade of the LHC to a **H**igh **L**uminosity-LHC (HL-LHC) is planned, with a final centre-of-mass energy of $\sqrt{s} = 14\,\mathrm{TeV}$ and an instantaneous luminosity of $\mathcal{L} = 5 - 7.5 \times 10^{-34}\,\mathrm{cm^{-2}s^{-1}}$ in 2027 [**CERN 2020c**]. These luminosities exceed the design value of the LHC ($\mathcal{L} = 1 \times 10^{-34}\,\mathrm{cm^{-2}s^{-1}}$) [**Gillies 2011**] which results in issues for some of the components of the four large detector experiments (ATLAS, CMS, ALICE, LHC-b) of the LHC, due to the high particle flux.

This thesis focuses on the ATLAS (**A** **T**oroidal **L**HC **A**pperatu**S**) experiment. The inner endcaps of the muon spectrometer of the ATLAS detector system, which are used as a $4\,\pi$ muon tracker along the beam axis, are not capable of correct position reconstruction at such a high luminosity, without losing too many particle collisions or having a very high fake rate ($\approx 90\%$). An upgrade of these muon endcaps is necessary and the production of the new detector modules is currently finalising. Scientists from many different countries collaborate in this production process for a specific type of muon chambers which are part of the **N**ew **S**mall **W**heel (NSW) upgrade (see figure 1.2). Detector modules of four different types (Germany (SM2), Italy (SM1), France (LM1), Russia and Greece (LM2)) are produced separately to fit the wheel structure.

[1] Conseil Européen pour la Recherche Nucléaire

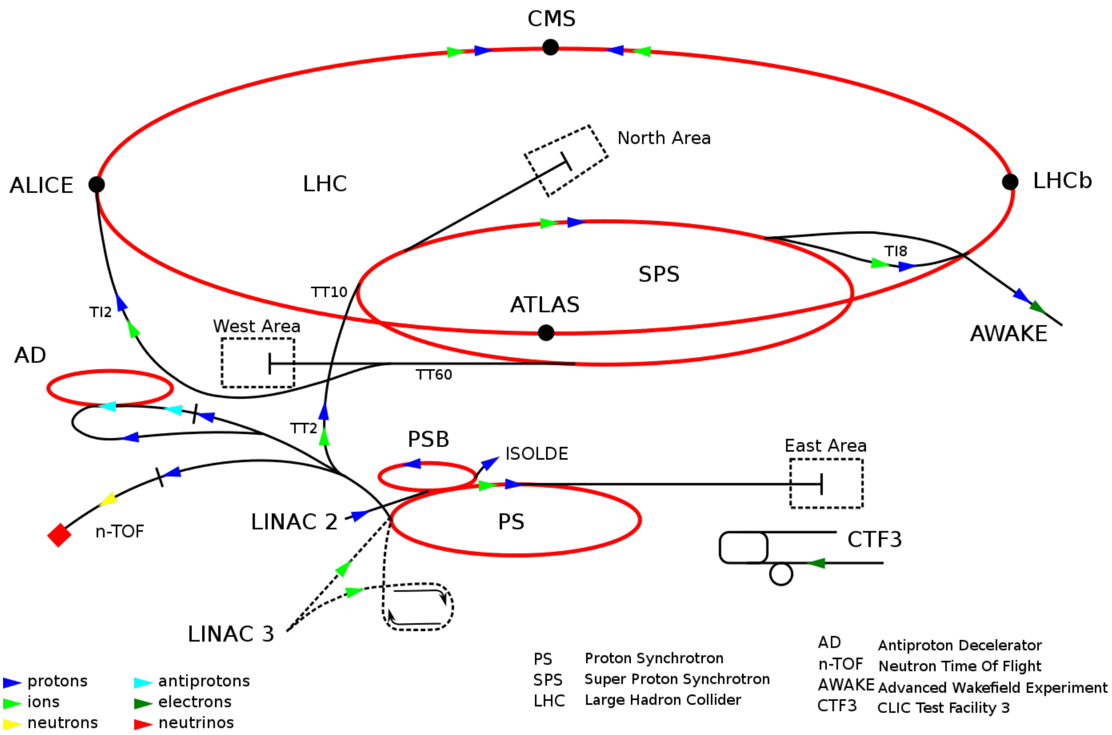

Fig. 1.1: Sketch of the layout of the LHC accelerator complex. The main experiments at the LHC are ALICE, LHCb, CMS and ATLAS[2].

The former muon tracker consisting of **M**onitored **D**rift **T**ubes (MDTs) and **C**athode **S**trip **C**hambers (CSC) is replaced by so-called Micromegas (**MIC**ro-**ME**sh **GA**seous **S**tructure) and small-strip **T**hin **G**ap **C**hambers (sTGC) quadruplets, that fulfil high rate stability at this instantaneous luminosity. To ensure the single layer design resolution of $< 100\ \mu\text{m}$ for these large area ($\approx 2 - 3\text{m}^2$) Micromegas detectors a precise alignment in the sub $100\ \mu\text{m}$ order is necessary [see **Stelzer 2016**]. Another challenge is the alignment of the four readout layers with respect to each other. During the production process misalignments are introduced that have to be accounted for, when the NSW gets integrated in the ATLAS detector.
The assembly as well as the quality control of the panels used for particle reconstruction inside of the **S**mall **M**icromegas 2 (SM2) modules take place at Garching near Munich. In this thesis the methods are tested for accuracy. The first alignment method is purely based on optical measurements and geometrical reconstruction using a telecentric camera as well as a **C**ontact-**C**harged **C**oupled **D**evice (C-CCD) to measure encoded chessboard-like masks, that are printed on the readout layers. The second alignment reconstruction method is using cosmic muons ($\sim$ GeV) in a Cosmic Ray Facility (CRF), where the reconstructed hit in the Micromegas is compared with a reference track, that is reconstructed using a scintillator hodoscope and MDTs. This thesis focuses on the alignment of the SM2 modules using these methods during the production in Garching. A comparison of the alignment reconstructions using cosmic muons with the optical alignment reconstructions is included.

[2]figure taken from Wikimedia, Author Forthommel, `https://commons.wikimedia.org/wiki/File:Cern-accelerator-complex.svg`, visited on April 21, 2020

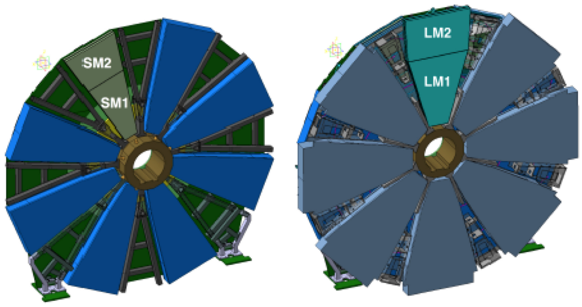

(a) Sketch of the layout of the New Small Wheel, indicating the four different Micromegas quadruplets. The large modules (LM) are placed on the outer side and the small modules (SM) on the inner side of the detector system (taken from [**Bianco 2016**]).

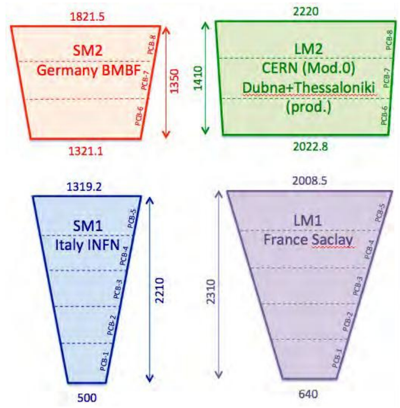

(b) Sketch showing the layouts of the different quadruplets as well as the associated production sites (taken from [**Sampsonidis 2017**]).

Fig. 1.2: Sketches of the layout and participating countries of the NSW upgrade. This thesis focuses on the **S**mall **M**icromegas 2 (SM2) modules built in Germany.

Chapter 2

ATLAS and the New Small Wheel Upgrade

2.1 The ATLAS experiment

The ATLAS experiment is one of the four large detector systems at the LHC located at CERN near Geneva (Switzerland). One of ATLAS main goals is the detection of particles and decays hinting for BSM physics. CMS, LHC-b and ALICE are the three other main experiments at the LHC. This thesis focuses on ATLAS and the New Small Wheel Upgrade of its muon spectrometer.

2.1.1 Layout of the ATLAS detector system

ATLAS has a toroidal shape for measurements in 4π with multiple detector layers. Using these, particles can be identified and their energy, momentum as well as their track to the interaction vertex can be reconstructed. Figure 2.1 shows an overview of the detector system. Starting from the most inner part, it consists of the beam pipe, the inner detector, the calorimeters and the magnet system for track bending of charged particles. The most outer part comprises the muon spectrometer.

The inner detector contains three different parts. The pixel detector is the closest one to the beam pipe and is designed for extremely precise tracking close to the interaction point with a pixel size of $14\times115\ \mu\mathrm{m}^2$. The semiconductor tracker of the inner detector primarily tracks particles emitted perpendicularly to the beam with an resolution in the same order of the pixel detector. The last part is the transition radiation tracker mainly being used as a particle identification system, but it also provides a coarse position information [**CERN 2020d**].

The ATLAS detector system contains two different calorimeters, the electromagnetic calorimeter (for photons and charged particles) and the hadronic calorimeter (for strongly interacting particles, e.g. hadrons). By absorbing the particle energy in high density metal, the showers characteristic shape for each particle can be used to determine the initial energy. These calorimeters stop almost all currently discovered particles, except muons and neutrinos [**CERN 2020a**]. Between the inner detector and the calorimeters is the inner solenoidal magnetic system for particle track bending. An additional toroidal magnet system lies within the muon spectrometer. Using the fact that the track bending is caused by the Lorentz force, which is proportional to the velocity, a momentum determination of the charged particles can be done. High momentum particles are effected less pronounced than low momentum particles.

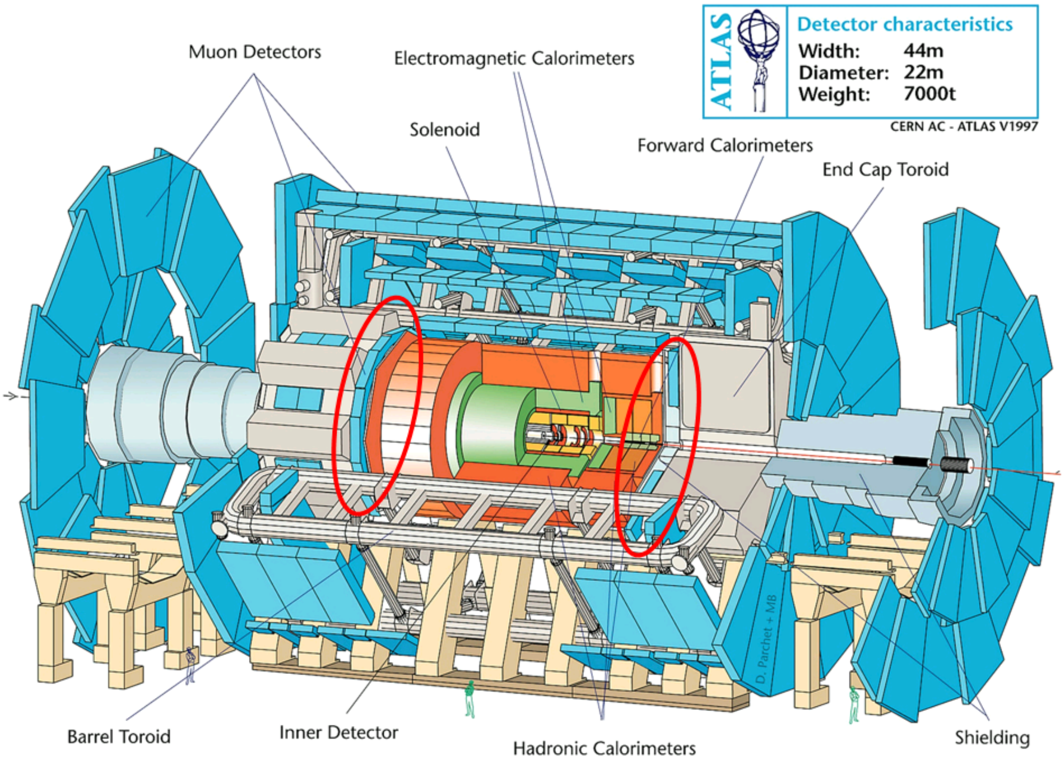

Fig. 2.1: Sketch of the layout of the ATLAS experiment at the LHC. It consists of a beam pipe, an inner detector system, calorimeters, a magnet system and a muon spectrometer. All these components provide information for particle identification, position reconstruction and energy determination. The red ellipses indicate the location of the Small Wheel of the endcap system, which gets replaced by the New Small Wheel[1].

A barrel surrounding the calorimeters and the inner detector system forms together with the four big and two small wheels at the two endcaps of the toroidal structure the muon spectrometer. It consists of four different technologies: The thin gap chambers (endcap trigger), the cathode strip chambers (position measurement in the inner part of the small wheels with a spatial resolution of ≈ 60 µm), the monitored drift tubes (position measurement of muon tracks in the barrel and the endcaps ≈ 80 µm) and the resistive plate chambers (barrel trigger **[CERN 2020b]**).

2.1.2 New Small Wheel Upgrade and muon track reconstruction along the beam axis

During the New Small Wheel Upgrade the Small Wheel (see figure 2.1) will be replaced by a new trigger and track reconstruction system. Due to the higher luminosity and the higher particle background the efficiency of the currently built-in MDTs will decrease by 35%, because of slowly

[1] figure taken from CERN document server, Layout of ATLAS, `https://cds.cern.ch/record/39038?ln=de`, visited on April 21, 2020

drifting ions close to their central wires [**Kawamoto et al. 2013, p.16**]. They are replaced by **M**icromegas **M**odules (MM) being able to handle these high backgrounds and thus reducing the fake triggers. In addition new **s**mall-strip **T**hin **G**ap **C**hambers (sTGC) are implemented which are mainly used as a trigger system. To maximise the distance between two sTGCs for an increased track angle resolution, the detectors of the NSW are arranged in a sandwich structure of the form sTGC-MM-MM-sTGC [**Kawamoto et al. 2013, p.20**]. This layering is shown in detail in A.1 of the appendix A. For a discrimination between correct and fake triggers the reconstructed tracks of both wheels are taken into account. Coincidental triggers with trajectories pointing towards the interaction point (IP) are the main exclusion criteria for the determination of a candidate particle track. Figure 2.2 illustrates this principle. The Big Wheel trigger reconstructs all three particle tracks (A, B, C) as possible candidates. The coincidence trigger prerequisite excludes the particle tracks B and C. To ensure a correct particle track reconstruction of the NSW, a precise alignment ($<100\,\mu$m) of the used detectors is indispensable.

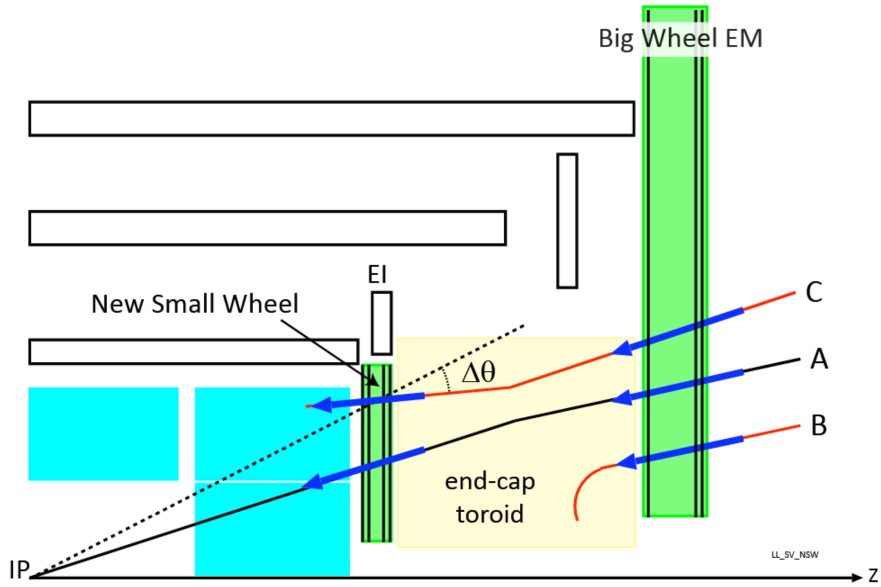

Fig. 2.2: Sketch of the layout of a quarter of the ATLAS muon trigger system containing the small and big wheel.Triggers obtained from the large wheel are compared to the track reconstruction done by the small wheel and only tracks that are reconstructed to originate from the interaction point (IP) by both wheels are used for analysis (Track A in the picture) other tracks that origin from a different location are dismissed (Track B and C) [**Kawamoto et al. 2013, p.119**].

2.2 The SM2 Micromegas detector

The Micromegas (**MIC**ro-**ME**sh **GA**seous **S**tructure) detector was developed in 1996 by Y. Geometries and G. Chapeau as a high gain gaseous detector with high accuracy, high rate capability, excellent timing properties and robustness [**Giomataris, Charpak, et al. 1996**]. Its signal length is in the order of 100 ns with a spatial resolution below 100 μm. These properties constitute the Micromegas detector as the perfect candidate for the NSW upgrade.

2.2.1 Energy loss of particles in matter

The mean energy loss of charged particles in matter is well-described by the "Bethe-Bloch formula" [**Tanabashi et al. 2018, p.447**]. Symbol definitions are given in table 2.1.

$$\left\langle -\frac{dE}{dx}\right\rangle = Kz^2 \frac{Z}{A}\frac{1}{\beta^2}\left[\frac{1}{2}\ln\frac{2m_e c^2\beta^2\gamma^2 W_{\max}}{I^2} - \beta^2 - \frac{\delta(\beta\gamma)}{2}\right] \tag{2.1}$$

The gas ionisation process in Micromegas detectors according to the Bethe-Bloch formula is the detection mechanism for traversing ionising particles. Figure 2.3 shows the mass stopping power of muons in copper as a function of $\beta\gamma$. For very small $\beta\gamma$ in the order of $0.001 - 0.01$ is the mass stopping power maximal. In the region between $1 - 1000$ the stopping power reaches a plateau. The muons are minimal ionising for a ($\beta\gamma \approx 3 - 4$). For thin detector layers the minimum ionising energy loss follows a Landau distribution. This results to large variation around the mean energy loss value due to large energy transfer to target electrons. In this case the momentum transfer is maximal. The energy loss distribution approaches a Gaussian distribution for thicker layers [**Kleinknecht 2005, p.14ff**].

parameter	definition	unit/value
K	$2\pi\rho {r_e}^2 m_e N_A$	eV/m
ρ	mass density	g/m^3
$m_e c^2$	electron mass multiplied with c^2	0.511 MeV
r_e	classical electron radius	$1.818 \cdot 10^{-15}$ m
N_A	Avogadro constant	$6.022 \cdot 10^{23}$ 1/mol
Z, A	atomic number, mass number	1
z	particle charge	1
$W_{\max} = \frac{2m_e c^2\beta^2\gamma^2}{1+2\gamma\frac{m_e}{M}+(\frac{m_e}{M})^2}$	maximum energy transfer in a single collision	eV
M	particle mass	MeV/c^2
$\beta = \frac{v}{c}$	velocity of the particle over c	1
$\gamma = \frac{1}{\sqrt{1-\beta^2}}$	Lorentz factor	1
δ	density correction	1

Table 2.1: Parameters of the Bethe-Bloch formula.

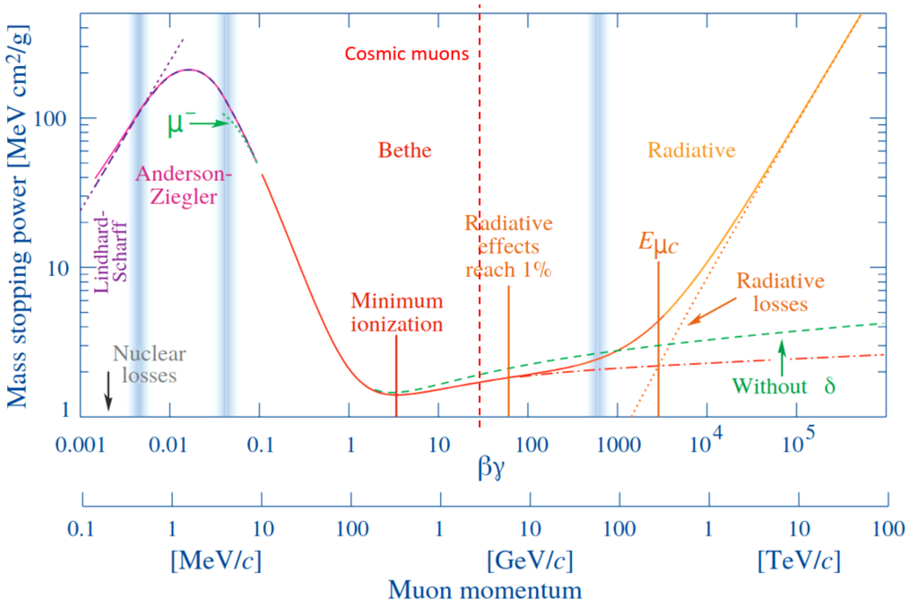

Fig. 2.3: The stopping power of muons in copper for different muon momenta and $\beta\gamma$ values. For values of $\beta\gamma$ of about 0.01 the energy loss due to ionisation is maximal. The muons are minimal ionising for a $\beta\gamma$ between $3-4$. For relativistic particles with energies $\geq 100\,\mathrm{GeV}$ radiative losses dominate. Figure taken from [**Tanabashi et al. 2018, p.447**].

2.2.2 Working principle of a Micromegas detector

A Micromegas detector is a gas-filled detector prominently detecting ionising radiation. Since this thesis focuses on the development of muon detectors for the ATLAS NSW upgrade the following part is discussed for the case of incident muons. Figure 2.4 shows the typical layout of a Micromegas detector.

It consists of a non-segmented cathode, a grounded micromesh and a readout anode. The micromesh for the SM2 module has a typical distance of 128 μm to the anode. This gap is called amplification region. To ensure this distance over the whole detector size of $\approx 2\,\mathrm{m}^2$, pillars are used for stabilisation. The readout strips on the anode are printed parallel to each other with a pitch of 425 μm to detect the electron signal. On top of the copper readout strips an additional layer of resistive strips is added as spark protection [**Alexopoulos et al. 2011**]. The electrons for the readout signal are produced by ionisation of the gas inside the detector by traversing muons. The detector is filled with a gas mixture of Ar : CO_2 with a ratio of 93 : 7 vol%. The CO_2 is used for quenching. The distance between the mesh and the cathode is typically 5 mm with an electric field in the range from a few hundred V/cm up to 1 kV/cm. This region is called drift region and it is used for separating the electrons and ions to prevent recombination and guide the electrons towards the mesh. In the amplification region an electric field in the order of $40-50$ kV/cm is applied [**Hertenberger 2016, p.2**]. With an electric field in the amplification region $50-100$ times higher than the drift region, the mesh is transparent to more than 95% of the electrons [**Stelzer 2016, p.1163**]. This strong field accelerates the electrons to such an extent, that secondary ionisation leads to Townsend avalanches. A typical avalanche amplifies the initially created electrons

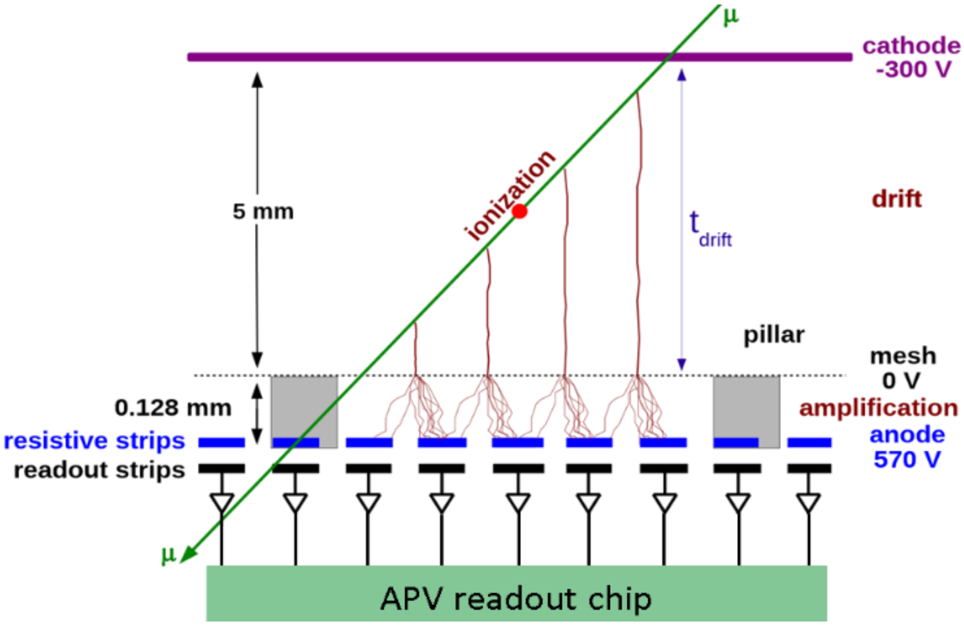

Fig. 2.4: Typical layout of a Micromegas detector; its three planar layers are a cathode, a micromesh and a segmented readout anode. Traversing particles ionise the gas mixture inside the detector, creating electron-ion pairs. Between the cathode and the mesh is a small electric field (few 100 V/cm) to separate ions and electrons. The electric field for amplification between the micro mesh and the readout anode is in the order of $40-50$ kV/cm for the Micromegas of the NSW upgrade [taken from **Lösel 2017**].

by a factor of $5 \cdot 10^3 - 10^4$. Accelerated electrons in the amplification region may not only ionise further atoms, but also excite some to a higher energy state. The deexcitation of those atoms produces photons, that can lead to further ionisation's. This might cause a longer insensibility or dead time of the detector. The quenching gas is used to capture these photons and prevent their further ionisation.

Since the major electron-ion pair production takes place in the amplification region, the deadtime of the detector can be estimated by the drift time of the ions towards the mesh and the subsequent evacuation of positive ions as $\approx$100 ns for the SM2 detectors [**Kawamoto et al. 2013, p.47**].

For one traversing muon typically multiple readout strips are hit. A charge weighting of the hit strips results in a spatial resolution of better than 100 μm per detector layer [**Flierl 2018**].

2.2.3 SM2 module layout

The SM2 modules for the ATLAS NSW upgrade consist of two readout panels and three drift panels. A quadruplet is constructed with four active Micromegas volumes. The inner drift panel, which contains two cathodes and two micromeshes gets sandwiched by the inner layers of the readout panels. For the two outer layers of the readout panels an additional drift region for each readout panel is implemented. This structure is illustrated in figure 2.5. Here also visible are the alignment pins, that ensure precise alignment of the layers with respect to each other. Additionally shown are the pillars and the precise mesh frames which are used to define the distance between anode and mesh and clamp the mesh. The O-ring ensures the gas tightness required for the

operation at ATLAS. To achieve the stiffness of the quadruplet aluminum honeycomb is glued between cathode and anode layers [**Kawamoto et al. 2013**].
As shown in figure 2.6a one readout layer consists of three separate **P**rinted **C**ircuit **B**oards (PCBs). The necessity of three individual boards is due to manufactural limitations whilst the production of the boards. The size of these boards for the SM2 modules is up to 450 mm in one dimension and up to 1900 mm in the other dimension [**Kawamoto et al. 2013, p.50**].

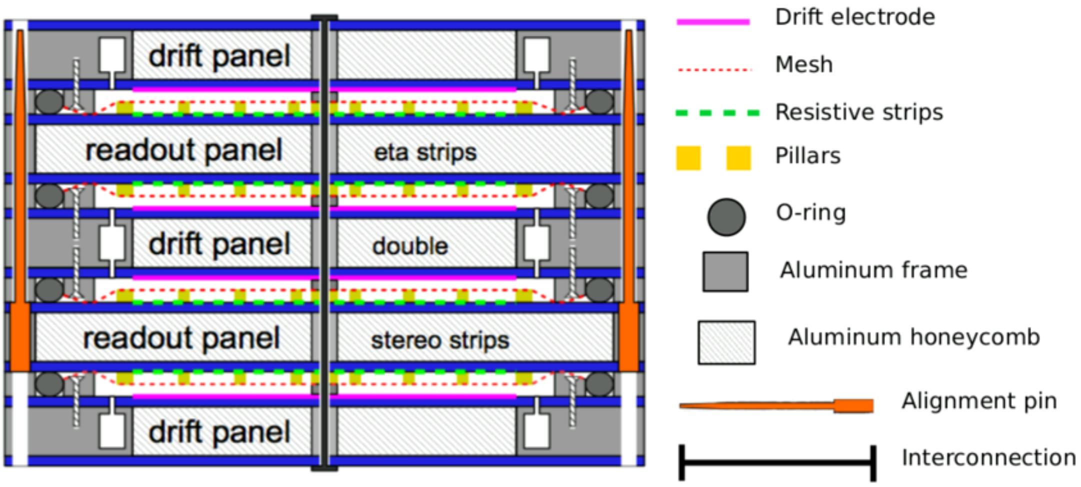

Fig. 2.5: Mechanical structure of an SM2 quadruplet containing four readout layers and four drift layers; layer-to-layer alignment optimisation using alignment pins; the pillars and the mesh frame ensure the distance between readout anode and mesh; O-ring used for gas tightness; honeycomb ensures the stiffness of the module (not to scale; taken from [**Sidiropoulou 2018**]).

During the panel production these three boards are glued together to achieve the desired size of the readout panel of approximately 2 m^2 and its typical trapezoidal shape. The active area of the readout plane with the parallel readout strips is indicated in brown. One PCB contains 1024 readout strips, which results in 3072 strips for a whole readout anode. The inactive border region is drawn in orange. The frontend electronics and cooling is attached to the grey area. For an improved track reconstruction two different types of readout boards are combined. The so-called Eta panels have parallel strips. Boards with readout strips, that are rotated by ±1.5°, are called Stereo boards (see fig. 2.6b). Combining the information of both readout panels gives rise to a precision direction perpendicular to the strips (precision $< 100\,\mu$m) and a non-precision information parallel to the readout strips (precision ≈ 4 mm) [**Flierl 2018, p.98**]. The numbering of the readout boards ($6-8$) comes from the layout of the NSW upgrade, where the SM2 quadruplets are the outer modules of the SM wedge (see 1.2a). The inner part SM1 (Italy) contains the boards with the numbers $1-5$.
The most delicate aspects during production are the planarity of the readout panels, the alignment of the boards in one layer, as well as the alignment of the different panels (readout and drift) with respect to each other. Misalignments that are introduced during the assembly of the quadruplets and the construction of the panels have to be measured and accounted for to ensure a good resolution of the track reconstruction after integration of the NSW.

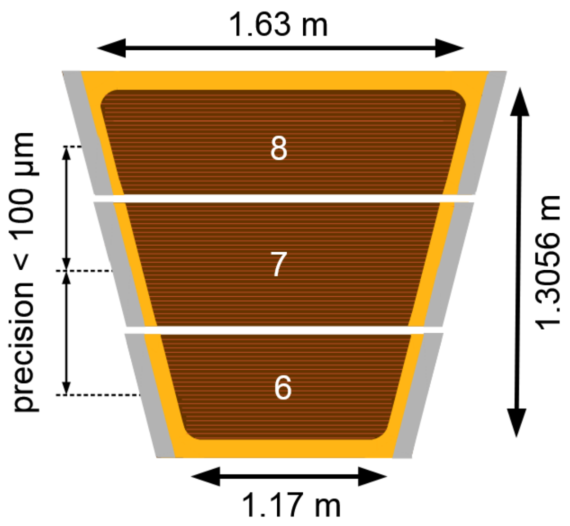

(a) Three individual boards with trapezoidal shape, that are glued together to form one readout anode. The active area with the parallel readout strips is brown. The inactive area is indicated in orange. The grey area contains connections for frontend readout and cooling. An overall alignment with a precision of < 100 µm perpendicular to the strips should be achieved.

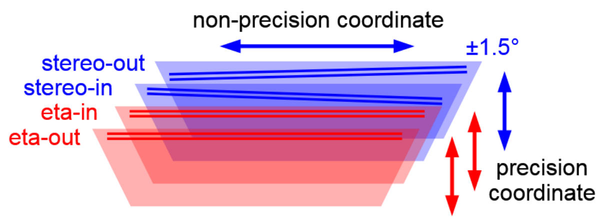

(b) Layering of the four readout planes of one quadruplet. Two different types of PCBs (Eta in read and Stereo in blue) with the orientational difference of the readout strips are indicated.

Fig. 2.6: Sketches of the trapezoidal shape of the readout anodes and their dimensions are shown on the left. The difference between the types of PCBs and their staggering is indicated on the right (taken from [**Herrmann 2019**]).

Chapter 3

Optical in-plane alignment reconstruction methods

The optical alignment is based on so-called Rasmasks (Rasnik masks), which are located on the readout panels. Rasnik is an abbreviation for **R**ed **A**lignment **S**ystem of **NIK**hef [**Hashemi 2007-2017**]. A total of 18 masks (6 per board) are used to determine the alignment of the readout boards. Reconstructing the mask positions and comparing those to their nominal positions results in residuals, that represent deformations, displacements or rotations of individual boards.

3.1 Working principle of the Rasnik alignment system

The minimal alignment system using the Rasnik system consists of an LED, one Rasmask (Rasnik mask), a lens and a CCD (see figure 3.1a). This type of Rasnik alignment is used for the alignment of the MDTs of the ATLAS muon spectrometer.

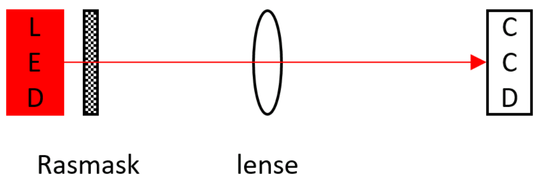

(a) Rasnik alignment for the ATLAS MDTs containing an LED, the Rasmask, a lens and the CCD. The light passes through the mask and is focused on the CCD using a lens.

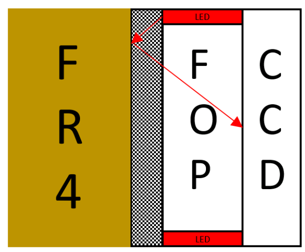

(b) Sketch of the Rasnik setup used for the alignment of the SM2 modules. The emitted light passes through the mask and is reflected on the FR4 surface. The reflected light is the collected by the **F**iber **O**ptical **P**late (FOP) which is directly placed on top of the mask. A Contact-CCD (C-CCD) is formed by the FOP and the CCD.

Fig. 3.1: Different Rasnik alignment methods used for the alignment of the ATLAS MDTs and the SM2 modules.

The Rasmask has a chessboard-like coded structure (see fig. 3.2). The emitted light of the LED's passes through the mask and is focused by a lens to the CCD, that is used for readout. For this method the Rasmasks are made of glass, so the emitted light of the LED's can pass through. For the alignment of the SM2 modules these masks are printed on the readout panels and are made of copper.

3.2 Rasnik and LWDAQ for SM2 alignment

In comparison to the MDT alignment reconstruction, the alignment measurements of the SM2 modules are done by analysing reflected light (see fig. 3.1b). Therefore different optical instruments, e.g. Contact-CCDs (C-CCDs) or a telecentric camera are used to take the Rasnik images. A C-CCD consists of a **F**iber **O**ptical **P**late, that is directly placed on top of the mask, and an CCD. An analysis software to evaluate the images is needed. The Rasnik analysis software of the ATLAS alignment, the **L**ong **W**ire **D**ata **AQ**uisation (LWDAQ) system, also developed at Brandeis University, was provided for this thesis.

Fig. 3.2: Image of the chessboard-like structure of a Rasmask; also shown is the coding for position determination using irregularities every ninth row and column [**Hashemi 2007-2017, p.3**]

A minimum experimental setup for the analysis of SM2 readout panels, containing all vital components, is presented in figure 3.3. The basic components needed are a camera (in this case a C-CCD) and a PC with the installed analysis software. The C-CCD and the PC are connected via a server. To obtain pictures using a C-CCD four LED's are placed around its image sensor (see fig. 3.8b). The camera is placed on top of the masks and the emitted light of the LED's is reflected by the surface behind the masks. The reflected light is collected at the photodiodes of the sensor. The incoming photons are converted by the photoelectric effect to photoelectrons which provide the image information.

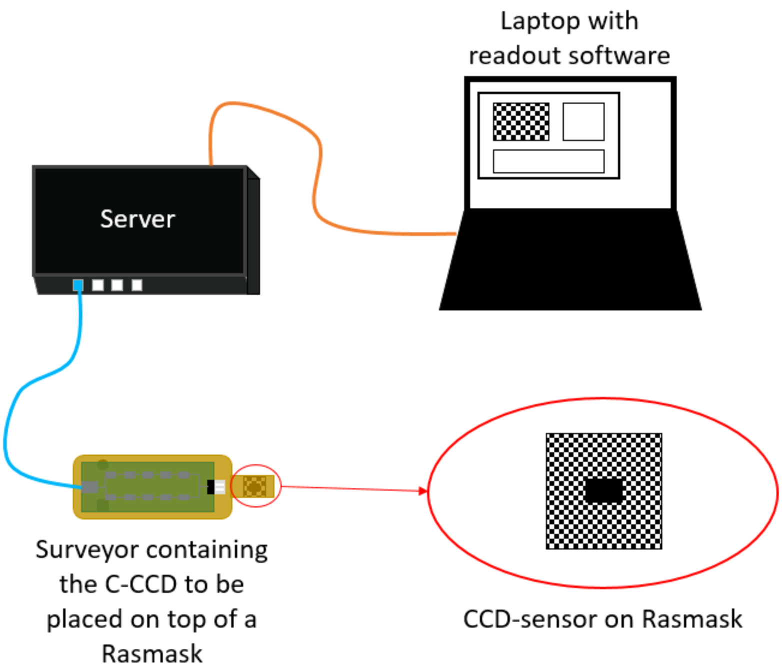

Fig. 3.3: Sketch of the basic setup for measuring and analysing Rasmasks. The surveyor contains a C-CCD for image taking and is placed on top of a Rasmask (indicated as chessboard-like structure at the tip of the surveyor). The surveyor is connected to a server, which is connected to a laptop with the readout software installed.

Figure 3.4 shows the analysis of a single mask using the analysis in LWDAQ. Datapoints (yellow) contain the position information. They are reconstructed using the irregularities of the mask. Crossings (red) of rows containing datapoints are unique and used for position determination of the centre of the image in a global coordinate system. For a correct analysis at least two crossing points are required. An additional problem occurs, if the edges of the image are too dark. White squares may be misidentified as black squares. This results in a misreconstruction of data points on the edges resulting in a wrong analysis. Cropping the image by setting the size of the analysis window leads to better results. On the right side of the analysed picture the I/O information is shown. The option "daq_flash_seconds" sets the exposure time of the four LED's. Variations of this feature lead to better results due to a better lighting.
Below the image is the output of the analysis program. The first entry in the row is the number of the image in this session. At I are the x- and y-position (in μm) of the centre of the image in the mask coordinate system. The light blue square displays the magnification factors in x- and y-direction, followed by the rotation angle (III; in mrad). In the purple square the error of the position measurement (in μm) is reported. Squaresize of the black and white arrays (V; in μm), the pixel size (VI; in μm), the orientation code (OC; VII) and the x-and y-coordinates of the reference point of the C-CCD (VIII; centre of C-CCD in μm) are the last five entries. The orientation code is very important for the transformation of the x- and y- positions to the global coordinate system. For example OC 2 results in an interchange of the x- and y- coordinates with an additional mirroring of the x-axis in the readout software compared to the actual mask coordinates (see figure B.1 in appendix B.1). This procedure is described in detail in chapter 3.4.1.

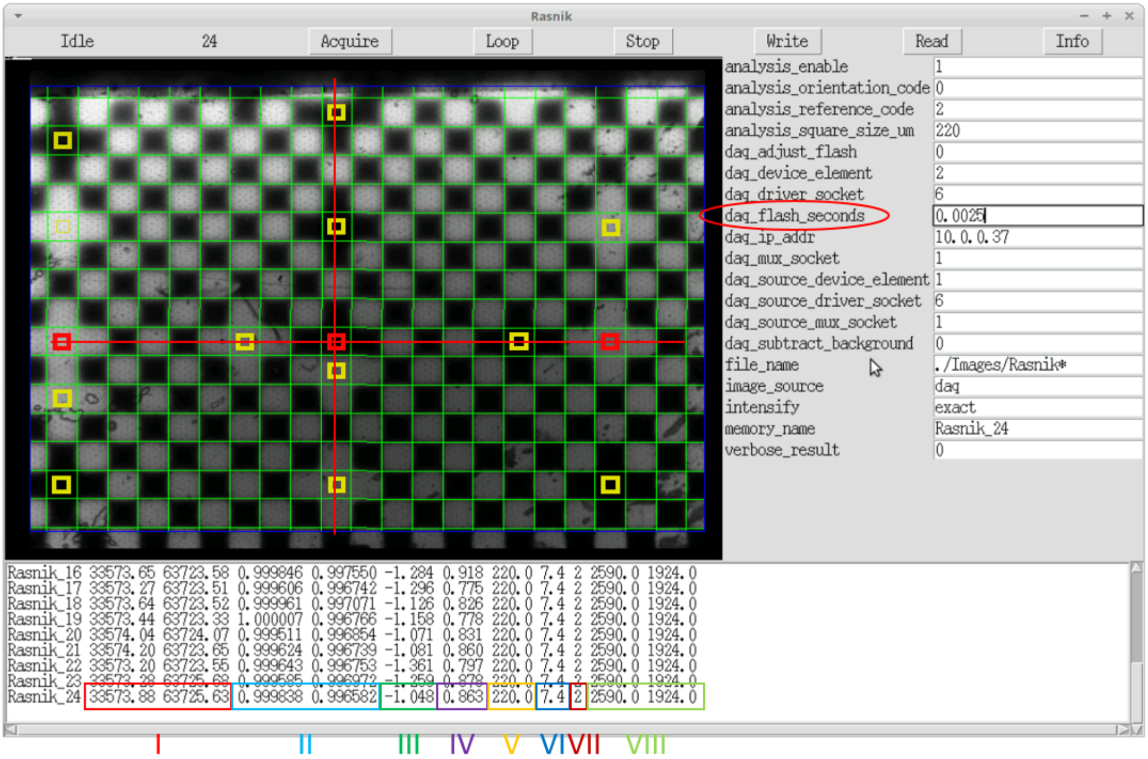

Fig. 3.4: Sketch of an analysed image of a Rasmask and the GUI of the LWDAQ. The yellow, red squares are data/crossing points for analysis/localisation. The output below the image corresponds to the analysed data from the Rasnik analysis software in the LWDAQ (I: measured x-/y position of image centre). On the right is the exposure time and the I/O information.

3.3 Introduction to in-plane alignment reconstruction

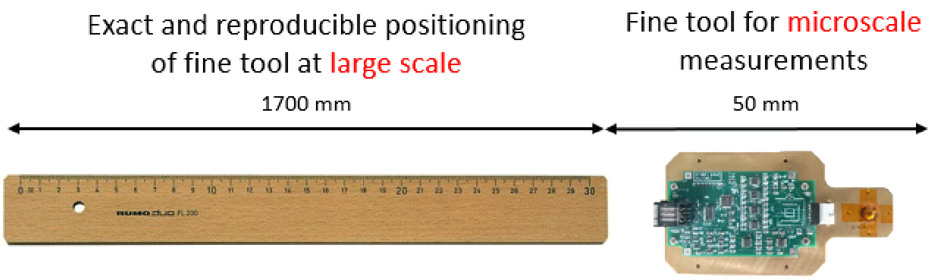

Fig. 3.5: Sketch of the alignment principle combining a large scale exact and reproducible positioner and a fine tool for precision measurement.

Via the in-plane alignment reconstruction misalignments and imperfections within a single readout plane are identified. These are introduced during the gluing process. Possible misalignments are small rotations or shifts of the readout boards (see figure 2.6a) with respect to each other. The absolute position reconstruction of the readout panel is a combination of a large scale alignment tool and a fine precision measurement tool ($\lesssim 10\,\mu$m). The large scale tool is used to position the fine tool exactly and reproducibly (see fig. 3.5). For the in-plane alignment two different large scale approaches are used, which are described and compared in the following sections. A third method based on cosmic muon data from a working Micromegas module using the Cosmic Ray Facility is described in chapter 5.

3.4 Reconstruction using the jig

The jig is a stiff aluminum honeycomb structure with well positioned spheres for an exact and reproducible positioning of the fine tool. During the measurement the jig is put on top of the readout panels (see figure 3.7). For a correct alignment reconstruction, a reproducible positioning of the jig on top of the panels is necessary. This is done by aligning the L- and V-spacers (see fig. 3.6 and red squares in fig. 3.7, right), that are on the long side of board 8 and on the long side of the jig, to the pins that are fixed to the granite table. The readout panels lie on so-called chims, which are precisely manufactured granite blocks with a height of 24.949 mm. After the alignment of the panel and the jig with the pins, the jig gets fixated using an aluminum bar, that gets fixated on the granite table using clamps (red squares in fig. 3.7, left).

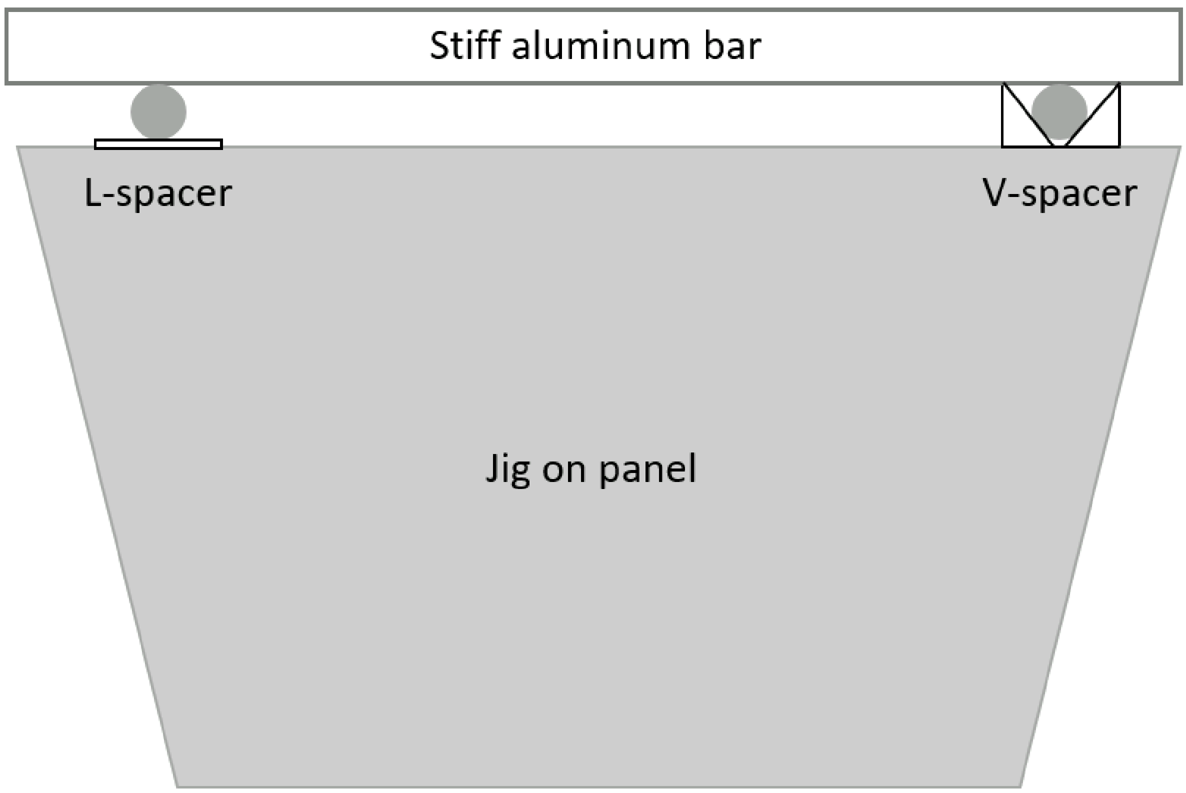

Fig. 3.6: Sketch of the positioning of the jig and the panel on the granite table. They are aligned using the V- and L-spacer, which are on the jig and panel, and two cylinders, that are fixed on the aluminum bar.

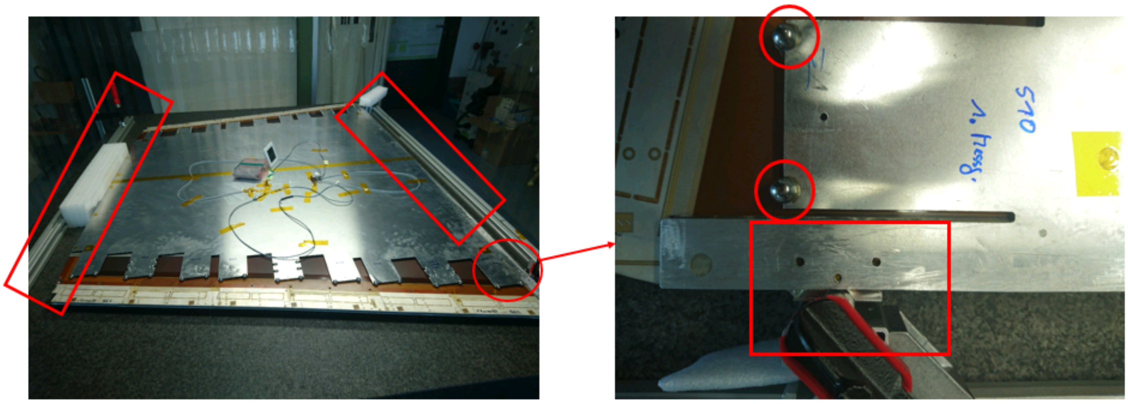

Fig. 3.7: Picture of the jig placed on top of a readout panel. The fine tool (Surveyor) is placed on top of the spheres of the jig (red circles, right). The jig is positioned by aligning the V- and L-spacer of the jig and panel to the alignment pins on the lower aluminum bar (red squares). Clamps and the upper aluminum bar are used as fixation. A lead block is placed on top to counteract possible bending of the jig during to the fixation process.

The readout system of the alignment measurements using the jig, consists of a so-called surveyor, readout by an ethernet connection to a laptop with the Rasnik readout software (see chapter 3.2). The surveyor (see fig. 3.8) contains a C-CCD, that is put on top of the Rasmasks, a camera head with ethernet connection and two cones on the bottom, used to position the surveyor on top of the spheres of the jig.

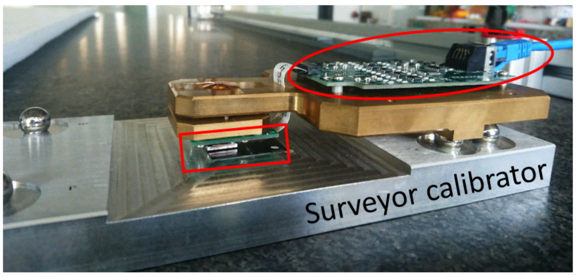

Side view

(a) Side view of the surveyor on top of its calibrator. In the red circle the camera head electronics and the ethernet connection are visible. The red square indicates the position of the C-CCD sensor. The surveyor calibrator allows determination of the position of the C-CCD centre with respect to the cones.

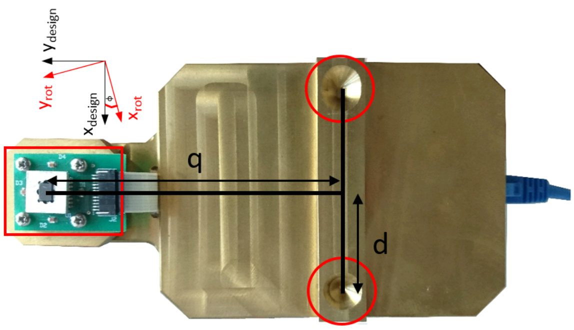

Bottom view

(b) Bottom view of the surveyor. The red square shows the minimal head of the C-CCD, with the photosensitive CCD sensor in the centre between the four screws sitting underneath a fiber optic plate (FOP, black). The cone (bottom) and the long cone (top) inside the red circles are used to reliably position the surveyor on the spheres of the jig. The four LED's are positioned between the screws of the minimal head. The three parameters q, d and ϕ describe the positioning of the FOP to the two cones.

Fig. 3.8: Different views of the surveyor and its calibrator, which is used for image taking of the Rasmasks in combination with the jig for the in-plane alignment of the readout panels.

For one readout layer, measurements at each of the 18 mask position are performed. For a correct position determination the distance between the centre of the C-CCD sensor to the cones has to be determined. This is done using the surveyor calibrator (see fig. 3.8a). It is a stiff aluminum plate containing a glasmask and four sets of spheres to position the surveyor. Combining the results of the measurements at all four positions the rotation of and the distance between the cones of the surveyor and the centre of the FOP can be determined. The results are a rotation of $\phi_{\text{C-CCD}} = -9.265\,\text{mrad}$, an elongation of $d = 34.018\,\text{mm}$ and a shortening of $q = 89.846\,\text{mm}$ in figure 3.8b. The design values are $\phi_{\text{C-CCD}} = 0\,\text{mrad}$, $d = 34.0\,\text{mm}$ and $q = 89.9\,\text{mm}$ (information provided by Brandeis).

3.4.1 Coordinate transformation and determination of the global position

It is necessary to transform the local position measurements of the Rasmask to a global coordinate system to determine their absolute position on the readout panel. A typical dataset for one readout panel is shown in figure B.2 in appendix B. Equations 3.1 and 3.2 are used to transform the measured mask positions to the global coordinate system (x_G, y_G).

$$\begin{aligned} x_G = {} & ((y_{\text{meas}} + x_{\text{surveyor}} - x_{\text{offset}}) \cdot \cos(\phi_{\text{image}} - \phi_{\text{C-CCD}}) - \\ & (x_{\text{meas}} - y_{\text{surveyor}} \cdot (-1)^n - y_{\text{offset}}) \cdot \sin(\phi_{\text{image}} - \phi_{\text{C-CCD}})) \cdot (-1)^n + \\ & x_{\text{calibration}} + x_{\text{nominal}} \end{aligned} \tag{3.1}$$

$$\begin{aligned} y_G = {} & ((y_{\text{meas}} + x_{\text{surveyor}} - x_{\text{offset}}) \cdot \sin(\phi_{\text{image}} - \phi_{\text{C-CCD}}) + \\ & (x_{\text{meas}} - y_{\text{surveyor}} \cdot (-1)^n - y_{\text{offset}}) \cdot \cos(\phi_{\text{image}} - \phi_{\text{C-CCD}})) \cdot (-1)^{n+1} + \\ & y_{\text{calibration}} + y_{\text{nominal}} \end{aligned} \tag{3.2}$$

x_{meas} and y_{meas} in the above equations correspond to the first and second entry of an analysed mask as described in chapter 3.2. Due to the orientation code 2 for jig measurements the y_{meas} value is oriented along the x-coordinate in the global system and vice versa. ϕ_{image} corresponds to the rotation of the masks with respect to the surveyor. These three values are taken directly from the analysis results.

Figure 3.9 illustrates the orientation of the coordinate systems in which the values are received as well as the coordinate system to which they are transformed. The orientation code is always 2 for jig measurements, so the orientation of the measurement coordinate systems differ between the left and right side. Also indicated are the surveyor positions and the corresponding mask names. For example the mask name of the bottom left mask is 1-00.

The x_{surveyor} and y_{surveyor} in the first line of eq. 3.1 and 3.2 correspond to the offsets between the C-CCD centre and its nominal position on the surveyor. These two and the rotation of the C-CCD $\phi_{\text{C-CCD}}$ are determined by the surveyor calibrator. The offsets are 54 µm for x_{surveyor}, 18 µm for y_{surveyor} and $\phi_{\text{C-CCD}} = -9.265\,\text{mrad}$. The sign factor $(-1)^n$ after y_{surveyor} accounts for the surveyor offset depending on the side on which the mask is located on. For masks on the left side (-00, -04, -08) and right side (-02, -06, -10) is $n = 0$ and $n = 1$, respectively.

All masks that are used for the alignment are small parts of one large mask (see fig. B.3 in the appendix). Therefore each mask has a different offset from the origin of this large mask. The x_{offset} and y_{offset} correspond to these individual offsets. They are used to determine the relative displacement in the mask coordinate system. The following formula for a mask with a name of the form b-ss (e.g. 1-00) and a width of 11.880 mm is used to calculate those offsets:

$$x_{\text{offset}} = (ss + 0.5) \cdot 11.880\,\text{mm} \tag{3.3}$$

$$y_{\text{offset}} = (b + 0.5) \cdot 11.880\,\text{mm} \tag{3.4}$$

The second sign factor $(-1)^n$ at the end of the second lines of the two equations 3.1 and 3.2 corresponds to a correct application of the difference between the nominal and measured position on the mask, depending on the board side. As before, for the left side (-00, -04, -08) follows $n = 0$ and the right side (-02, -06, -10) $n = 1$, respectively.

To ensure the correct position in the global coordinate system each mask has an individual nominal position that is added in the third line (x_{nominal} and y_{nominal}). This is essential for the fitting method described in 3.4.2.

At last the $x_{\text{calibration}}$ and $y_{\text{calibration}}$ values are added. These values correspond to calibration parameters that account for deviations of the sphere positions to their nominal position. The calibration and its results are described in detail in section 3.4.3.

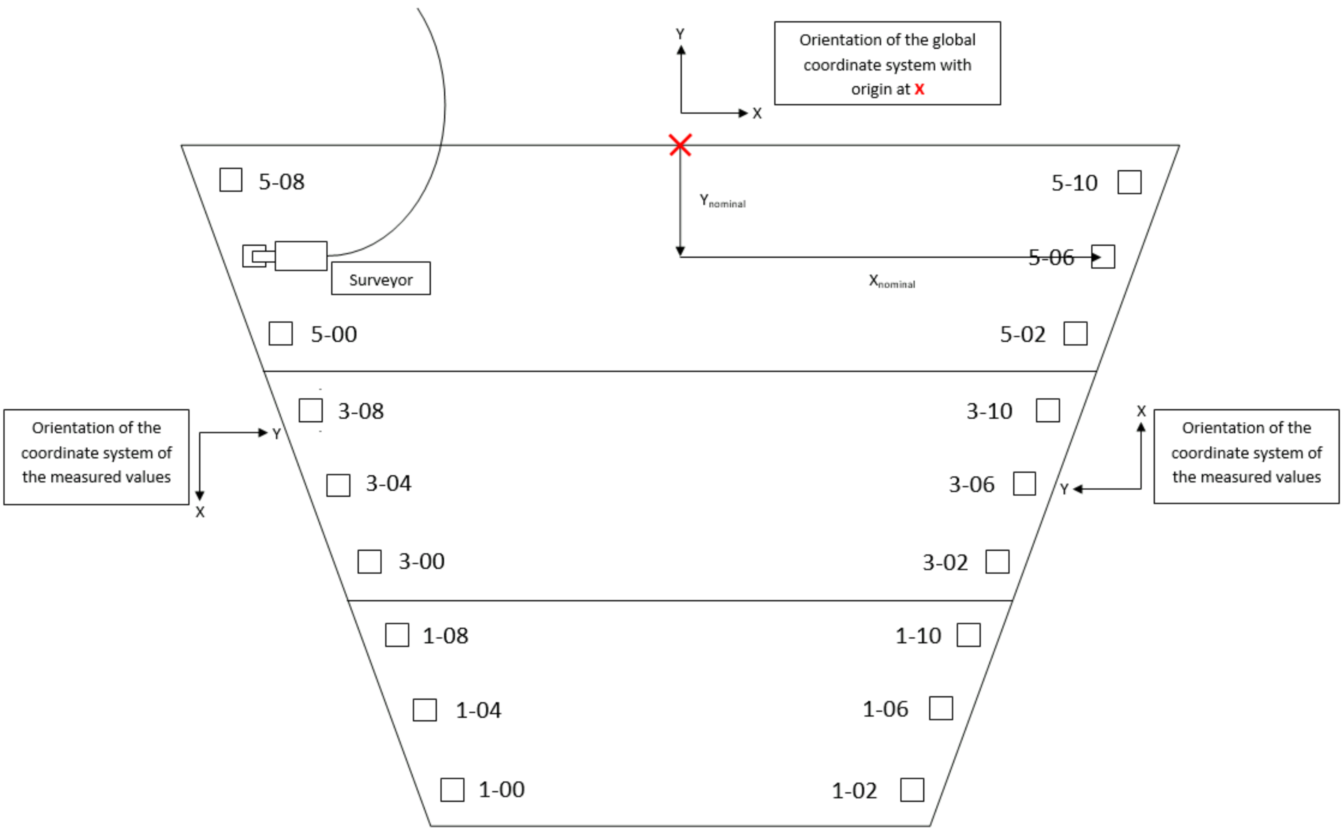

Fig. 3.9: A sketch illustrating the coordinate transformation from the measured values to the global system as well as the difference between the measurements from the left and right side. Also shown are the surveyor for image taking and the mask names.

3.4.2 Fitting method

To account for a global displacement of the jig with respect to the panel, a global minimisation of the residuals is performed. These residuals are the difference between the nominal mask position and the reconstructed global position (see eq.3.1 and 3.2). At first each mask is individually fit to its nominal position (see eq. 3.5 and 3.6). The nominal positions are displayed in figure 3.10. Parameter $p_0 = 0$ is fixed. The parameters 1 and 2 are free. The fixing of one parameter is necessary for the fitting process to converge. To obtain the highest accuracy in precision direction, the non-precision coordinate is fixed. The fractions containing $p_2 = \tan[\theta]$ correspond to a rotation matrix accounting for a global rotation of the panel. The reconstructed residuals in precision direction (ΔY) are summed up to the total residual f. This value is minimised by varying parameters 1 and 2. This corresponds to a global rotation and shift in precision direction of the whole reconstructed readout layer to account for a mispositioning between the jig and the panel.

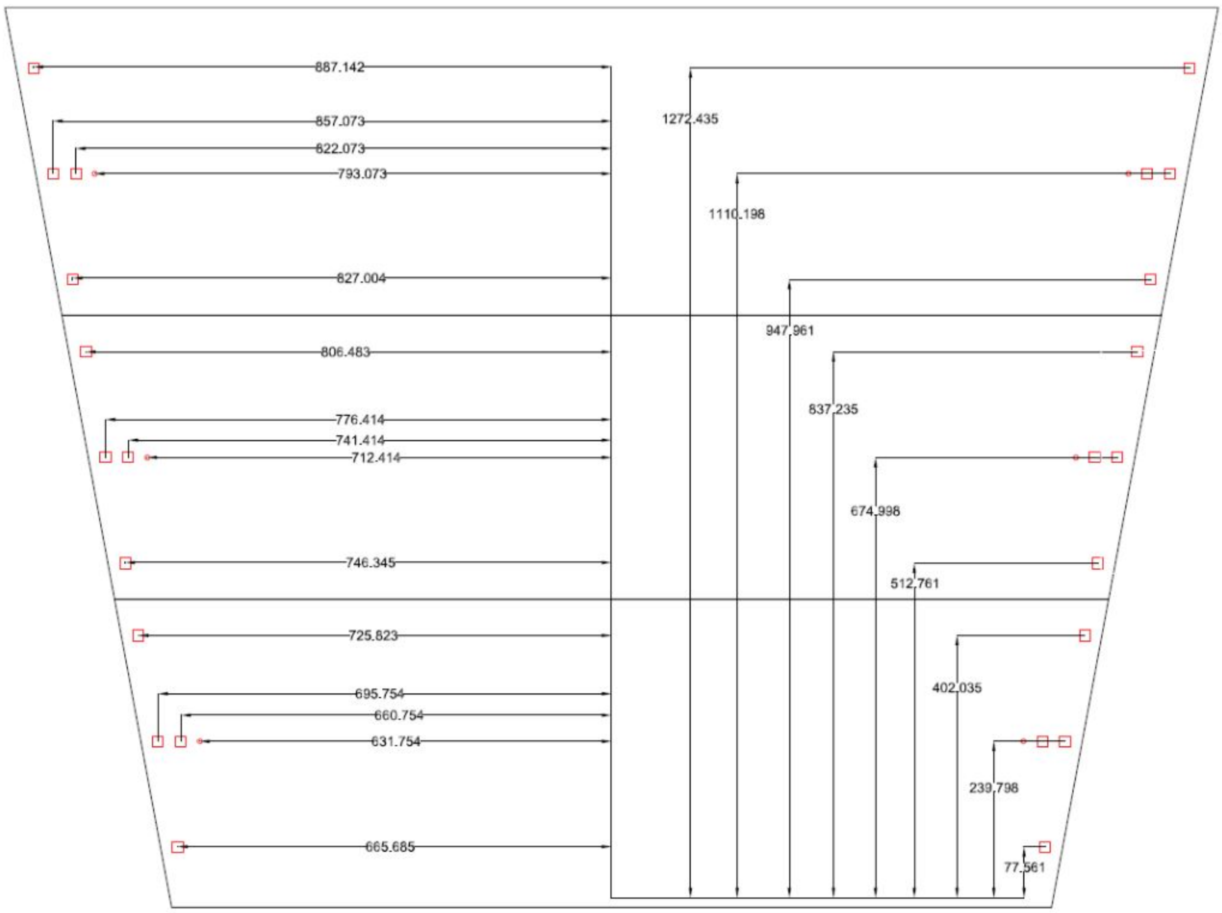

Fig. 3.10: Nominal positions of the Rasmasks on the readout panel (taken from [**Herrmann 2019**]). For this thesis the nominal mask positions are transformed to a coordinate system with the origin at the centre of the top edge (see fig. 3.9).

$$\begin{aligned}\Delta X = {} & \frac{1}{\sqrt{1+p_2 \cdot p_2}} \cdot (X_{\mathrm{G}} - p_0) - \\ & \frac{p_2}{\sqrt{1+p_2 \cdot p_2}} \cdot (Y_{\mathrm{G}} - p_1) - \\ & X_{\mathrm{nominal}}\end{aligned} \tag{3.5}$$

$$\begin{aligned}\Delta Y = {} & \frac{p_2}{\sqrt{1+p_2 \cdot p_2}} \cdot (X_{\mathrm{G}} - p_0) + \\ & \frac{1}{\sqrt{1+p_2 \cdot p_2}} \cdot (Y_{\mathrm{G}} - p_1) - \\ & Y_{\mathrm{nominal}}\end{aligned} \tag{3.6}$$

$$f = \sum_{n=1}^{18} (\Delta Y_{\mathrm{n}} \cdot \Delta Y_{\mathrm{n}}) \tag{3.7}$$

- p_0 can be used to account for global shifts in x-direction. For a converging minimisation in y-direction this parameter has to be set to 0.
- p_1 is used to account for global shifts in y-direction.
- $p_2 = \tan(\theta)$ is accounting for global rotations, where θ is the rotation angle.

3.4.3 Calibration

The calibration of the jig with spheres, that have an expected position accuracy of ±0.2 mm is performed with reference measurements, that were performed in December 2018 in Saclay (France). The reconstructed residuals of those measurements for the Eta 10 readout panel in precision direction for both gluing sides are shown in figure 3.11. The whole dataset of the residuals (precision and non-precision direction) can be found in table B.1 in the appendix. These reference measurements were taken using a precise optical Coordinate Measuring Machine, which is calibrated on a level of about 10 µm.

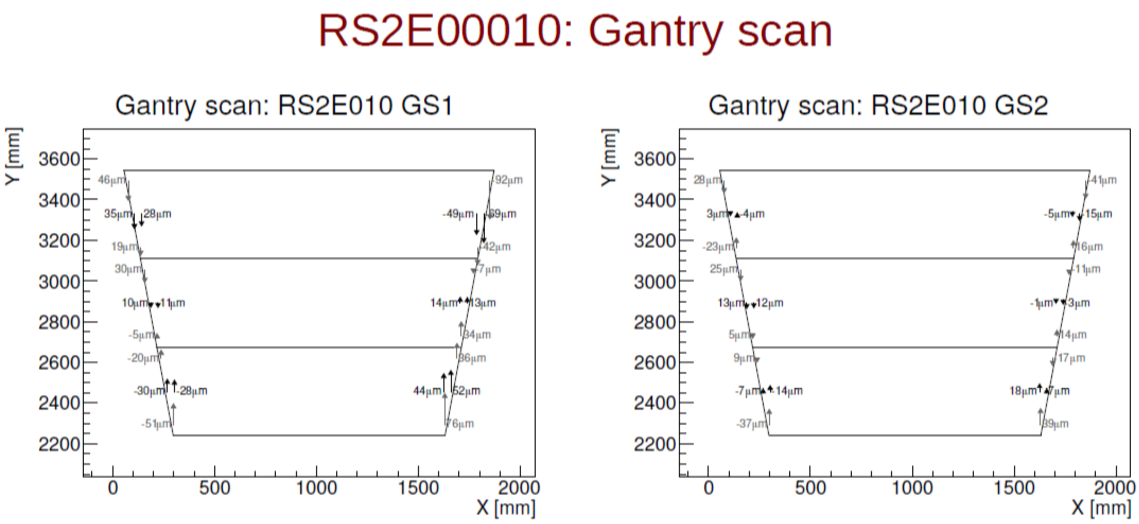

Fig. 3.11: Residuals calculated from the measurements preformed in Saclay (Dec.2018) for the panel Eta 10. Residuals are taken as reference for the calibrations of the jig and the CMM at Garching. Measurements done by Maximilian Herrmann, Paola Arrubarrena (both LMU Munich) and Pierre-François Giraud (CEA Saclay); analysis by Pierre-François Giraud.

The goal of the calibration is to achieve the same residuals using the jig. Therefore residuals from both methods, reference and jig reconstructed, are compared. To ensure the calibration produces reliable values for each measurement, this comparison is done for four readout layers simultaneously, to identify possible mismeasurements. The simultaneous analysis of four layers leads to an minimisation between both measurements, rather than to an exact reconstruction of the reference residuals with the jig.
Calibration parameters for the reconstruction of the global position (see $x_{\text{calibration}}$ and $y_{\text{calibration}}$ in subsection 3.4.1) are obtained in precision and non-precision direction for the 18 masks. The differences between the reference and reconstructed residuals before the calibration are shown in 3.12a and 3.12b. These differences are randomly distributed with a total width of $\Delta x = 2.45$ mm and $\Delta y = 0.53$ mm and a standard deviation of $\sigma_x = 516$ µm and $\sigma_y = 158$ µm respectively. A successful calibration minimises the standard deviations below the measurement error boundaries (discussed later in this subsection) and narrows the total width. Diagrams 3.13a and 3.13b show these differences after the calibration. An improvement for both directions regarding the total width and standard deviation is visible. Yet the quality of the calibration in non-precision direction is a lot worse than in precision direction.

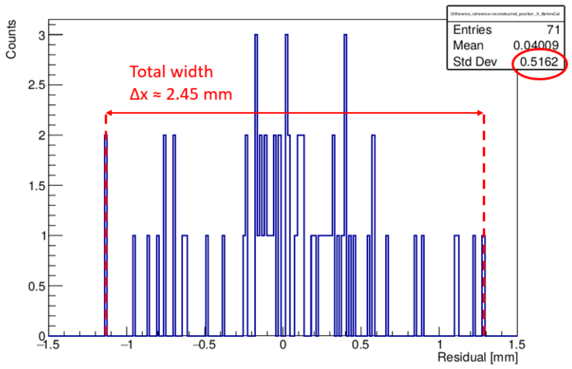

(a) Differences between residuals of the measurements from Garching and Saclay in **non-precision** direction (x-direction) before calibration. The distribution is random with a large standard deviation and total width.

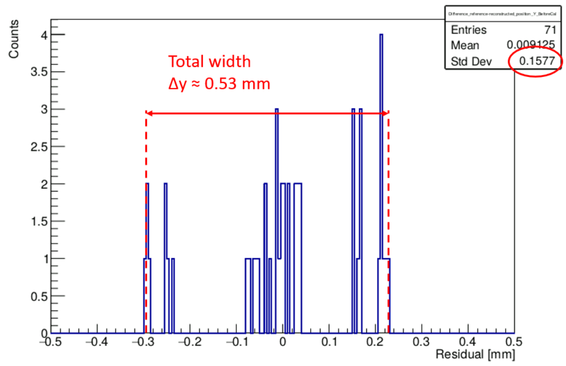

(b) Differences between residuals of the measurements from Garching and Saclay in **precision** direction (y-direction) before calibration. They are distributed randomly with a standard deviation larger than the measurement error of 12.2 µm, which is discussed later in this subsection.

Fig. 3.12: Difference between measured residuals from July 2019 and reference measurements from Saclay (Dec. 2018) for all four readout layers (Eta 10 GS1/GS2 and Stereo 11 GS1/GS2) for non-precision direction (left) and precision direction (right) before applying calibration corrections.

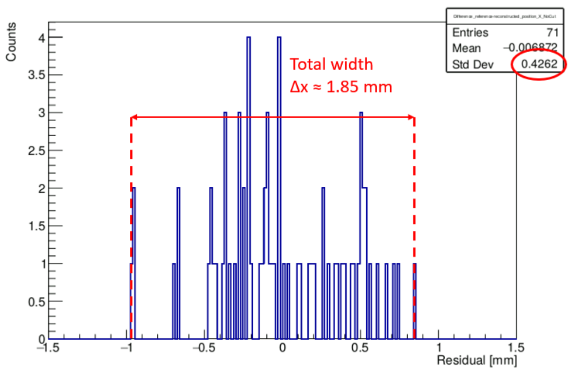

(a) Difference between residuals of the measurements from Garching and Saclay in **non-precision** direction (x-direction) after the calibration. The total width is widened by single layer large residuals (−1 mm). This results in a large standard deviation of 426 µm.

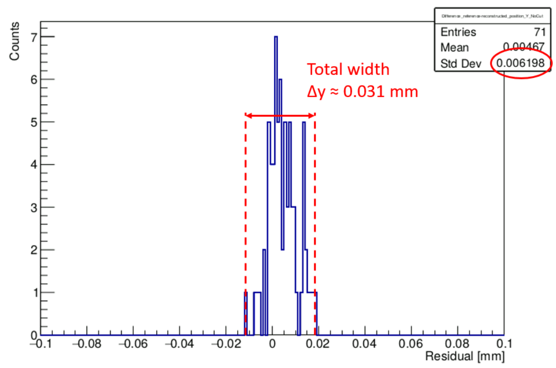

(b) Difference between residuals of the measurements from Garching and Saclay in **precision** direction (y-direction) after the calibration. The standard deviation is now within the measurement standard dev. of 12.2 µm.

Fig. 3.13: Difference between calibration measurements from July 2019 and reference measurements from Saclay (Dec. 2018) for all four readout layers (Eta 10 GS1/GS2 and Stereo 11 GS1/GS2) for non-precision direction (left) and precision direction (right) after the calibration corrections.

The first major influence is the fitting method described in subsection 3.4.2, where the x-coordinate is fixed during the fitting process. Only the y-coordinate and the angle are varied to correct for global displacements and distortions. Besides the effects caused by the fitting process another important influence is the large variation of single layer mask residuals in non-precision direction in the reference datasets (see figure B.4 and B.5 in the appendix B.2). These single measurements, are not compatible with the measurements of the other three layers distorting the results by a large margin. One residual at −1 mm in figure 3.13a is accounted for by three residuals of about +0.33 mm. To improve the quality in non-precision direction, these measurements are excluded, assuming they are mismeasurements.

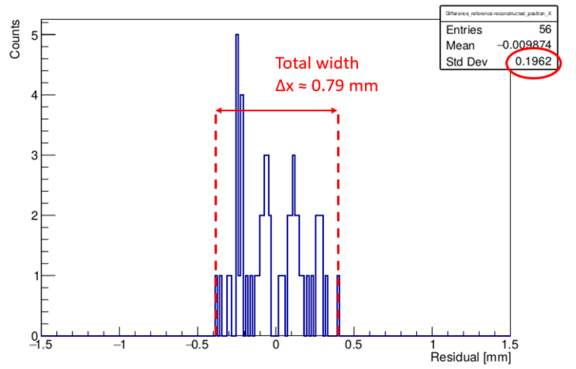

(a) Difference between residuals of the measurements from Garching and Saclay in **non-precision** direction after applying a cut on the mismeasurements showing its improving effect. The total width and standard deviation are narrowed a factor of > 2. The four visible peaks cannot be assigned to individual panels or gluing sides.

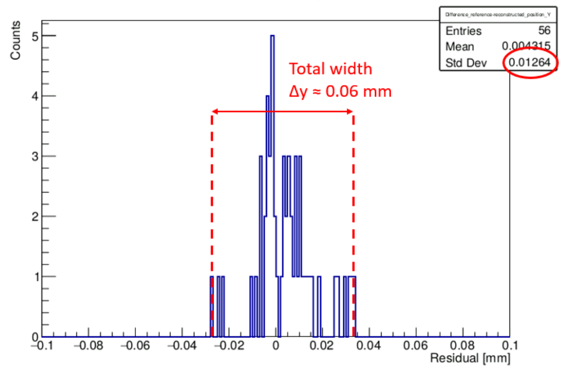

(b) Difference between residuals of the measurements from Garching and Saclay in **precision** direction after applying a cut on the mismeasurements to improve the calibration quality in non-precision direction. The standard deviation exceeds the measurement error of 12.2 µm by 0.4 µm. The reason for this is the unknown temperature difference between the jig and the panel, which may be larger than the assumed 1 K.

Fig. 3.14: Difference between calibration measurements from July 2019 and reference measurements from Saclay (Dec. 2018) for all four readout layers (Eta 10 GS1/GS2 and Stereo 11 GS1/GS2) for non-precision direction (left) and precision direction (right) after applying a cut and calibration corrections. In total 15 masks are cut.

These cuts result in an improvement shown in figure 3.14. The large standard deviation before the cuts of 426 µm is reduced by more than a factor of 2 to 196 µm. The standard deviation of the calibration in precision direction is still within the expected measurement precision (see equation 3.8). The calibration constants $x_{\text{calibration}}$ and $y_{\text{calibration}}$, that are obtained with cuts, are used for all analyses and alignment reconstructions, that are performed using the jig.

The precision of the position reconstruction using the C-CCD and the jig is determined by the resolution of the C-CCD and possible deformations of the jig, which result in an error due to non-reproducible positioning of the Surveyor. Also a non-exact reconstructible expansion of the panels due to humidity give rise to possible differences between the reference and jig measurements. The measurement error of the C-CCD (≈ 7 µm) is discussed in [**Vogel 2017**]. Errors due to deformations of the jig, with a main focus on thermal expansion, are discussed in the subsection 3.4.5. Since no temperature monitoring was done for these measurements, the error can only be estimated. A good estimation is in the order of 10 $\frac{\mu\text{m}}{\Delta\text{K}}$ in precision direction, where ΔK is the difference between the temperature of the jig and the panel. This temperature difference is typically below 1 K yet some measurements exceed these differences. The total measurement error is estimated as:

$$\begin{aligned}\Delta Y_{\text{meas}} &= \sqrt{\text{C-CCD}^2_{\text{meas-error}} + \text{jig}_{\text{deformation}}{}^2} \\ &= \sqrt{(7\,\mu\text{m})^2 + (10\,\mu\text{m})^2} \\ &= 12.2\,\mu\text{m}\end{aligned} \tag{3.8}$$

Combining the error of the single measurement with the standard deviation of the calibration, the total error for the jig alignment reconstruction becomes:

$$\begin{aligned}\Delta Y_{\text{total}} &= \sqrt{\Delta Y^2_{\text{meas}} + \Delta Y^2_{\text{calibration}}} \\ &= \sqrt{(12.2\,\mu\text{m})^2 + (12.6\,\mu\text{m})^2} \\ &= 17.5\,\mu\text{m}\end{aligned} \tag{3.9}$$

3.4.4 Analysis example of one readout layer

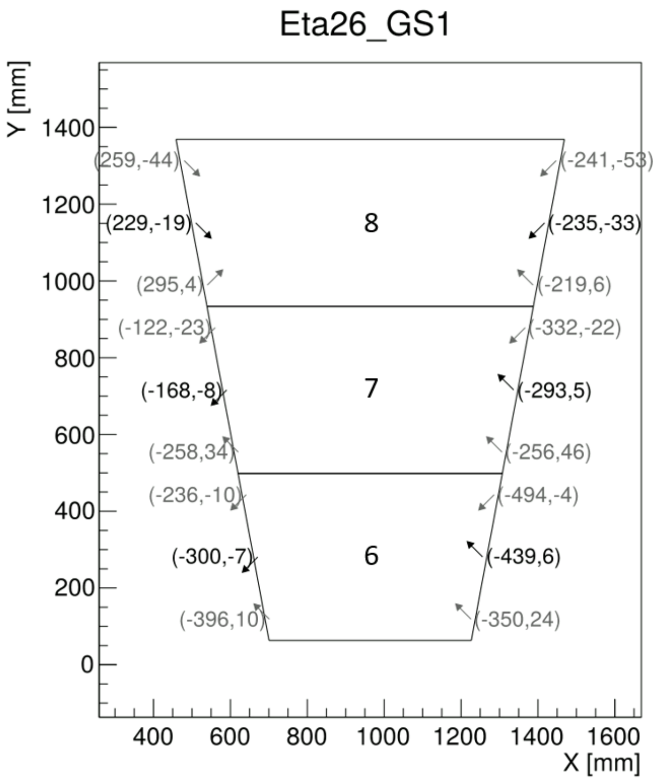

Fig. 3.15: Residual plot for Eta 26 gluing side 1. Shown are the residuals in x-and y-direction (Δx, Δy). A shrinkage of all readout boards in y-direction is visible. For the boards 7 and 8 this contraction is in the order of $48 - 68\,\mu$m, for board 6 it is $20 - 28\,\mu$m. A small left-right difference of $\approx 13\,\mu$m of all boards corresponds to a rotation around the centre of the PCBs of 4.67 µrad, 4.19 µrad and 4.08 µrad (boards 6, 7 and 8).

Figure 3.15 shows the results of the alignment reconstruction of the gluing side 1 of Eta panel 26. The numbers in the brackets are the residuals between the reconstructed and nominal position for x-and y-direction (Δx, Δy). The residuals in precision direction are much smaller than in non-precision direction. The first reason is the fit method, which minimises in precision direction for an optimal reconstruction in the more sensitive readout direction. Comparing the reconstructed residuals to the resolutions for the two directions (≤ 4 mm for x and ≤ 100 µm for y), the induced misalignments are smaller than the desired resolution. The alignment during the gluing is done at the centre of each board (values in bold).

Analysing the y-residuals of one readout board (6, 7, 8) shows a shrinkage of all boards in y-direction. This change in length is visible by a difference of the distance between the top and bottom mask compared to its nominal distance. For board 7 and 8 this shrinkage is in the order of $48 - 68$µm, whereas board 6 shows a contraction in the range of $20 - 28$µm. This shrinkage is a result of the humidity dependent expansion/shrinkage of the readout boards, which happened before the gluing of the three boards. Comparing the left and right side of one board shows differences of ≈ 13 µm. This corresponds to rotations of the boards around the centres of the PCBs of 4.67 µrad, 4.19 µrad and 4.08 µrad (boards 6, 7 and 8).

3.4.5 Temperature Studies

The effect of expansion and shrinkage due to temperature change on the measurement accuracy is investigated in the following. Since the jig is built in a sandwich structure of two aluminum plates with an aluminum honeycomb in between, it is susceptible to temperature changes. The readout panels themselves expand and shrink as well. Therefore the actual experimental effect on the position measurement should be smaller than the linear thermal expansion coefficient of aluminum of $\alpha = 23.1 \cdot 10^{-6} \, \frac{1}{K}$ [**Lide 2003, sec.12 p.219**]. The experimental setup of the temperature measurements is shown in figure 3.16. The red circles indicate the position of the four temperature sensors, that are used for tracking the temperature.

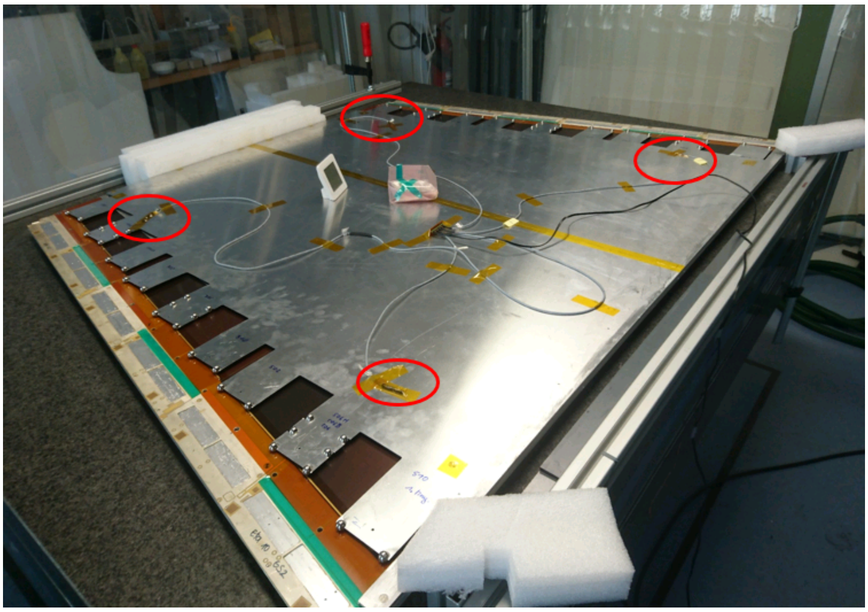

Fig. 3.16: Experimental setup of the temperature measurement. In total four temperature sensors (inside the red circles) are used to track the temperature of the jig. The rest of the setup is identical to the typical measurement setup described in section 3.4.

A typical temperature trend is visible in figure 3.17 as a fluctuation around its mean temperature of one set of position measurement (all 18 masks of one panel). The total fluctuation width is 0.38 K. The step structure results from the readout of the sensors, which have a discretisation of 0.06 K.

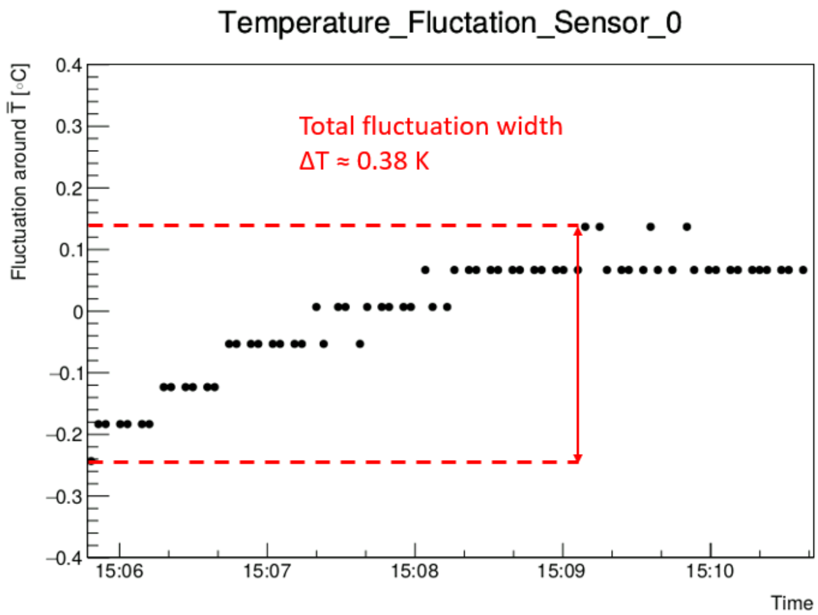

Fig. 3.17: Temperature fluctuations of one sensor around its mean value during one set of position measurement. The discrete steps are because of the sensor readout precision.

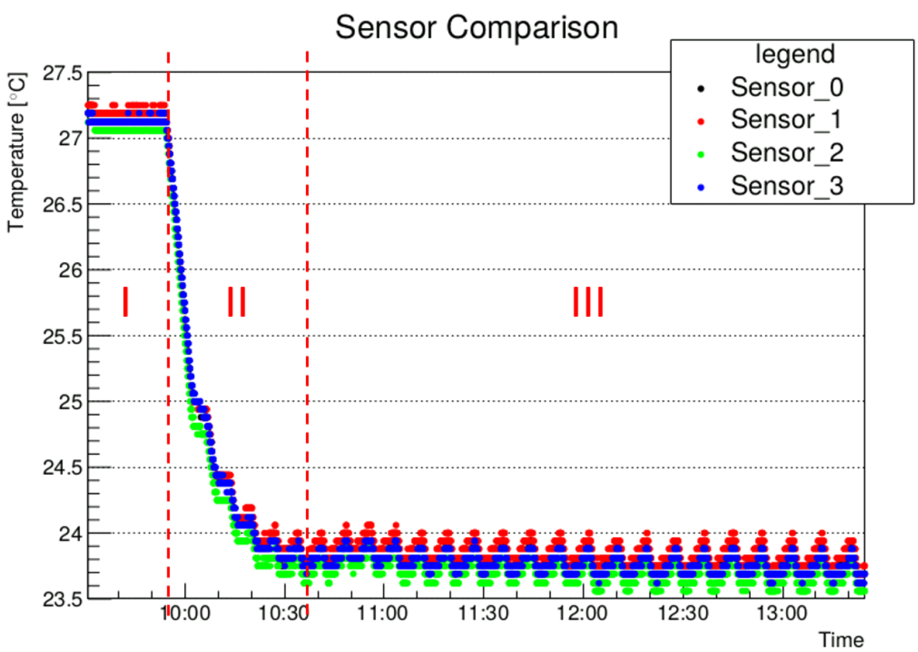

Fig. 3.18: Measured temperatures of all four sensors with air condition off (I), turned on to cool the room (II) and after reaching the set temperature of the air condition system (III). All sensors show the same behaviour over the whole time. Especially in region II they measure the identical temperature. The bumps in section II and III correspond to the starting and stopping of the air condition.

One measurement checking the comparability of the four temperature sensors is done. Constant offsets between different sensors need to be accounted for, if they exist. For this measurement all sensors are placed close to each other on the jig and the temperature in the room is linearly decreased. The measured temperatures for each sensor are shown in figure 3.18. Section I shows the measured temperature before turning on the air condition system. Small differences in the order of the readout precision are visible. In section II the sensors measure identical temperatures except when the air condition stops and starts. This process is seen as bumps in the trend. The last section III is the time after the air condition system reached a stable temperature. To stay at this temperature the air condition periodically starts and stops. The first slightly higher values after the separation line between II and III are caused by persons entering the room. Overall the sensors are comparable and therefore suitable for the temperature studies on the jig.
Position measurements at three different temperatures are taken, to investigate the behaviour of the jig under temperature changes. During the acclimatisation of the room the jig remains inside. The panel is not acclimated to maximise the effect of the thermal expansion of the jig. Assuming the same temperature for the panel for all measurements, the expansion of the jig is calculated from the linear thermal expansion of aluminum $\alpha = 23.1 \cdot 10^{-6}\,\frac{1}{K}$ and the distance between the top and bottom mask as:

$$\Delta d = \alpha \cdot d_{\text{top-bottom}} = 23.1 \cdot 10^{-6}\,\frac{1}{K} \cdot 1194.874\,\text{mm} = 27.60\,\frac{\mu\text{m}}{\text{K}} \tag{3.10}$$

The results for the three different temperatures for gluing side 1 and 2 are shown in figure 3.19. The total expansion between the cold and hot measurement is 87 µm and 73 µm respectively. The corresponding temperature differences are 8.97 K and 8.65 K. From equation 3.10 the expansion coefficient for the jig for the measurement of gluing side 1 is calculated as $\alpha_{\text{jig}} = 8.12 \cdot 10^{-6}\,\frac{1}{K}$. The expansion coefficient for gluing side 2 is $\alpha_{\text{jig}} = 7.06 \cdot 10^{-6}\,\frac{1}{K}$.

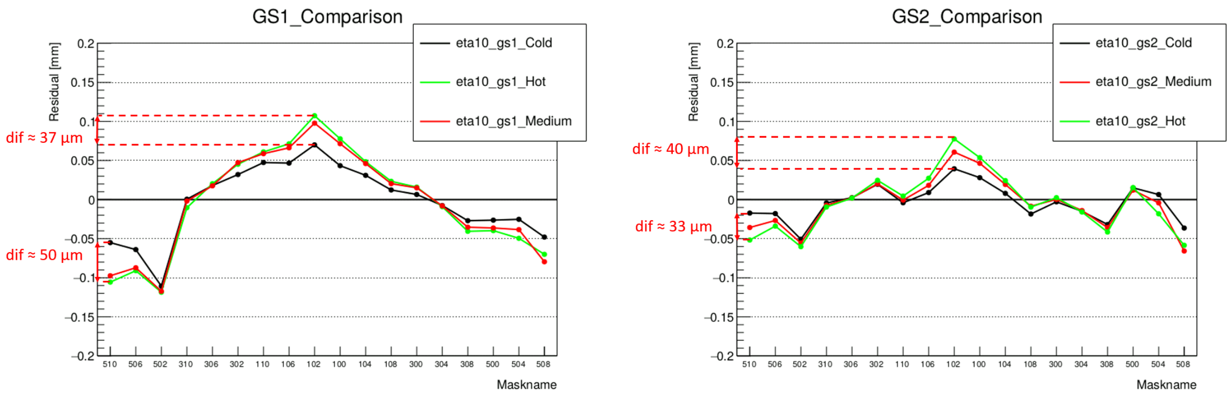

(a) Total expansion of 87 µm between the top most (510) and bottom most (102) Rasmask between the cold (18.32 °C) and hot (27.29 °C) measurement for gluing side 1. This results in a linear thermal expansion coefficient of $\alpha_{\text{jig}} = 8.12 \cdot 10^{-6}\,\frac{1}{K}$.

(b) Total expansion of 73 µm between the top most (510) and bottom most (102) Rasmask between the cold (18.40 °C) and hot (27.05 °C) measurement for gluing side 2. This results in a linear thermal expansion coefficient of $\alpha_{\text{jig}} = 7.06 \cdot 10^{-6}\,\frac{1}{K}$.

Fig. 3.19: Comparison of the residuals at each mask position for three different temperatures. Thermal expansion is visible, yet smaller than the theoretically calculated expansion.

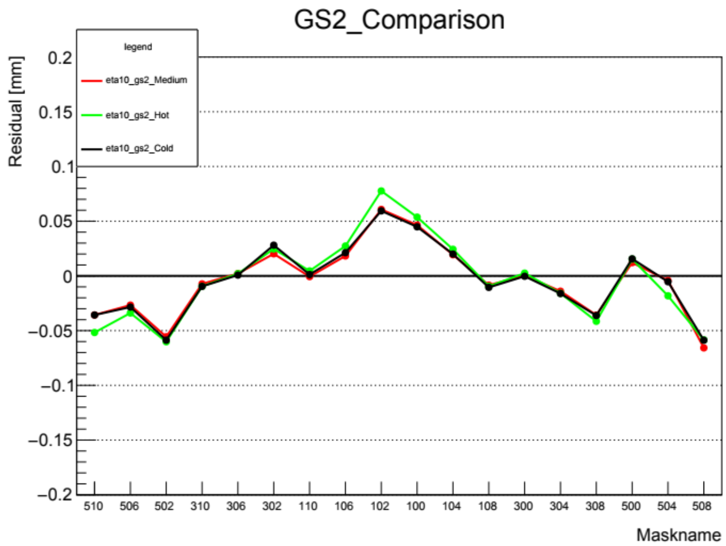

Fig. 3.20: The red and black line correspond to measurements with equal temperatures for jig and panel. The red one was performed at a temperature of 22.46 °C, the cold temperature measurement (black) was done at 18.29 °C. After an acclimatisation period (1 h) no differences in the residual for measurements at different temperatures are visible.

The reason for a smaller expansion of the jig is the expansion of the panel during the measurement. The acclimatisation of the panel lowers the temperature difference between the jig and the panel, which results in a larger expansion coefficient than measured. This measurement method mimics the measurement procedure, if the panels are not tempered in jig measurement during the series production. For calculation of the expansion depending on the temperature difference between jig and panel, the temperature of the panel is tracked alongside the temperature of the jig. After an acclimatisation period of about 1 h after the cold temperature measurement of figure 3.19b, the panel temperature and jig temperature matched. The results of an additional measurement of all masks for tempered panels are shown in figure 3.20. This measurements were done for the cold and medium temperature. The cold measurement now matches the residuals at medium temperature. Therefore an acclimatisation of the panels to the room temperature improves the reproducibility of the position measurements. From this result it is possible to estimate the temperature of the panel at the beginning of the cold measurement as $\approx 22.46\,°\mathrm{C}$, which was the temperature of the jig during the medium temperature measurement. This leads to a temperature difference of 4 K at max between the non thermal equilibrium (see fig. 3.19b) and thermal equilibrium (see fig. 3.20) residuals for the cold temperature. Combining this temperature difference with the total residual difference between the two cold measurements of 40 µm, the real expansion of the jig depending on the temperature difference between jig and panel is:

$$\Delta\, d_{\mathrm{real}} = \frac{\Delta\, d_{\mathrm{meas}}}{\Delta T} = \frac{40\,\mu\mathrm{m}}{4\,K} = 10\,\frac{\mu\mathrm{m}}{\mathrm{K}} \tag{3.11}$$

3.4.6 Alignment results for the reconstruction using the jig

One exemplaric plot showing the residuals in precision direction of all jig measurements (49 panels or 98 gluing sides) for one mask is shown figure 3.21. The distribution has a standard deviation of 21 µm and is centred around −29.7 µm. The total width of the distribution is $\Delta y = 93$ µm. The mean deviation implies an alignment issue during the gluing process, where board 8 is shifted towards board 7 compared to its nominal position in precision direction. This is also visible for all other masks on board 8 (masks 500-510 in table B.2 in the appendix B). In comparison the masks on board 6 show residuals with a positive mean value (masks 100-110 in table B.2). Combining these residuals result in an overall mean shrinkage of all readout panels compared to their nominal size in precision direction of ≈ 163 µm (mask 100 and mask 508 of table B.2).

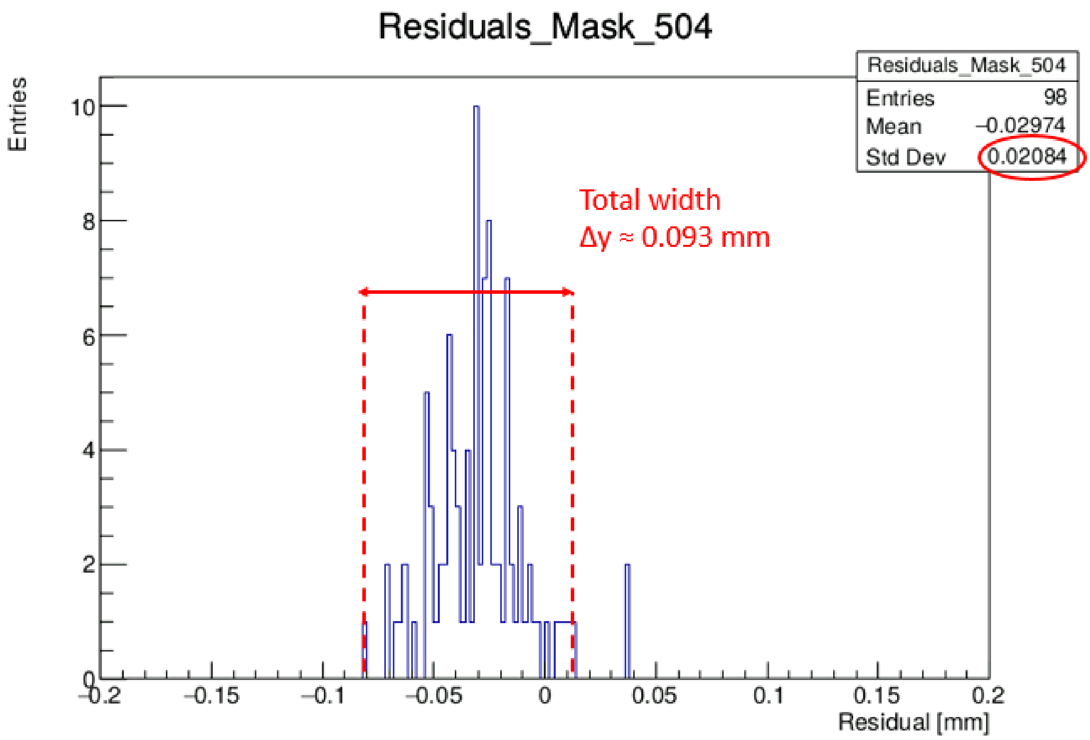

Fig. 3.21: Histogram of the residuals for mask 504 in **precision** direction of all measured gluing sides (98) using the jig. The total width of the distribution is $\Delta y = 93$ µm with a standard deviation of 21 µm. The mean residual for mask 504 is −29.7 µm.

3.5 Alignment reconstruction with a Coordinate Measuring Machine

An alternative approach to reconstruct the in-plane alignment using an optical method is performed with a **C**oordinate **M**easuring **M**achine (CMM). The underlying principle is similar to the reconstruction method using the jig. In this case the CMM takes the place of the large scale, reproducible positioning of the fine tool (telecentric lens system). Pictures of the Rasmasks on each board are taken with a camera. Then these are analysed by a software. The obtained measured positions are fit by a global fit to their nominal positions, the same way as described in 3.4.2. The main difference between this method and the jig is the telecentric camera instead of a C-CCD. For a complete measurement of all masks of the readout panels the camera holder was upgraded. A calibration of the CMM is done using the reference measurements from Saclay. At last the reconstructed residuals of the CMM and the jig are compared.

3.5.1 Layout and design upgrades

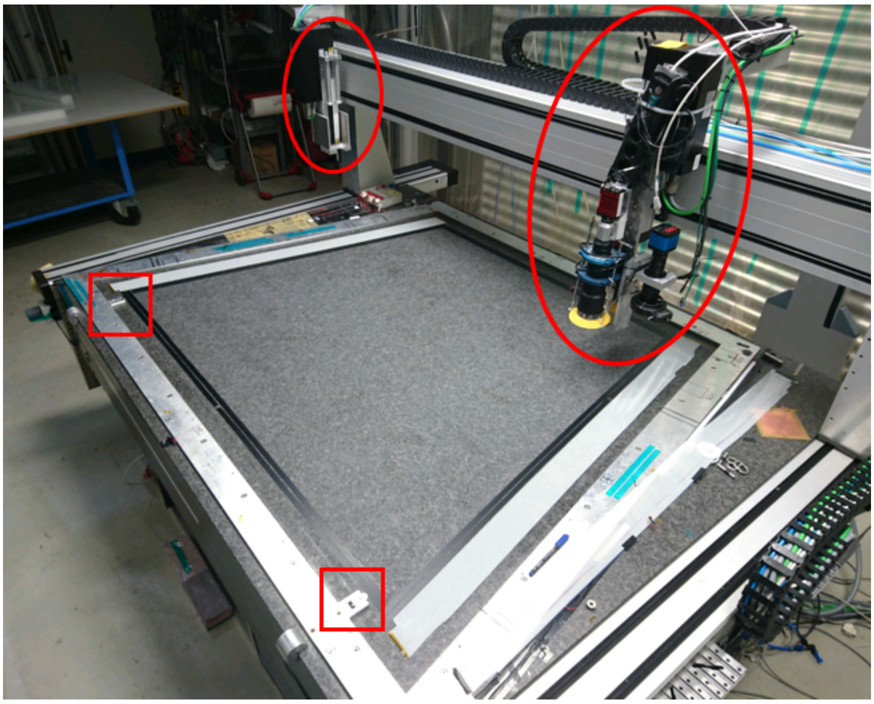

Fig. 3.22: Picture of the Coordinate Measuring Machine (CMM) that is used for gluing, planarity investigations and alignment reconstruction of the readout panels. The camera mounted on the small arm in the right ellipse is used for the alignment measurements. The readout panel is aligned by its V- and L-spacer to the two cylinders (red squares). The camera arm moves over the panel and takes pictures at the mask positions. The second arm in the smaller ellipse is used for gluing.

The CMM is built on top of a granite table having an overall planarity of 6 μm [**Müller 2017, p.22**]. This table has holes in it, so that the panels on top of it, can be fixed by evacuating the space between the table and the panel using a vacuum pump. As shown in figure 3.22 the CMM has one large arm for moving in y direction and two smaller arms mounted on the large arm for moving in x direction, used for gluing and quality control. The quality control consists of a laser sensor for planarity measurements and the telecentric lens system for alignment reconstruction. The lens is fixed by screws to an aluminum plate connected to the small arm. To obtain high quality images an LED ring is used for a homogeneous lighting of the masks. The distance between the ring and the readout panels is freely adjustable by hand. The movement of the CMM is operated by a software running on a PC. The position of the arm can be set in three dimensions, with an origin and orientation as indicated in figure 3.23. The z-position is held constant for all measurements.

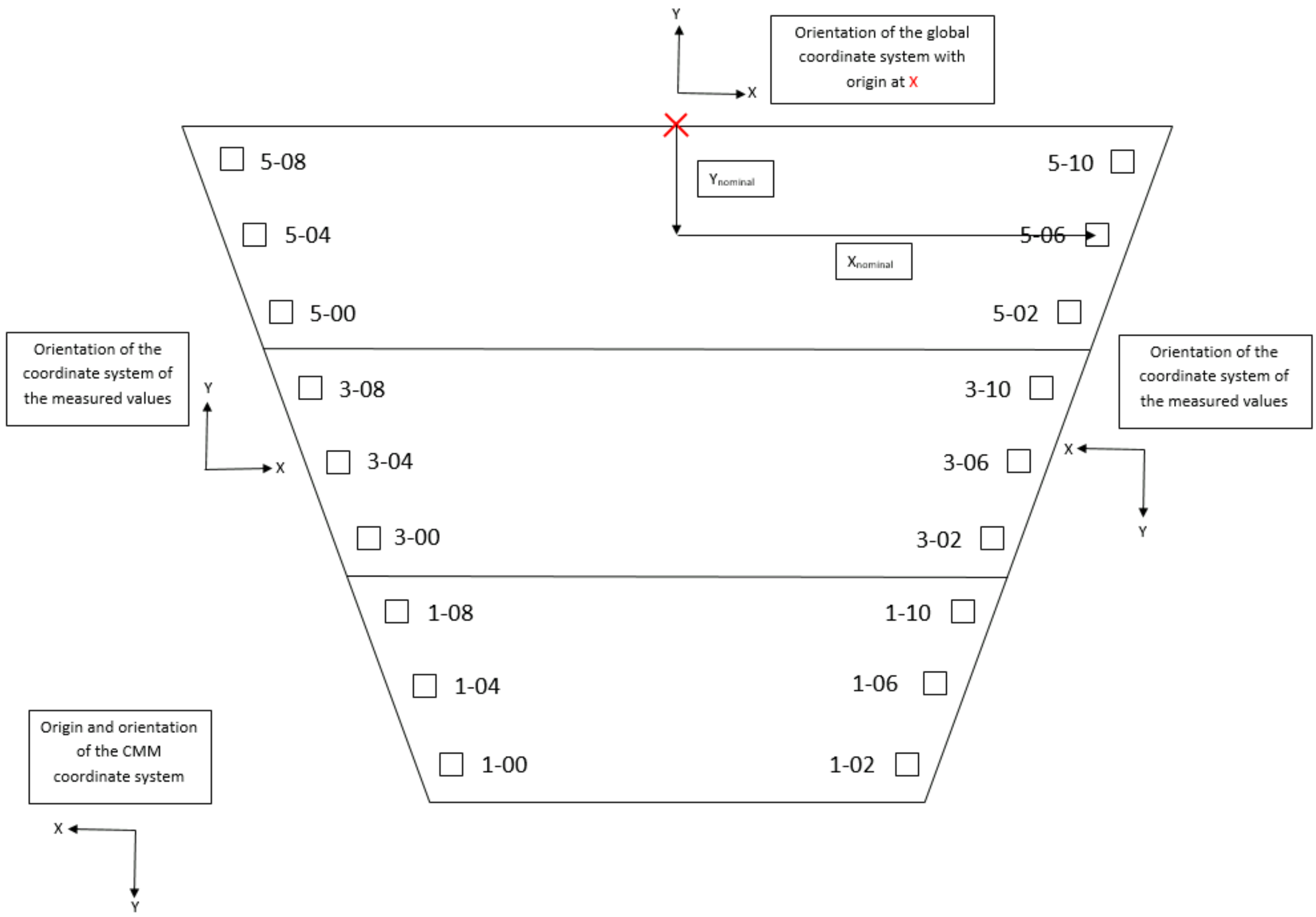

Fig. 3.23: Sketch of the different coordinate systems which have to be accounted for during the residual reconstruction (see section 3.5.3) using the CMM. In the bottom left corner the origin of the CMM coordinate system is indicated. Also shown are the positions of the Rasmasks and their names.

Using the CMM with two vertical arms for gluing and quality control of the readout panels resulted at the beginning in an issue that is illustrated in figure 3.24a. Three of the mask positions of one panel could not be measured, because the two arms of the CMM would collide. To overcome this challenge the prior installed camera holder was replaced by a new one, placed such that the arms do not collide and that all mask positions can be analysed. Figure 3.24b shows a picture of this new holder. The position of the prior camera holder was rotated by 90° anti-clockwise around the arm with respect to the new setup. With the new camera holder integrated, measurements of all mask positions are possible (see fig. 3.30 in subsec. 3.5.5).

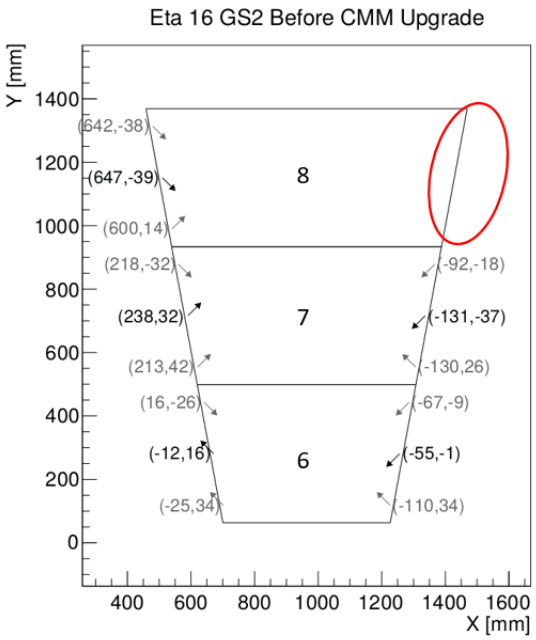

(a) Reconstructed residuals for Eta 16 gluing side 2 before the upgrade of the camera holder. Masks 502, 506 and 510 on board 8 are not accessible due to collision issues with the second vertical arm of the CMM.

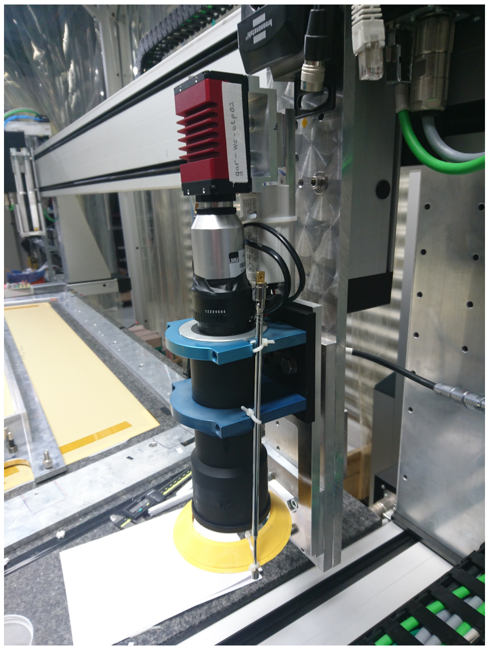

(b) New camera holder with the telecentric lens system mounted on the CMM arm. The prior setup was rotated by 90° anti-clockwise around the vertical CMM arm. The yellow circular shaped object is the LED ring, that is used for enlighting the Rasmasks during the image taking process.

Fig. 3.24: Residual plot of one panel before installing the newly designed camera holder demonstrating the problematics of the old setup (left). Picture of the new camera holder mounted on the CMM (right).

3.5.2 Image evaluation

One image taken with the CMM is shown in figure 3.25a. These images are including besides the Rasmask also its surroundings. The parts close to the actual mask are vulnerable for being wrongly reconstructed, since they also have a chessboard-like pattern due to the reinforcement fibres in the semi-transparent FR4 PCB material. For an improvement of the picture quality one has to exclude the surrounding of the image in the analysis. All pictures are cropped and adjusted in their brightness and contrast to ensure best analysis quality.
Therefore a mask template with the size of the Rasmasks of the PCBs is moved over the image via software. When the template reaches the Rasmask and exactly overlaps it, the original image is cut around the template. The result of this cropping process is shown in figure 3.25b. The filtering decreased the number of wrongly analysed pictures to almost zero. For the few problematic masks left mask damages introduced during production create the problems. For evaluation the images are uploaded to a server similar to the LWDAQ Rasnik analysis, that is used for the jig. As a result of manipulating the image by changing the size, the change of the position in the coordinate system of the CMM has to be accounted for the transformation to the global coordinate system. Since the offset between the centre point of the non-cropped image and the centre point of the cropped image differs for each position of the CMM, this procedure is essential.

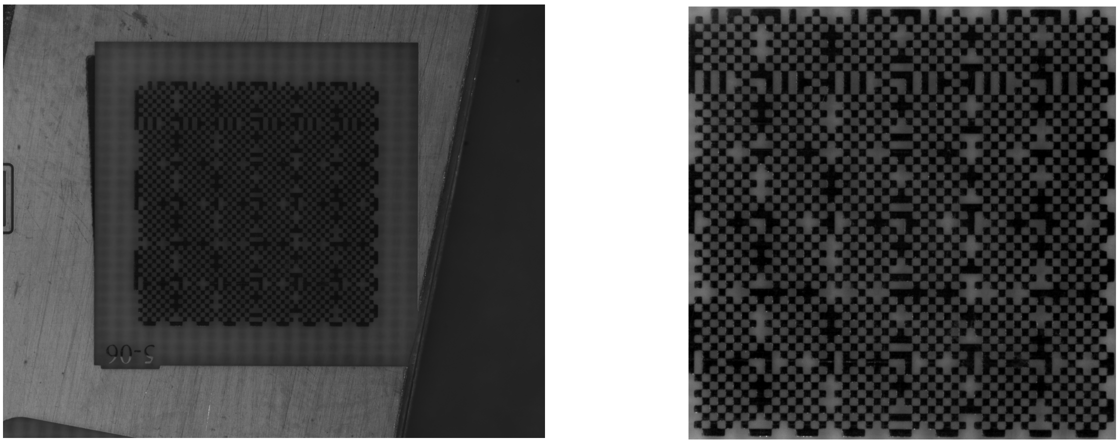

(a) Picture of the mask 506 of Eta 30 GS1 taken by the telecentric camera. The surroundings of the chessboard-like structure might be identified as part of the mask with coded position information leading to analysis problems. Additionally the pictures are inconsistent in their brightness and contrast also causing the analysis to fail.

(b) Picture of the same mask as in (a), after a cropping and adjustment of the brightness. Using these cropped images, increases the number of correctly reconstructed masks to almost 100%. The few still wrongly analysed images arise due to damages introduced during a faulty lithographic process of the panels.

Fig. 3.25: Pictures before and after the image cropping process. Also the contrast and the brightness are adjusted.

3.5.3 Determination of the global position

The basic principle to determine the global position of the masks is the same for the CMM and the jig (see eq. 3.1 and 3.2). Here the CMM is used to position the telecentric camera reproducibly within few μm accuracy. The camera of the CMM alignment reconstruction is the fine tool like the surveyor is the fine tool for the jig alignment reconstruction. The combination of the large scale system and the fine tool allows an absolute position reconstruction of the mask position in a global coordinate system (see figure 3.23). Due to the cropping process an additional shift has to be added in the reconstruction, depending on where the images are cropped. The formulas used for position determination in the global coordinate system are:

$$\begin{aligned} x_G = {} & ((x_{\text{meas}} - x_{\text{offset}}) \cdot \cos(\phi_{\text{image}}) - (y_{\text{meas}} - y_{\text{offset}}) \cdot \sin(\phi_{\text{image}})) \cdot (-1)^n + \\ & x_{\text{calibration}} + x_{\text{camera}} + ((x_{\text{crop}} - x_{\text{image size}} \cdot 0.5) \cdot p + x_{\text{masksize}} \cdot 0.5) \end{aligned} \tag{3.12}$$

$$\begin{aligned} y_G = {} & ((x_{\text{meas}} - x_{\text{offset}}) \cdot \sin(\phi_{\text{image}}) - (y_{\text{meas}} - y_{\text{offset}}) \cdot \cos(\phi_{\text{image}})) \cdot (-1)^n + \\ & y_{\text{calibration}} + y_{\text{camera}} + ((-y_{\text{crop}} + y_{\text{image size}} \cdot 0.5) \cdot p - y_{\text{masksize}} \cdot 0.5) \end{aligned} \tag{3.13}$$

x_{meas} and y_{meas} correspond to the analysed position of the centre of the cropped image, that was performed by the online Rasnik analysis program. The offsets x_{offset} and y_{offset} are the offsets of the individual masks, that are calculated using equation 3.4. The picture rotation with respect to the camera is Φ_{image}. The sign factor $(-1)^n$ accounts for the different internal coordinate systems of the mask depending on the side it is positioned on (see fig. 3.23). For masks on the left side (-00, -04, -08) is $n = 0$, for masks on the right side (-02, -06, -10) is $n = 1$. The calibration parameters $x_{\text{calibration}}$ and $y_{\text{calibration}}$ correspond to the mispositioning of the camera compared to its nominal position, that is directly above the centre of the nominal mask positions. The determination of these calibration constants is discussed in section 3.5.4.
The position of the camera in the CMM coordinate system has to be transformed to the global coordinate system. Therefore the origin of the global coordinate system is determined in CMM coordinates. Since the origin of the global system was defined as the centre of the top edge of the large board (8), its position can be determined taking pictures of the L- and V- spacer and the corresponding position pins which are symmetrically placed on this edge. With these two pictures and a pixel size $p = 8\,\mu\text{m}$ the origin can be calculated precisely (Δx_{origin} and $\Delta y_{\text{origin}} = \sqrt{2} \cdot 8\,\mu\text{m} = 11.3\,\mu\text{m}$). Any global deviations in precision direction of the calculated origin to the real origin of the global coordinate system are corrected by the fitting method in the analysis (see 3.4.2). The last bracket in equations 3.12 and 3.13 contains the transformation of the centre position of the cropped image to the centre position of the original image. x_{crop} and y_{crop} correspond to the distance between the top left points of the cropped and original image. The size of the original images are $x_{\text{image size}}$ and $y_{\text{image size}}$ and the mask width or size of the cropped image is x_{masksize} and y_{masksize}. After the transformation to the global coordinate system the measured positions can be fit to their nominal positions extracted from figure 3.10.

3.5.4 Calibration

The underlying principle to determine the calibration parameters for the CMM is the same as for the jig. The residuals reconstructed in Saclay are used as reference measurements. Minimising the difference between the reference measurements and the reconstructed residuals using the CMM leads to calibration parameters for each individual mask.
Figure 3.26 shows the differences between the measured residual and the reference measurements before applying calibration corrections. The distribution for the non-precision direction shows a constant offset of -1.201 mm. Such an offset is not visible for the precision direction. Similar to the jig is the total width of the distribution in precision direction ($\Delta y = 0.11$ mm) a lot smaller than in non-precision direction ($\Delta x = 2.35$ mm). The results of the calibration are shown in figure 3.27. The constant offset is nullified for the differences between reference and measured residuals for the non-precision direction. The precision direction shows an excellent calibration result with a standard deviation of $6.4\,\mu\text{m}$ and a small total width of $\Delta y = 0.035$ mm. The spike structure for the non-precision direction corresponds to the four readout panels, that are used for the calibration. Figure 3.28 shows a zoomed in version of this histogram and the clearly resolvable four measurement sets.

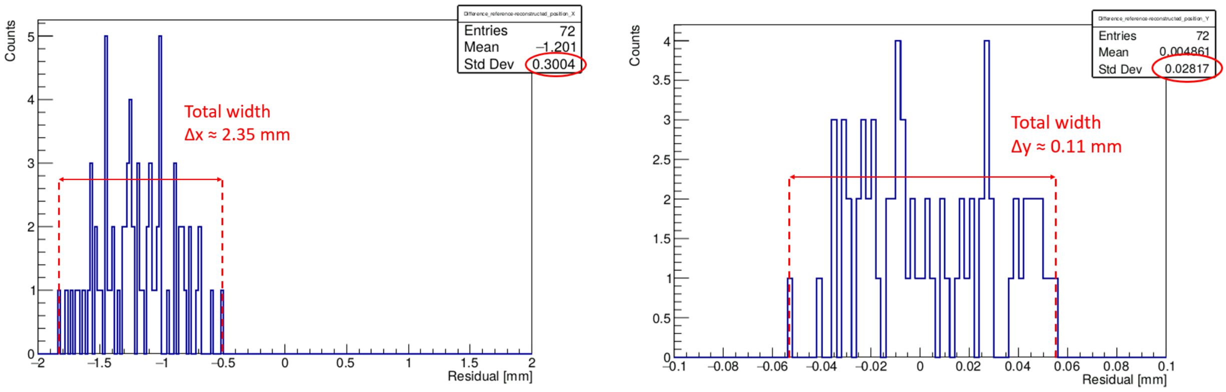

(a) Difference between residuals of the measurements from Garching and Saclay in **non-precision** direction before calibration. A constant offset of −1.201 mm is visible with a total width of Δx = 2.35 mm. The constant offset results from a constant mispositioning of the camera in x-direction.

(b) Difference between measured and reference residuals in **precision** direction before calibration. The entries are randomly distributed over the total width of Δy = 0.11 mm. A good calibration will result in a Gaussian shape centred around zero.

Fig. 3.26: Difference between residuals reconstructed by the CMM and reference measurements from Saclay for non-precision direction (left) and precision direction (right) before applying calibration corrections.

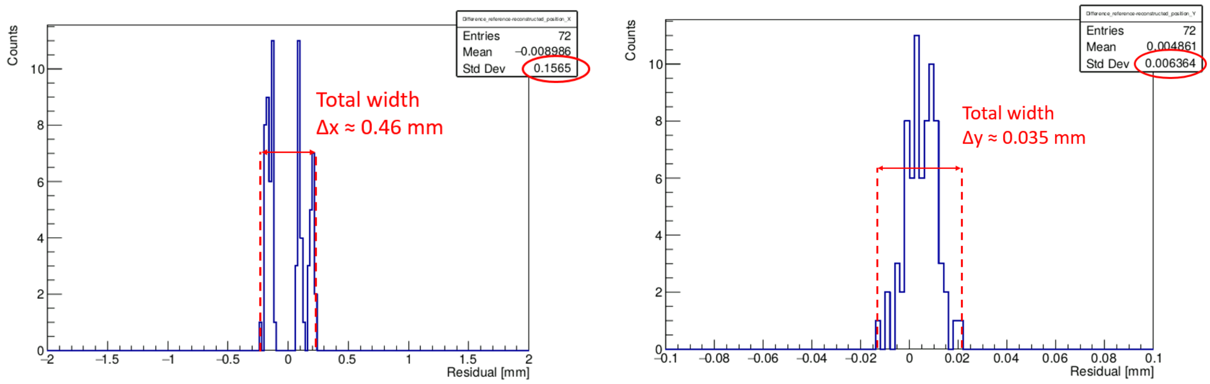

(a) Difference after the calibration between residuals of the measurements from Garching and Saclay in **non-precision** direction (x-direction). The individual readout layer differences are resolved. The distribution has a total width of Δx = 0.46 mm with a standard deviation of 0.156 mm.

(b) Difference after the calibration between residuals of the measurements from Garching and Saclay in **precision** direction (y-direction). A standard deviation of 6.4 µm of the Gaussian shape (total width of Δy = 0.035 mm) show a perfect result of the calibration.

Fig. 3.27: Difference after the calibration corrections between reconstructed residuals of the CMM and the reference measurements from Saclay (Dec. 2018) for all four readout layers (Eta 10 GS1/GS2 and Stereo 11 GS1/GS2).

The four marked areas in figure 3.28 correspond to the panels Eta 10 GS1 (II), Eta 10 GS2 (III), Stereo 11 GS1 (I) and Stereo 11 GS2 (IV). This separation of individual panels is not visible for the calibration measurements of the jig (see figure 3.14a) where single layer differences are distributed over the whole width and not in a small interval, separated from other layers. In addition to the separation of individual layers, a dependency on the gluing side (I and II for GS1, III and IV for GS2) of the panel is visible. The reason for this is the alignment method used during gluing.

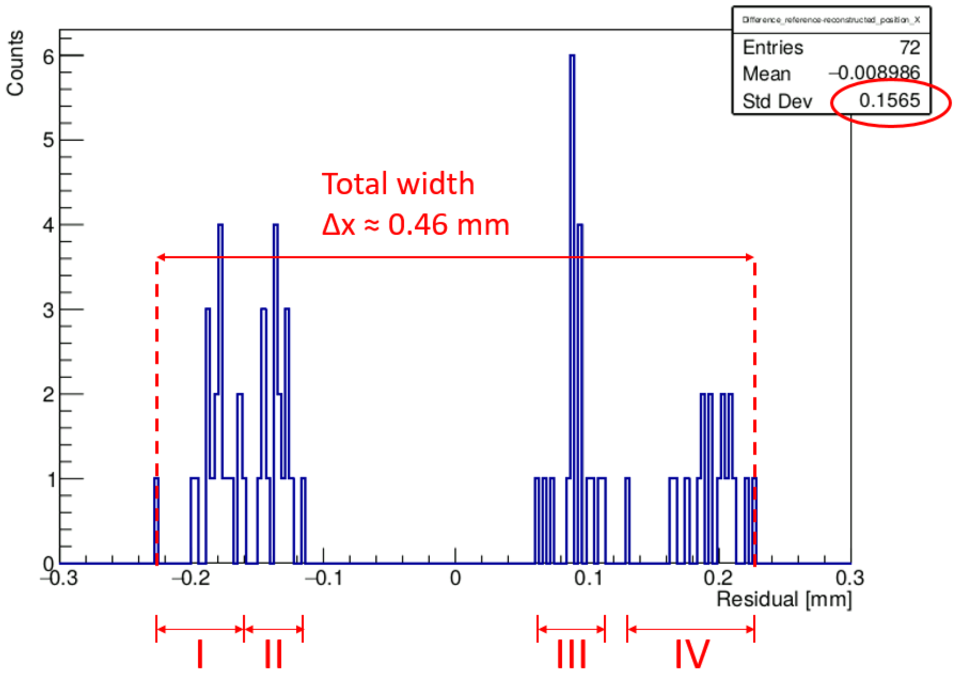

Fig. 3.28: Histogram with zoom of the difference after the calibration between the reference measurements and the reconstructed residuals in **non-precision** direction. All four panels, that are used for the calibration, are resolvable in this histogram, with Eta 10 GS1 (II), Eta 10 GS2 (III), Stereo 11 GS1 (I) and Stereo 11 GS2 (IV). Also a gluing side dependency is visible.

The readout layers are aligned by an alignment frame using a round and oval washer, that are glued on the PCBs. The alignment frame is aligned to the granite table cylinders using a V- and L-spacer. Then the V- and L-spacer are attached to the readout layer, they same way as the frame was aligned. In the next step the aluminum honeycomb and the second PCB layer are glued on top (see [**Herrmann 2016**]). Any mispositionings in x-direction during this gluing result in gluing side dependent shifts for the alignment measurement.
This leads to the idea of a gluing side dependent calibration of the CMM. To minimise possible errors due to low statistics, this approach has to be discarded. Additional reference measurements for a total of at least four readout layers per gluing side would be necessary to ensure a good calibration.
A comparison in the quality of the calibration between CMM and jig shows a better result for the CMM calibration for both directions ($\sigma_{x-\text{jig}} = 196\,\mu\text{m}$ and $\sigma_{y-\text{jig}} = 13\,\mu\text{m}$ of the jig compared to $\sigma_{x-\text{CMM}} = 156\,\mu\text{m}$ and $\sigma_{y-\text{CMM}} = 6\,\mu\text{m}$ of the CMM). However both calibrations are sufficiently good, with standard deviations similar to their measurement errors (see eq. 3.8 and 3.14) to consider both approaches as capable for alignment reconstruction. The measurement precision of the position determination using the CMM and the telecentric camera can be estimated by the thermal expansion coefficient of the main component of the readout boards (FR4) and the reconstruction precision of the Rasnik analysis algorithm. The thermal expansion of the panels is similar to aluminum with an linear expansion coefficient $\alpha = 23.1\,\frac{\mu\text{m}}{\text{m}\cdot\text{K}}$ (see subsec. 3.4.5). Typical temperature fluctuations over one day are less than 1.5 K (see B.7 in appendix B.3). The maximum expansion is measured using the top most and bottom most mask. Their distance is 1194.874 mm.

The measurement error of the position reconstruction using the analysis software is in the order of 4 µm (see figure B.8 in appendix B.3). This leads to the following measurement error in precision direction:

$$\begin{aligned}\Delta Y_{\text{meas}} &= \sqrt{\text{Analysis}_{\text{error}}{}^2 + \text{FR4}_{\text{deformation}}{}^2}\\ &= \sqrt{(4\,\mu\text{m})^2 + \left(\frac{1}{2}\cdot 1.5\,\text{K}\cdot 1.194874\,\text{m}\cdot 23.1\,\frac{\mu\text{m}}{\text{m}\cdot\text{K}}\right)^2}\\ &= 21.1\,\mu\text{m}\end{aligned} \tag{3.14}$$

The total error of the position reconstruction using the CMM is a combination of the measurement error and the standard deviation of the calibration:

$$\begin{aligned}\Delta Y_{\text{total}} &= \sqrt{\Delta Y^2_{\text{meas}} + \Delta Y^2_{\text{calibration}}}\\ &= \sqrt{\left(21.1\,\mu\text{m}\right)^2 + \left(6.4\,\mu\text{m}\right)^2}\\ &= 22.0\,\mu\text{m}\end{aligned} \tag{3.15}$$

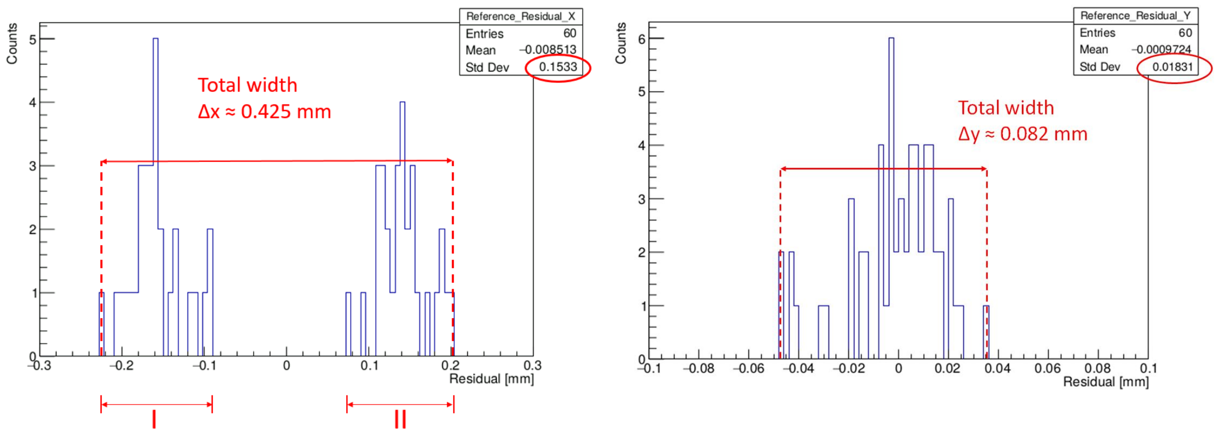

(a) Differences in **non-precision** directions. Gluing side dependent differences are resolved. Section I corresponds to GS1. GS2 is shown in section II. The standard deviation is in the same order as for the post upgrade calibration ≈ 153 µm (see figure 3.27a)

(b) The calibration in **precision** direction for the before upgrade measurements is worse than for after the upgrade with an agreement between reference and reconstructed residuals of 18.3 µm. It is within the measurement error of 21.1 µm.

Fig. 3.29: Difference between reconstructed residuals of the CMM before the camera upgrade and reference measurements from Saclay (Dec. 2018) for all four readout layers (Eta 10 GS1/GS2 and Stereo 11 GS1/GS2) after the calibration corrections.

A first set of alignment measurements of the positions of the three PCBs per anode plane using the CMM were done before the upgrade of the camera holder. As these panels were integrated into quadruplets a remeasurement after the upgrade was impossible. To analyse these measurements

(referred to as Before Upgrade (BU) measurements) a calibration is necessary. The used method is the same as for the post upgrade calibration and the jig. To compare the reference residuals from Saclay to the reconstructed measurements and to minimise the difference between both for all four readout layers simultaneously. The main difference between BU and post upgrade alignment measurements is the position of the camera in the CMM coordinate system. A second important difference is an image rotation by 90° or 270° respectively. For a correct analysis the images have to be rotated correctly and the position transformation of the centre of the images during cropping has to be done carefully. The results of the BU calibration are displayed in figure 3.29.
A calibration of similar quality as for the post upgrade CMM is achieved. In non-precision direction the distribution has a total width of $\Delta x = 0.425$ mm and the different gluing sides are resolvable (I for GS1 and II for GS2). The standard deviation in precision direction with 18.3 µm remains within the expected error of 21.1 µm. The reason for this wider spread (total width of $\Delta y = 0.082$ mm) compared to the new camera holder is the unknown temperature at which these calibration measurements were performed. It is possible, that the temperature exceeds the assumed typical temperature fluctuation of 1.5 K inside the hall containing the granite table. Also the missing three masks (502, 506 and 508) influence the quality of the calibration negatively.

3.5.5 Reconstruction example of one readout layer

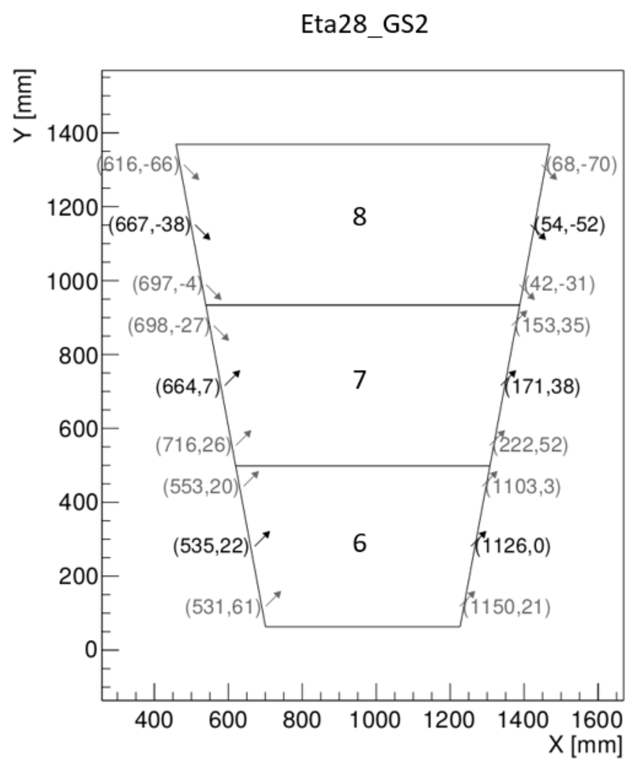

Fig. 3.30: Typical plot showing the residuals in x- and y-direction at each mask position for the alignment reconstruction using the CMM. Displayed are the results for Eta 26 GS2. A rotation of the boards 7 and 8 is visible (from left to right upwards) as well as a shrinkage of all three boards of about 17 − 60 µm. Board 6 is also rotated (from left to right downwards), but in the opposite direction as the other two boards.

Using the calibration described on the previous pages a typical alignment reconstruction for one readout layer is shown in figure 3.30. The residuals in x- and y-direction for Eta 28 GS2 are displayed.
Shrinkage or extension of a readout board can be seen in a difference between the top and bottom mask on one side. Board 6 is shrinked by about 41 μm (left side) and 18 μm (right side). The other two boards also show a shrinkage of 17 μm (board 7 right) and 39 − 62 μm (the three remaining sides).
The difference of the residuals between the left and right side of a board implies a rotation. For this only the central masks of the boards are investigated. Board 7 is slightly rotated by about 9.98 μrad. The mean rotation for board 8 is 4.08 μrad and for board 6 it is 7.90 μrad. The alignment reconstruction of this readout layer gives an insight on the very small misalignments and mechanical deformations, like shrinkage, which are all below the limit of 100 μm.

3.6 Comparison of jig and CMM alignment reconstruction

Both approaches for the in-plane alignment reconstruction are calibrated and working. Now a comparison of the reconstructed residuals from the jig and CMM method is discussed. The first comparison is done for the readout panels, that are used for the calibration (Eta 10 GS1/GS2, Stereo 11 GS1/GS2). Figure 3.31 shows the difference between the residuals at each mask position between jig and the post upgrade CMM in precision direction. The first thing to notice is the standard deviation of the distribution. With a deviation of < 13 μm the agreement of the different approaches within the total error (see equation 3.16) is proven. A mean value of less than 1 μm implies no constant offset between the two measurements. For the calculation of the total error of the calibration measurements only the standard deviations of their distributions are used (see figures 3.14b and 3.27b).

$$\begin{aligned} \Delta Y_{\text{total-Cal}} &= \sqrt{\Delta Y^2_{\text{jig-Cal}} + \Delta Y^2_{\text{CMM-Cal}}} \\ &= \sqrt{(12.6\,\mu\text{m})^2 + (6.4\,\mu\text{m})^2} \\ &= 14.1\,\mu\text{m} \end{aligned} \tag{3.16}$$

For a comparison of panels, that are not used for the calibration, the total error becomes:

$$\begin{aligned} \Delta Y_{\text{total}} &= \sqrt{\Delta Y^2_{\text{jig-total}} + \Delta Y^2_{\text{CMM-total}}} \\ &= \sqrt{(17.5\,\mu\text{m})^2 + (22.0\,\mu\text{m})^2} \\ &= 28.1\,\mu\text{m} \end{aligned} \tag{3.17}$$

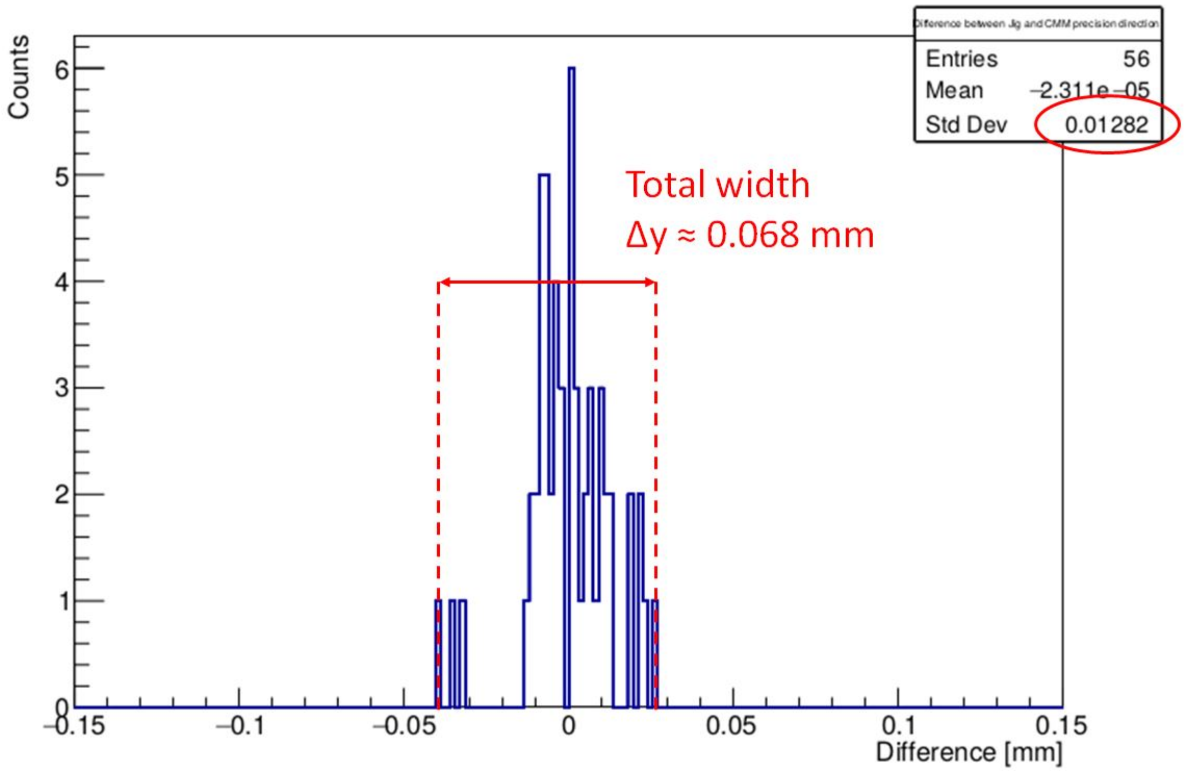

Fig. 3.31: Difference between the reconstructed residuals of the jig and CMM measurement in **precision** direction for the panels used for the calibration (Eta 10, Stereo 11). The standard deviation (12.82 μm) is within the expected error. A mean value of < 1 μm indicates no constant offset between the methods. The total width of the distribution $\Delta y = 0.068$ mm is smaller than $\pm 3\sigma$ (76.92 μm), which corresponds to a narrower distribution than normal distributed.

Figure 3.32 contains a total of 76 readout layers. Reconstructed residuals that were obtained with the old and new CMM camera setup are included. The standard deviation of the distribution is 29.7 μm with a mean value of −1.3 μm. This again implies no constant offset as a result of an systematic error. The standard deviation exceeds the expected error by 1.6 μm. This difference as well as the large differences inside the red box are a result of a mechanical deformation of the jig post calibration. One example of such a deformation is bending of the aluminum parts, where the spheres are placed on. A singular bending could be accounted for by a recalibration of the jig for this deformation. But several more deformations happened over the whole production time of the readout panels, such that a recalibration of this specific deformation is not possible anymore. The analysis of the measured mask positions was not done parallel to the production process, so these deformations were discovered months after the actual position measurement.

Differences for the masks of board 8 are all < 0.01 mm, for board 6 masks differences are > 0.01 mm. This results from different expansions of the panels for the different measurement methods. The residual differences for the central board (board 7) are equally distributed over the whole width. Therefore the systematic effect on the right side of the distribution arises from the wider spread of the differences of board 6.

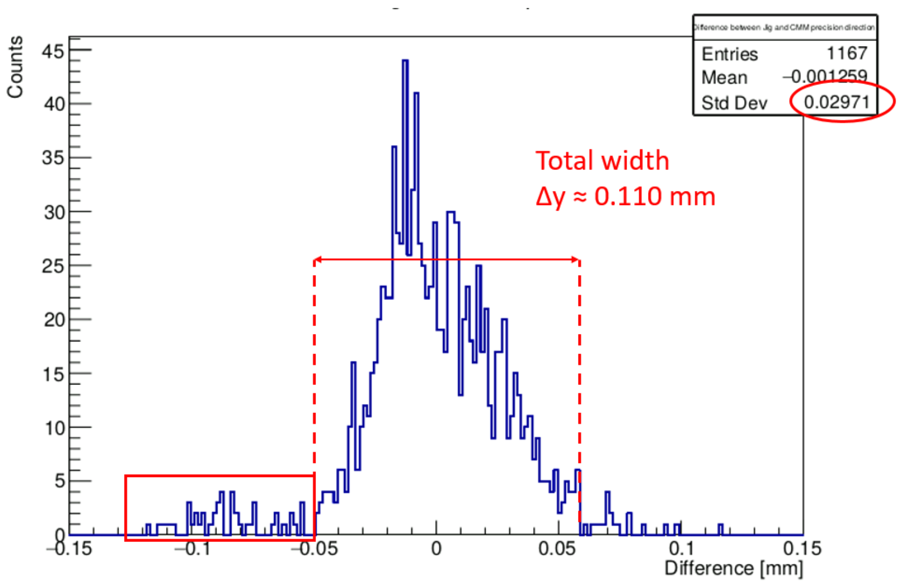

Fig. 3.32: Difference between the reconstructed residuals of the jig and CMM measurement in **precision** direction for 76 readout layers. The standard deviation (29.7 µm) exceeds the expected error of 28.1 µm. This and the large differences inside the red box arise from mechanical deformations of the jig after the calibration. An absolute mean value of < 2 µm indicates no constant offset between the methods. Differences for the masks of board 8 are all < 0.01 mm, for board 6 masks the differences are > 0.01 mm. This results from different expansions of the panels for the different measurements. Board 7 differences are equally distributed over the whole width. The systematic effect on the right side of the distribution arises from the wider spread of the differences of board 6.

The comparison of the non-precision direction for these two methods is only possible with restrictions. The main reason is the fitting method used for the determination of the residuals (see section 3.4.2). As described in that section the global minimisation process is done for the precision direction and the rotation. This is done to account for global displacements, for example between the jig and the readout panel. Another possibility is a false alignment of the panels on the granite table with respect to the alignment pins. For the non-precision direction these global misalignments are not corrected, thus leading to large differences between both methods. For completeness these differences are displayed in figure 3.33.

$$\begin{aligned}\Delta X_{\text{total-Cal}} &= \sqrt{\Delta X^2_{\text{jig-Cal}} + \Delta X^2_{\text{CMM-Cal}}} \\ &= \sqrt{(197\,\mu\text{m})^2 + (156\,\mu\text{m})^2} \\ &= 251\,\mu\text{m}\end{aligned} \tag{3.18}$$

$$\begin{aligned}\Delta X_{\text{total}} &= \sqrt{\Delta X^2_{\text{jig-total}} + \Delta X^2_{\text{CMM-total}}} \\ &= \sqrt{\left(\sqrt{(197\,\mu\text{m})^2 + (17\,\mu\text{m})^2}\right)^2 + \left(\sqrt{(156\,\mu\text{m})^2 + (17.4\,\mu\text{m})^2}\right)^2} \\ &= 252\,\mu\text{m}\end{aligned} \tag{3.19}$$

The expected error for the comparison of the calibration measurements is the obtained from the standard deviations of their distributions in figures 3.14a and 3.27a. For the comparison of all measurements the measurement uncertainties have to be included.

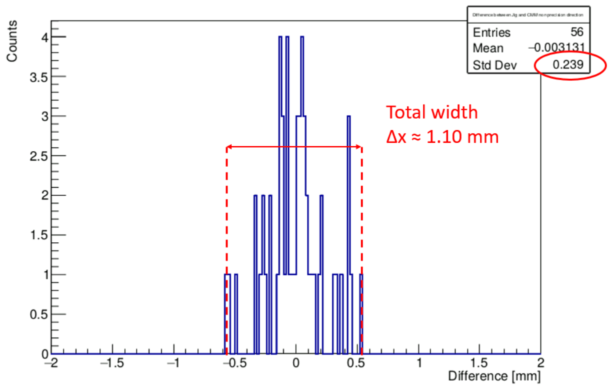

(a) Difference between the jig and CMM residuals for the calibration measurements (Eta 10, Stereo 11) in **non-precision** direction. Here the differences are within the error expected from the standard deviations of the two calibration distributions of 251 µm (see figures 3.14a and 3.27a)

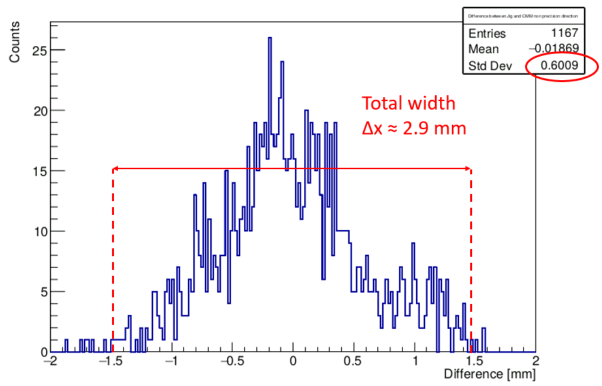

(b) Comparison of the residuals of 76 readout layers for the **non-precision** direction. The width of the distribution is larger than the expected error of 252 µm. The main reason for this is the missing global correction of the x-position. Misalignments between the jig and the readout panel are not accounted for in non-precision direction.

Fig. 3.33: Differences between the two in-plane alignment reconstruction methods for the residuals of the calibration measurements (left) and 76 readout layers (right) for the non-precision direction.

A distribution similar to a normal distribution is visible, yet due to the fitting method, the standard deviation for the comparison of all panels (600 µm) exceeds the error of 252 µm. Since the resolution in non-precision direction is in the order of 4 mm, uncertainties in this order are tolerable.

Chapter 4

Optical layer-to-layer alignment reconstruction

For the layer-to-layer alignment reconstruction of the SM2 quadruplets and the readout panels (Eta and Stereo), before the final assembly, two different approaches are evaluated. For the optical approach CCDs are used similar to the original Rasnik approach used for the MDT alignment in ATLAS (see sec. 3.1). The optical systems consist of CCDs, lenses and prisms to measure the Rasmasks. A second reconstruction method via determination of cosmic muon tracks in the Cosmic Ray Facility (CRF) is discussed in chapter 5.

4.1 Two-fold Rasfork

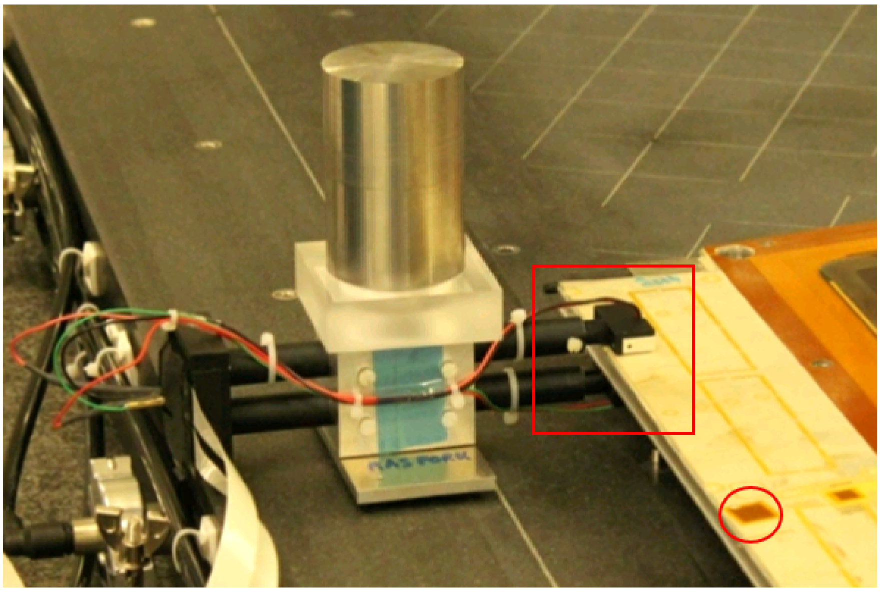

Fig. 4.1: Picture of the two-fold Rasfork during a panel measurement. The two prisms inside the red square measure the top and bottom side masks of one panel simultaneously. The red circle shows one Rasmask of the top layer to be measured. For stabilisation during the measurement a weight is placed on top of the fork.

The alignment of the two readout sides (GS1 and GS2) of a single readout panel (Eta or Stereo) is measured using a so-called two-fold Rasfork. This fork was developed and produced at Saclay for this very purpose (see [**Giraud 2017**]) and is shown in figure 4.1. It is a combination of two prisms to achieve parallel tracks for the light emitted by LED's. They have a distance according to the thickness of the readout panels between them. This method is also using the Rasmasks, that are placed outside of the active area on the rim of the readout panels. To measure the difference between two masks the panel is placed on top of chims to ensure the correct height for the fork. Then pictures are taken simultaneously and analysed by software. For a correct relative position reconstruction a calibration of the Rasfork is necessary. This calibration is performed before an alignment measurement using a precise calibrator (calirasfork), also developed at Saclay. For this calibration the heads of the fork are placed on the calibrator and analysed (see figure 4.2a). For the determination of the gap between the heads of the Rasfork, measurements at different heights of the calirasfork are done. The height positioning is done by placing stainless steel spacers of well defined thicknesses (0.1 mm, 0.2 mm and 0.3 mm) below the spheres of the calibrator. Combining the results of the measurements provides the calibration of the parallelity of the two beams passing through the prisms. Major problems, which may arise due to inattentive handling of the fork (e.g. dropping) have effects in the order of mm on the alignment measurements and need to be accounted for. This calibration is therefore mainly used as verification of the functionality of the fork as well as for fine-tuning of the calibration parameters for each individual panel measurement.

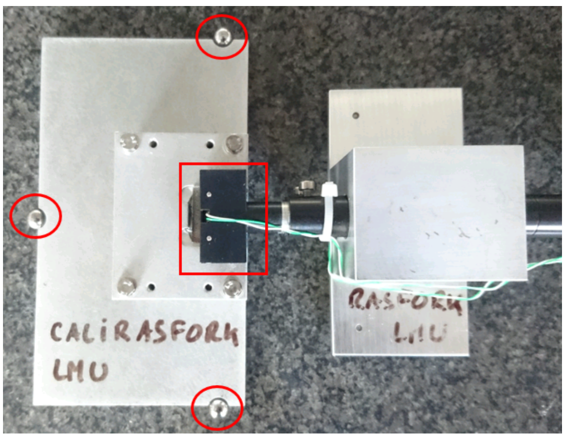

(a) Picture of the two-fold Rasfork placed on its calibrator. In the red square is the C-CCD of the two-fold Rasfork.

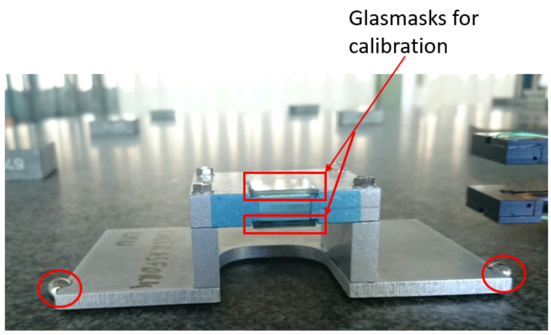

(b) Picture of the calirasfork for the two-fold Rasfork. Glasmasks inside the red squares are used for the calibration of the Rasfork. They are Rasmasks printed on glass with smaller squaresizes (120 µm) used for calibration.

Fig. 4.2: Pictures of the calibrator (calirasfork) and the two-fold Rasfork. The spheres in the red circles are used to calibrate the Rasfork, by investigating the parallelity of the two beams passing through the prisms. Therefore thin stainless steel spacers of well known thicknesses (0.1 mm, 0.2 mm and 0.3 mm) are placed below the spheres. Combining the measurement results for different heights allows the determination of the Rasfork calibration parameters.

The Rasfork provides information on the relative position of the two masks lying on top of each other. These results are then combined with the in-plane alignment reconstruction of one of the prior described methods to reconstruct the alignment of one whole panel. For a correct reconstruction it is necessary to account for the orientation of the panel, regarding the gluing side which lays on top/bottom accordingly. The 1-00 mask of the upper layer has the 1-02 mask of the lower layer beneath it and the Rasfork measures the positional difference between these two.

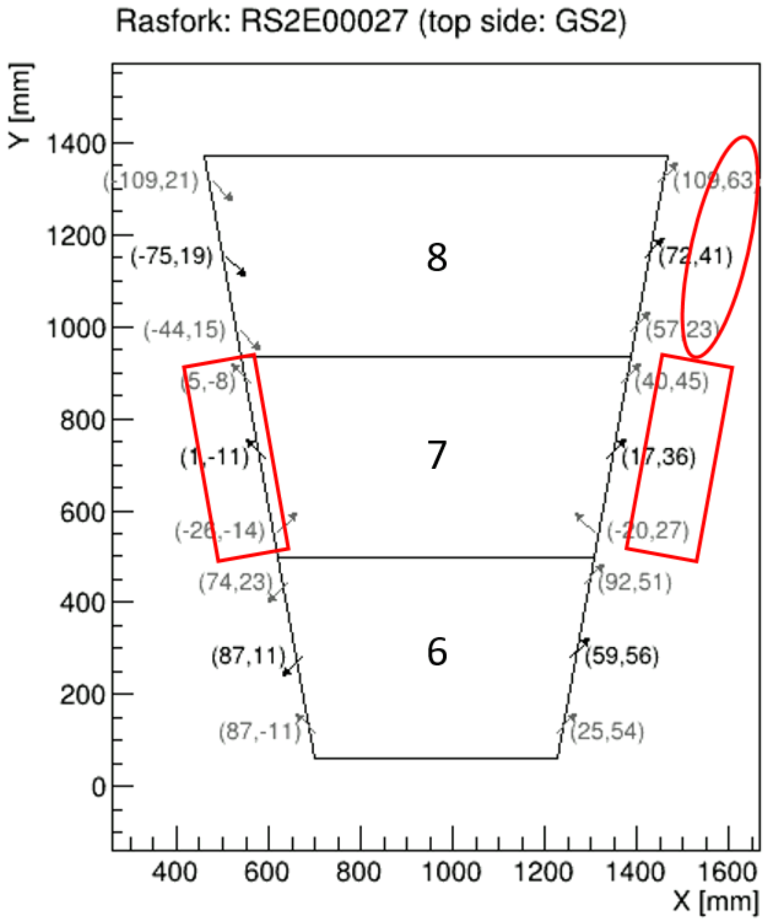

Fig. 4.3: Measurement results for Eta 27 using the two-fold Rasfork with gluing side 2 on top ($\Delta_{\text{non-prec.}}$, Δ_{prec}). The constant offset ($41-53\,\mu$m) between the left and right side in precision direction (red squares) indicates a rotation of the two readout layers with respect to each other. The difference between the top and bottom mask in the red ellipse indicates an elongation of one of the gluing sides to the other by 40 µm. For the left side of board 6 this is also visible.

Figure 4.3 displays the two-fold Rasfork measurement for Eta 27 with the gluing side 2 as top side. The residuals in the brackets are of the form ($\Delta_{\text{non-prec.}}$, Δ_{prec}). The constant offset between the left and right side in precision direction (red squares, $\approx 40-50\,\mu$m) indicates a rotation of the two layers to each other. Due to a difference between the top and bottom mask in the red ellipse an elongation of 40 µm between the two layers on board 8 (right) and of 34 µm on board 6 (left) is visible. The right side of board 7 shows a smaller elongation of 18 µm. Such a difference is also present for the non-precision direction on board 8.

4.2 Four-fold Rasfork

The four-fold Rasfork is a tool to measure the alignment of fully assembled Micromegas quadruplets. Similar to the two-fold Rasfork it consists of multiple prisms that are built on top of each other (see fig. 4.4). In this case the fork has four heads to measure all layers simultaneously (red square). In addition to the two-fold fork, the four-fold version is capable of measuring the alignment of the two readout panels with respect to each other. For the absolute alignment reconstruction of one module the absolute position reconstruction of one readout layer is combined with the relative position measurement of the four-fold Rasfork. The four-fold Rasfork has a calibrator working similarly as the calirasfork of the two-fold fork. Figure 4.5 shows a picture of the calibrator of the four-fold fork (cali4fork). The spheres on the cali4fork (red circles) and the four Glasmasks (red squares) are used for calibration. The principle to determine the calibration constants is the same as described in the prior section 4.1 by using spacers with well defined thicknesses.

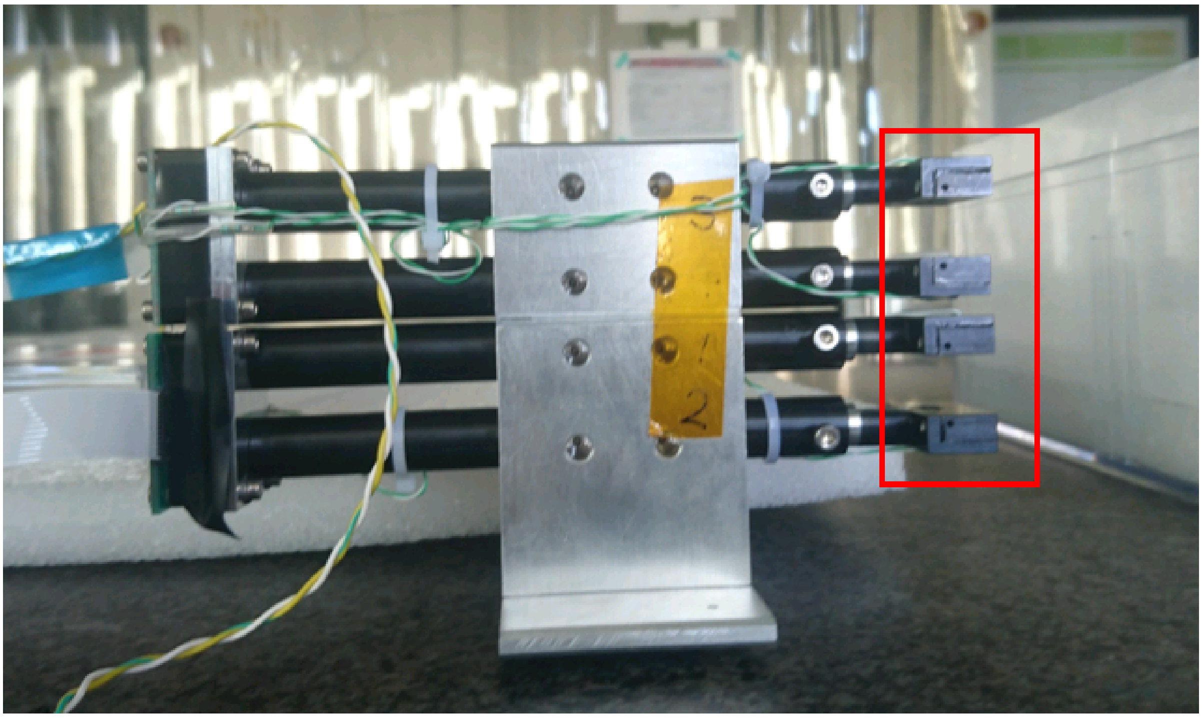

Fig. 4.4: Picture of the four-fold Rasfork. The four heads (red square) measure the relative position of all readout layers of one fully assembled Micromegas quadruplet.

The nomenclature of the four-fold Rasfork analysis is sketched in figure 4.6. The module is placed on a granite table with the Stereo panel as top side. This top panel is called B panel, whereas the bottom panel is the A panel. The residuals of the alignment reconstruction of the single panels are called B panel dif (Stereo) and A Bot (Eta). The A Bot residuals are compared to the two-fold Rasfork measurements in section 4.3. For an absolute position reconstruction one layer is taken as reference layer (Eta in layer). From this the absolute module alignment is reconstructed by combining the position measurements of the Eta in layer with the residuals of A Bot (Eta in - Eta out dif), B Bot (Eta in - Stereo in dif) and B Top (Eta in - Stereo out dif).

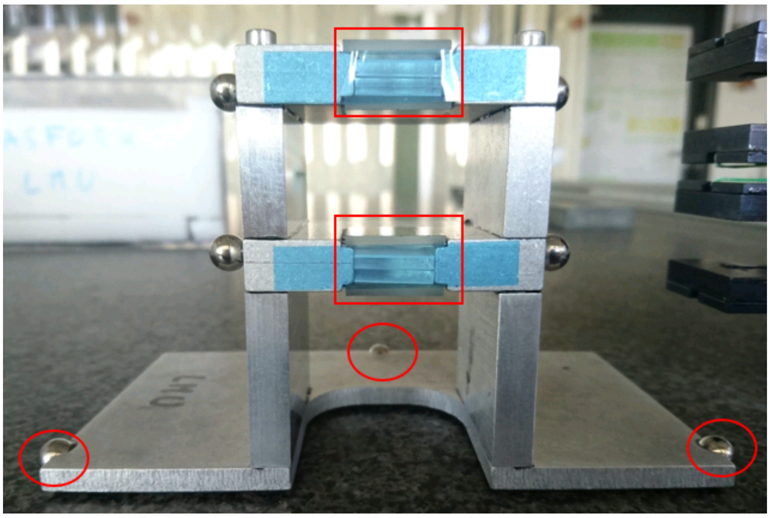

Fig. 4.5: Photo of the four-fold calibrator (cali4fork). The spheres (red circles) and four Glasmasks (two per red square) are used to calibrate the four-fold fork. The principle is the same as described in sec. 4.1. The other spheres were used during the production of the calibrator.

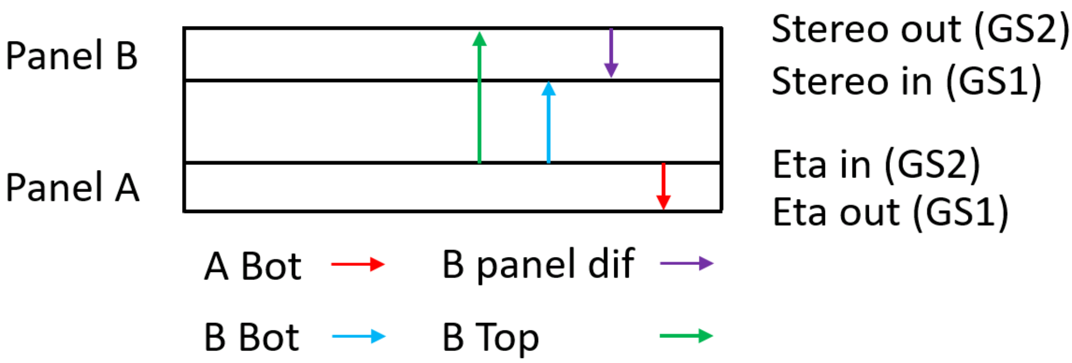

Fig. 4.6: Nomenclature for the four-fold Rasfork measurement. The module is placed on a granite table with the Stereo panel as top side. The top panel is the B panel in the Rasfork plots. The A Bot and B panel dif residuals correspond to the two-fold Rasfork measurements of the individual panels. For the absolute position reconstruction the Eta in layer is used as reference layer. From this the relative position to the other three layers is measured (see figures 4.7 and C.1-C.3 in appendix C).

The residuals displayed in figure 4.7 correspond to the difference between the two Eta layers of module 27. A comparison of those to the residuals in figure 4.3 shows no significant differences between the two forks. A complete discussion on the comparability of the two forks is done in the next section. The overall rotation between the boards (constant offset between left and right) as well as the elongation in precision direction (red squares) for board 8 (right) and board 6 (left) is visible.

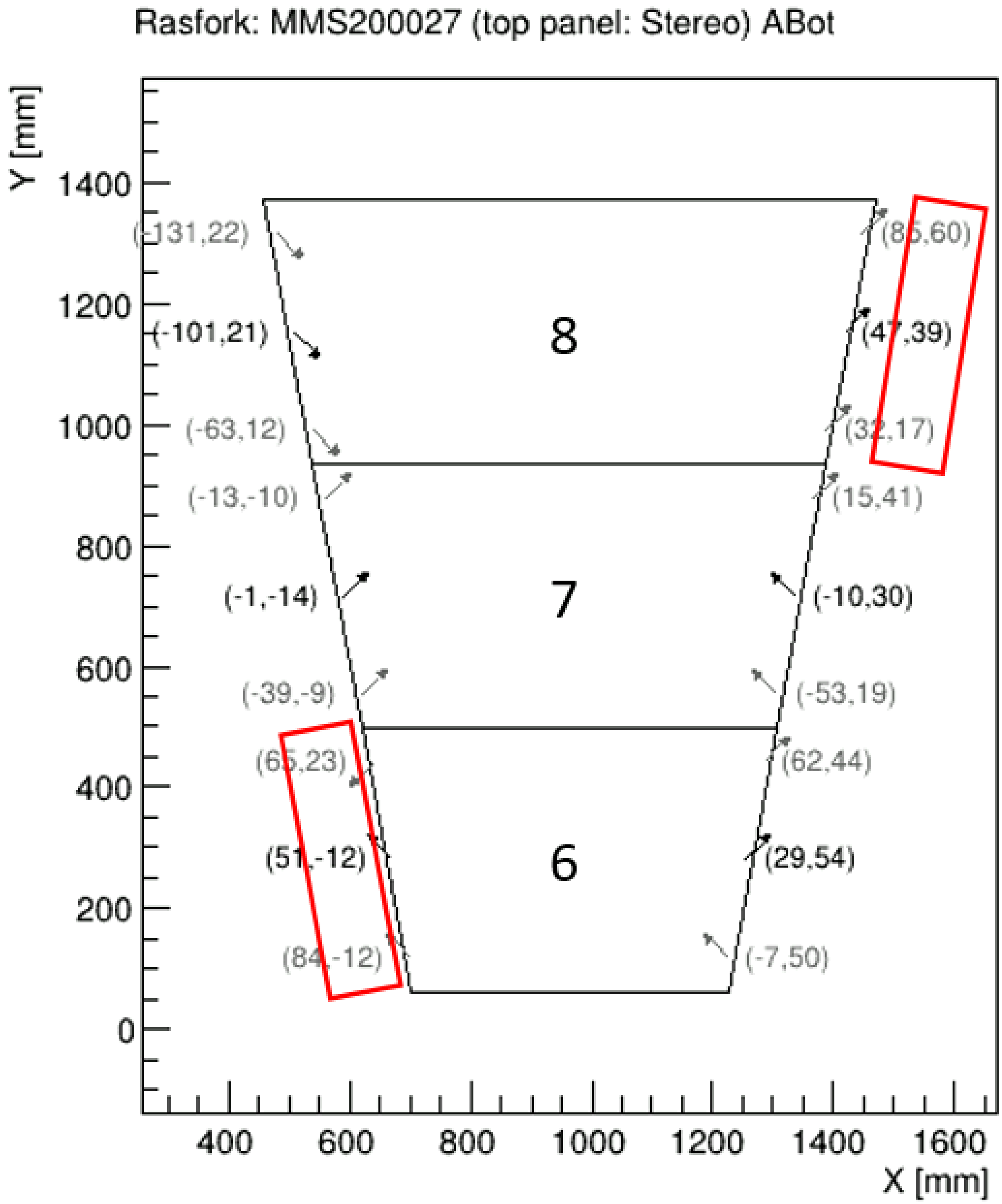

Fig. 4.7: Measured alignment of the two Eta layers of module 27. This plot is comparable to figure 4.3 of the two-fold fork measurement. It shows the same behaviour as discussed in sec. 4.1. Inside the red squares the elongation in precision direction of board 6 and 8 is visible. A more complete comparison of the two forks is done in sec. 4.3.

4.3 Comparison two-fold and four-fold Rasfork

A comparison of the two-fold and four-fold Rasfork measurements is done to prove the independent usage of either fork for comparisons with the CRF alignment reconstruction. Therefore the measured differences for the Eta panels are compared. Figure 4.8 shows the differences in precision direction. The mean difference between the forks is about 1 µm and the standard deviation is approximately 11 µm. The good comparability of both forks results in a small total width of Δy = 45 µm. The error of one Rasfork measurement can be estimated from the error calculated in [**Vogel 2017**] of a single C-CCD measurement (7 µm):

$$\Delta y = \sqrt{2} \cdot 7\,\mu\text{m} = 9.9\,\mu\text{m} \tag{4.1}$$

For the comparison of two forks this error is $\sqrt{2 \cdot (9.9\,\mu\text{m})^2} = 14\,\mu\text{m}$.

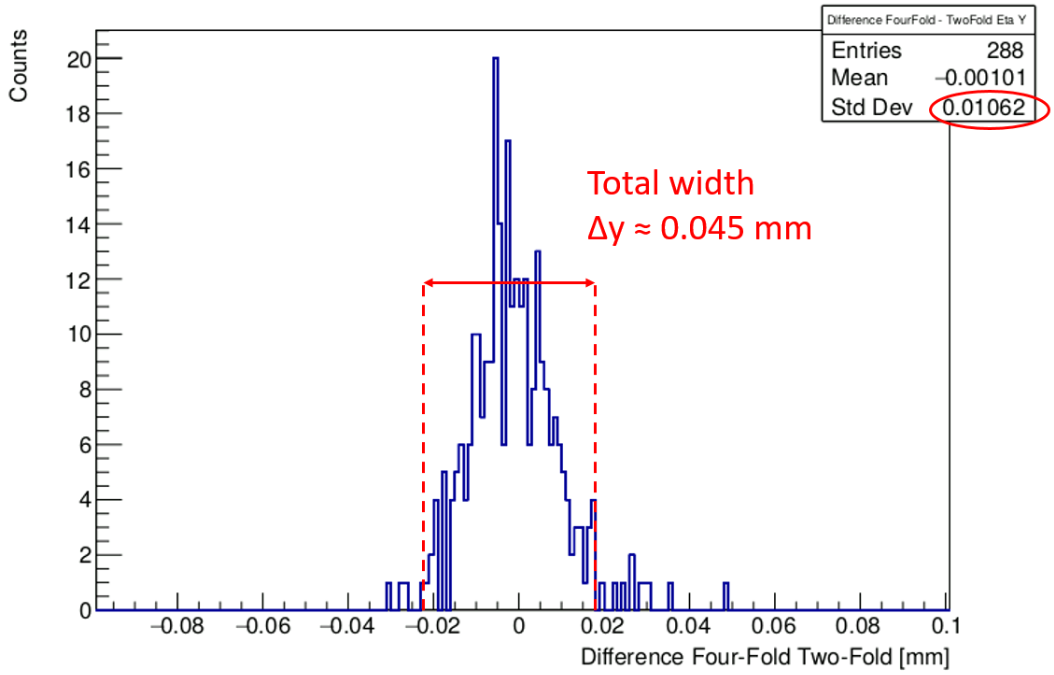

Fig. 4.8: Difference between four-fold and two-fold Rasfork residuals in **precision** direction for the Eta panels. Very good agreement of both forks with a small total width (Δy = 45 µm) and a standard deviation of 11 µm within the expected error of 14 µm.

The few differences with a larger spread may result from measurement obstacles. Since the four-fold Rasfork measurement is done after the final assembly of the quadruplets, some of the grounding screws are screwed through the masks (see figure 4.9). They are removed for the fork measurement, but the remaining hole may still influence the measurement. Another possibility is a wrong usage of the Rasfork for single masks. Since the vast majority of the differences remain within the expected error region (14 µm), the two fork measurements can be used independently for measurements or comparisons in precision direction.

The results of the comparison in non-precision direction are displayed in figure 4.10. The standard deviation of the distribution (16.7 µm) is slightly larger (2.6 µm) than the expected error (14 µm). One possible reason is the larger humidity dependent expansion in non-precision direction, since the measurements with the different forks were done at different days and during different environmental conditions (temperature and humidity). With a total width of 57 µm the distribution is wider than for the precision direction (45 µm). A constant offset between the two forks in non-precision direction of −27 µm shows a discrepancy of the two forks. This can be accounted for in future comparisons.

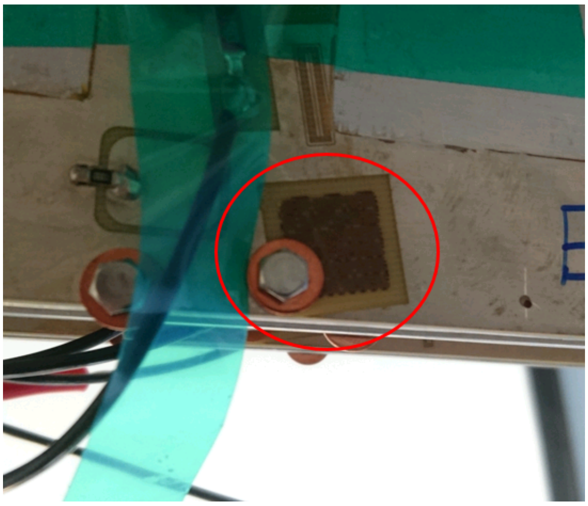

Fig. 4.9: Picture showing a grounding screw after the final assembly, a possible source for the larger discrepancies between two-fold and four-fold Rasfork.

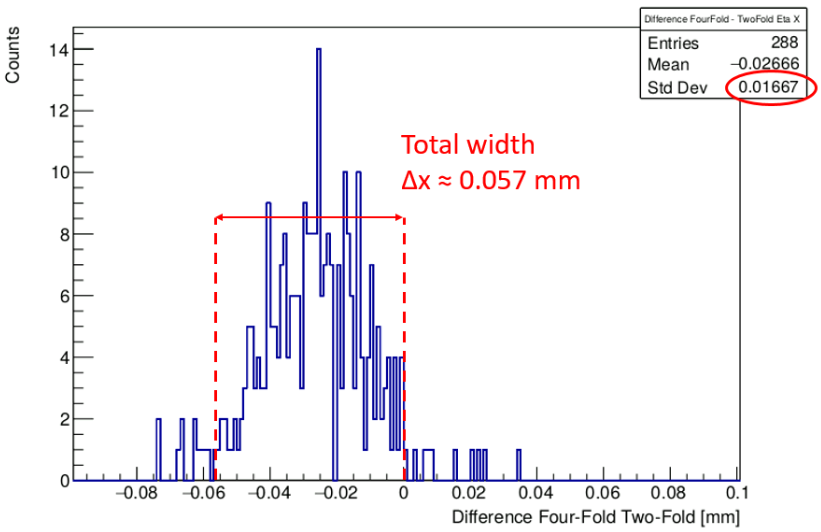

Fig. 4.10: Histogram of the differences between the four-fold and two-fold Rasfork in **non-precision** direction. Compared to the precision direction the total width is about 12 µm wider, yet sufficiently small. Measurements outside the distribution width are mismeasurements. The two forks have a constant offset in non-precision direction of −27 µm. The standard deviation of 16.7 µm is 2.6 µm larger than the expected error of 14 µm. A possible reason is the larger humidity dependent expansion in non-precision direction.

Chapter 5

Alignment reconstruction using cosmic muons in the Cosmic Ray Facility (CRF)

The Cosmic Ray Facility (CRF) in Garching near Munich is used to calibrate and test the efficiency of NSW Micromegas in relation to reference detectors using cosmic muons. For this thesis the reconstructed muon tracks are a reference to investigate the alignment of the Micromegas modules for the NSW Upgrade. A picture of the CRF is displayed in figure 5.1. The red brackets indicate the position of the two reference chambers. Inside the space of the blue bracket the test modules are placed. The trigger system is shown by the white brackets.

Fig. 5.1: Photo of the Cosmic Ray Facility (CRF) in Garching[1]. Shown are the two reference chambers (red), the space for the test module (blue) and the trigger system (white).

[1]Taken from the experimental particle physics homepage of the LMU: `https://www.etp.physik.uni-muenchen.de/research/detector-development/cosmic/index.html`

5.1 Layout of the Cosmic Ray Facility

Figure 5.2 is a sketch of the main components of the CRF. It consists of two layers of segmented scintillator detectors (green) forming a hodoscope. It is mainly used as a trigger system. While passing through the scintillators the muons excite the molecules inside the material. This leads to a deexcitation process via photon emission. The advantage of scintillators is a very fast signal ($\approx$ 10 ns) ideal for triggering. These photons are detected by photomultplier tubes (PMT), that are mounted to the end of each of the scintillators. When the photons reach the PMT, electrons are created at the photocathode via the photoelectric effect. Only muons, that trigger both the top and the bottom scintillator layer with the coincidence time of about 20 ns are counted. Additionally the segmentation of the scintillators provides a coarse position resolution in x direction ($\approx$ 10 cm).

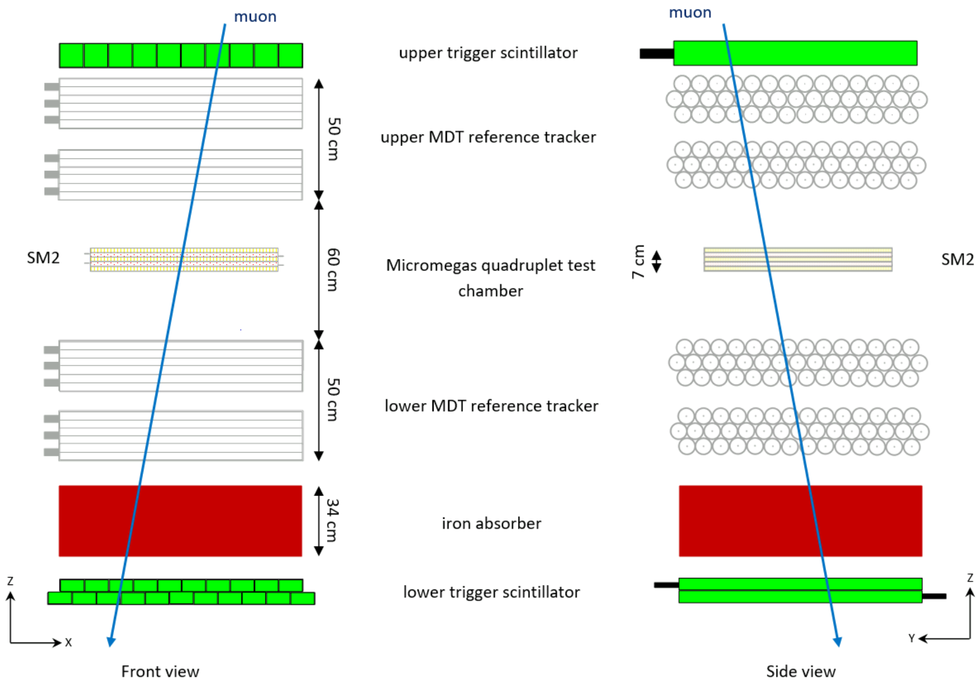

Fig. 5.2: Sketch showing the layout of the CRF containing two scintillator hodoscopes (green) as trigger, an upper and lower MDT reference tracking system (grey), the Micromegas module (yellow) as test chamber and an iron absorber (red) to discard low energy muons (< 600 MeV), that tend to scatter multiply. The absorption prevents the coincidental trigger of the top and bottom scintillators (taken from [**Herrmann 2019,p.14**], modified).

To harden the energy spectrum of the cosmic muons, a 34 cm thick iron absorber is positioned above the bottom scintillator layer. This absorber filters muons with low energy (< 600 MeV). Muons with such low energy tend to scatter multiple times while traversing the detector system and therefore have a scattered track. These tracks are much harder to reconstruct with a similar precision as straight tracks (±10 µm [**Herrmann 2019,p.16**]). By absorbing the muon before the second trigger layer, these particles are discarded. The main component of the muon track reconstruction is the Monitored Drift Tube (MDT) system (grey) made of multiple layers of drift tubes. Single MDTs are gas filled ionisation detectors consisting of a central gold plated tungsten anode wire in an aluminum tube as cathode. The Ar : CO_2 (93 : 7 vol%) gas inside the tubes is ionised by traversing muons. The electron-ion pairs are separated by an electric field between the wire and the tube. The electric field is high enough to accelerate the electrons to an extent at which secondary ionisation will occur. This results in an electron avalanche, which is detected at the wires. By combining the information of the two chambers a mean track can be reconstructed with a high precision of ±10 µm. The SM2 Micromegas module is placed flat in between the upper and lower reference tracking system to be investigated. The orientation of the module is chosen so that the readout strips of the SM2 module are parallel to the wires of the MDTs.

5.2 Reference track reconstruction and module alignment inside the CRF

The underlying principle of the alignment reconstruction of the SM2 modules using the CRF is a comparison of a reference muon track from the MDTs with the measured positions inside the four active Micromegas volumes of the module. The two reference tracks of the upper and lower MDT chamber are interpolated into the SM2. This interpolation of the reference tracks is done to the centre between the two MDT chambers. The Eta_out layer of the module is the bottom layer of the module in the CRF. The Stereo_out layer is the top layer. The interpolated tracks are then combined to obtain a single mean reference track used for investigation.

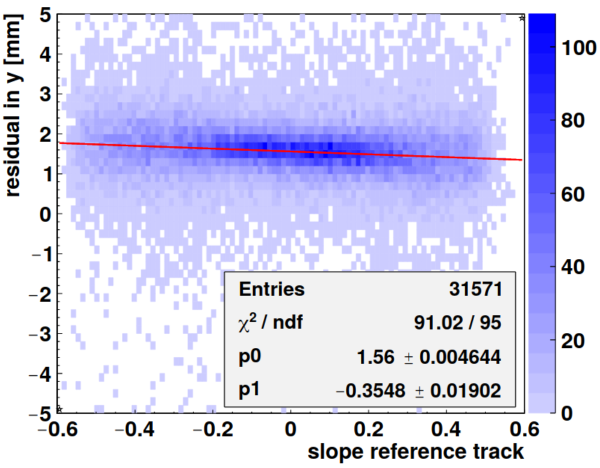

Fig. 5.3: Residuals between reference track and measured position inside the Micromegas module as a function of the slope of the reference track. Shifts in precision direction (y at slope 0) correspond to the first fit parameter. A shift perpendicular to the active area is given by the slope (taken from [**Herrmann 2019,p.55**]).

In addition to the precise reconstruction of the reference track the exact positioning of the module inside the CRF is important for alignment investigations. The goal is to achieve a precise parallel positioning between MDT wires and the readout strips of the module. Furthermore the rotation around x or y axis of the module needs to be determined.

To account for the rotation around the z axis the residuals between reference track and measured position inside the module are compared to the coarse position given by the scintillator hodoscope.

Any dependencies between those are interpreted as rotations around the z-axis and can be corrected. Typical values of this rotation are $\pm 3\,\frac{mm}{m}$ or $\pm 0.17°$.
To account for the rotation around the x and y axis the residuals are plotted as a function of the slope of the reference track (see fig. 5.3). The fit parameters of the distribution correspond to shifts in precision direction (p_0 at slope 0) and perpendicular to the active area (slope p_1). Combining these shifts with the rotation allows to account for the actual position of the module inside the CRF [**Herrmann 2019**].

5.3 In-plane residual determination

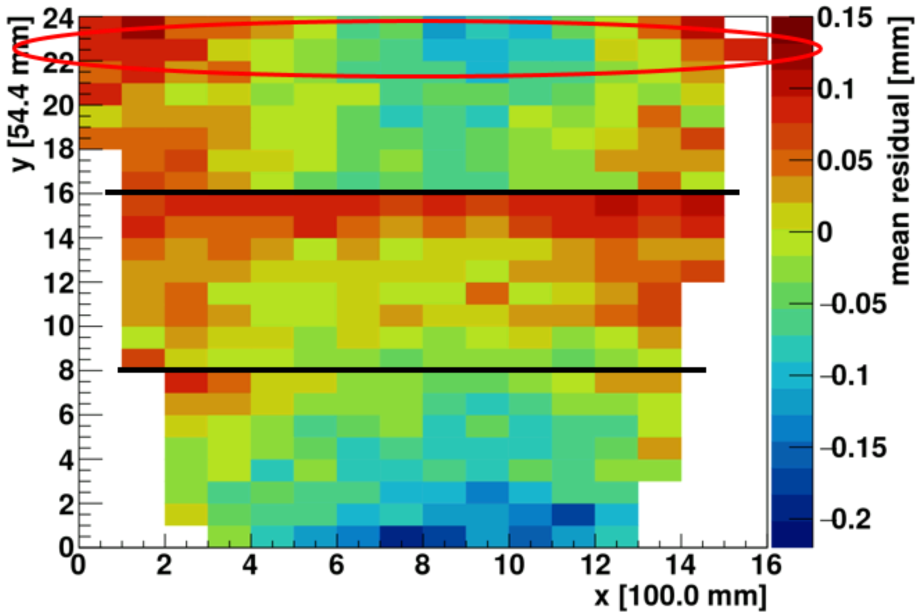

Fig. 5.4: Residuals in precision direction between reference track and measured position inside the Micromegas module for the Eta_out layer of module 18. The black horizontal lines indicate the board borders. The segmentation is corresponding to the readout electronics for the precision direction (128 strips with 425 µm pitch) and 100 mm for the non-precision direction (scintillator width). The red oval indicates an example of bent readout strips (see fig. 5.5). The colour pattern of the residuals of the two lower boards indicates a shrinkage for both compared to their nominal sizes in precision direction. This can be seen by the residual course from bottom to top of the individual board (e.g. y-slice 1-8 for board 6). This shrinkage is temperature and humidity dependent and happened before the gluing of the panel.

For the alignment reconstruction of the individual readout layers the measured position inside the detector is compared to the reference track. Figure 5.4 shows the residuals as a function of the position inside the detector for the Eta_out layer of module 18. The segmentation of this layer is chosen as 100 mm slices in non-precision direction (width of the scintillators) and as 54.4 mm in precision direction. The precision direction segmentation results from the readout electronics. One of these readout chips is capable of reading out 128 strips with a pitch of 425 µm resulting in a size of 54.4 mm. The two horizontal black lines indicate the two borders between the three boards. From bottom to top the boards are of type 6, 7 and 8.
The course of the residuals from bottom to top for board 6 and 7 indicates a shrinkage of the two

boards with respect to their nominal sizes in precision direction. The residuals in the centre of board 6 (slice 8 in x) decrease from about −0.2 mm to −0.025 mm. This results in a shrinkage of the board of about 0.175 mm. For board 7 this shrinkage is ≈ 0.1 mm. The shrinkage results from the temperature and humidity dependency of the FR4 material, the base material of the readout panels.

One major obstacle for the alignment reconstruction is the shape of the readout strips. The slice inside the red oval shows a strip bending from left to right. In figure 5.5 the projection of this slice 23 is displayed. The residuals for this slice can be fit with a second order polynomial. The resulting strip shape is shown in figure 5.6. Total strip bendings in the order of 0.200 mm were observed.

Due to the procedure of the panel gluing the endings of the readout strips are positioned correctly. Their connection position to the readout electronic is the same for straight and bent strips. For the comparison of the CRF residuals and the residuals reconstructed using optical methods in 5.5 this is important.

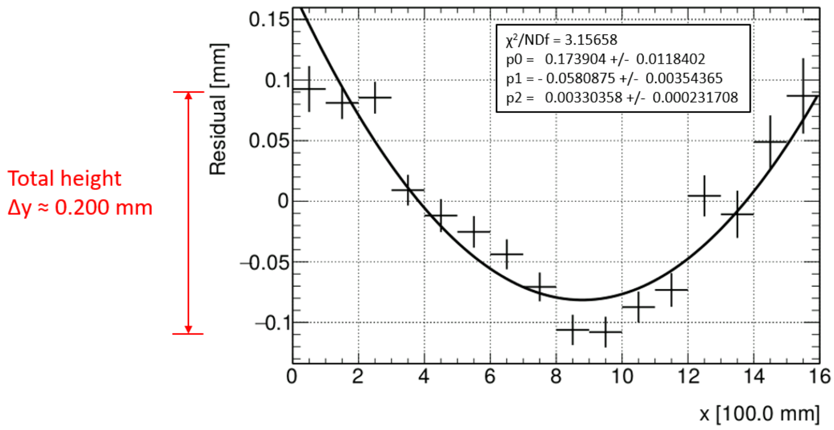

Fig. 5.5: Projection of the second to top slice (23) of figure 5.4. A total height of $\Delta y = 0.2$ mm corresponds to the total deformation of the readout strips. The residuals in precision direction are fit with a second order polynomial and correspond to a strip shape shown in figure 5.6.

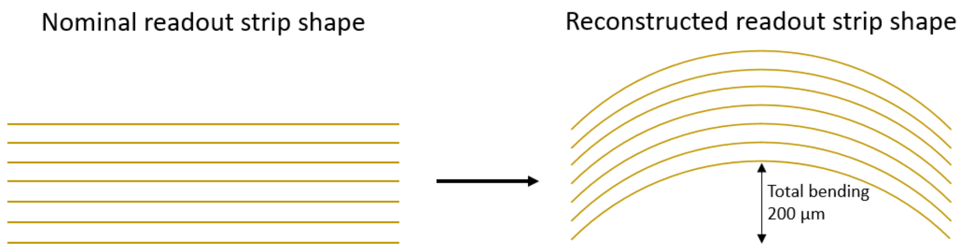

Fig. 5.6: Actual strip shape of the readout strips of board 8 of the Eta_out layer of m18. The endings of the readout strips are positioned correctly for straight and bent strips, only the middle of the strips deviates from the nominal positioning (not to scale).

5.4 Layer-to-layer residual determination

The layer-to-layer alignment reconstruction compares the reconstructed positions of the different detector volumes. The reference track is used to correct for inclined muon trajectories. The alignment of the two Eta layers of module 18 is displayed in figure 5.7.
Slice 19 in the red circle and slice 16 in y-direction correspond to problematics of the readout electronics. The two layers show an overall rotation with respect to each other. All slices in y direction show an increase of the residual from left to right. The differences are in the order of 50 µm for all three boards. This corresponds to board rotations around their centres of 17.9 µrad, 16.1 µrad and 14.6 µrad (for boards 6, 7 and 8 respectively).
For this layer-to-layer reconstruction it is important to keep track of the strip shape of the individual layers. Both readout layers of this plot show bent strip shapes on board 8 (fig. 5.4 and D.1 in the appendix D). Therefore the strip shape of the individual layers is not visible in the layer-to-layer comparison plot.

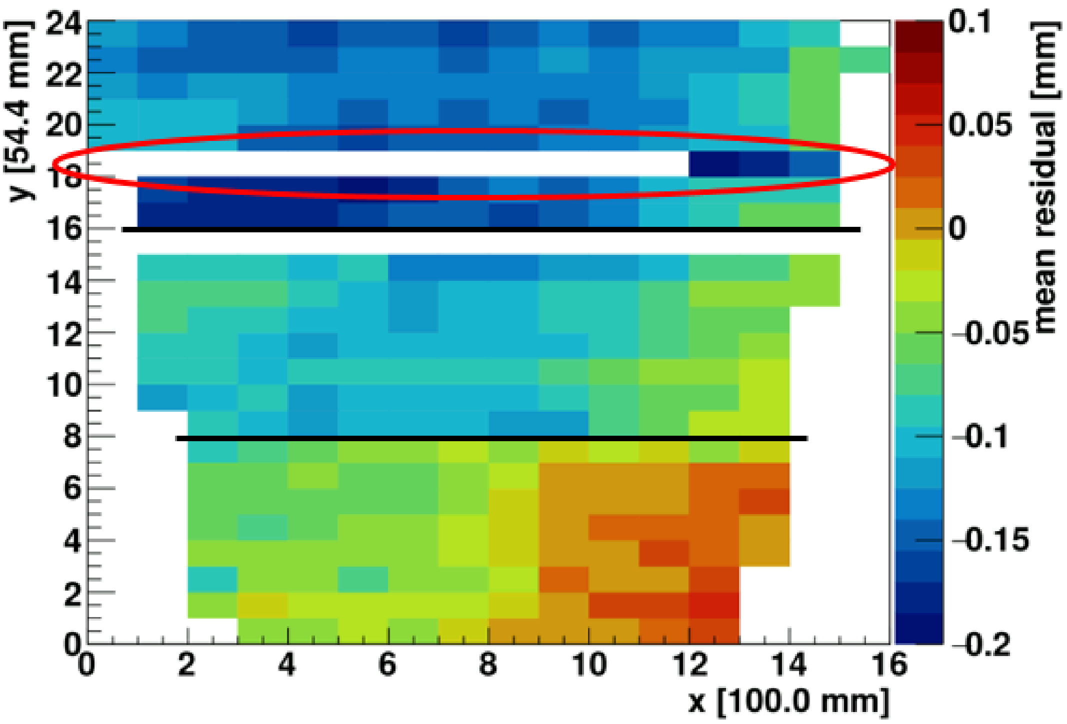

Fig. 5.7: Residuals between the two Eta layers of module 18. The increasing residuals from left to right over the whole active area indicate a rotation of one layer to the other. The difference is ≈50 µm corresponding to board rotations around their centres of 17.9 µrad, 16.1 µrad and 14.6 µrad (for boards 6, 7 and 8 respectively). Mispositioning of the electronics for the y-slices 16 and 19 result in a wrong residual reconstruction by 425 µm, corresponding to one strip pitch.

5.5 Comparability with optical alignment methods

Reconstructing with the CRF provides only information of the residuals inside the active area. The Rasmasks of the optical alignment reconstruction are positioned outside of the active area. Reconstructed residuals measured on the edges of the active area are chosen to be compared to the optical alignment reconstruction. The influence of the strip shape is small compared to residuals closer to the centre, since the shape is not uniform, but varies from board to board.
The used bins for the comparison with their corresponding masknames are displayed in figure 5.8. The inactive area of the detector is also sketched. Residuals are only provided for bins with sufficient entries (> 500 muon hits). The mean value of two bins is used for comparison with the optical methods, if both slices have sufficient entries (e.g. 1-04). For positions with one good entry and one with no reconstructed residual the single good entry is used (e.g. 1-02). Positions with no good entries are skipped (e.g. 1-00). An extrapolation of the active area positions to the mask positions is not performed.

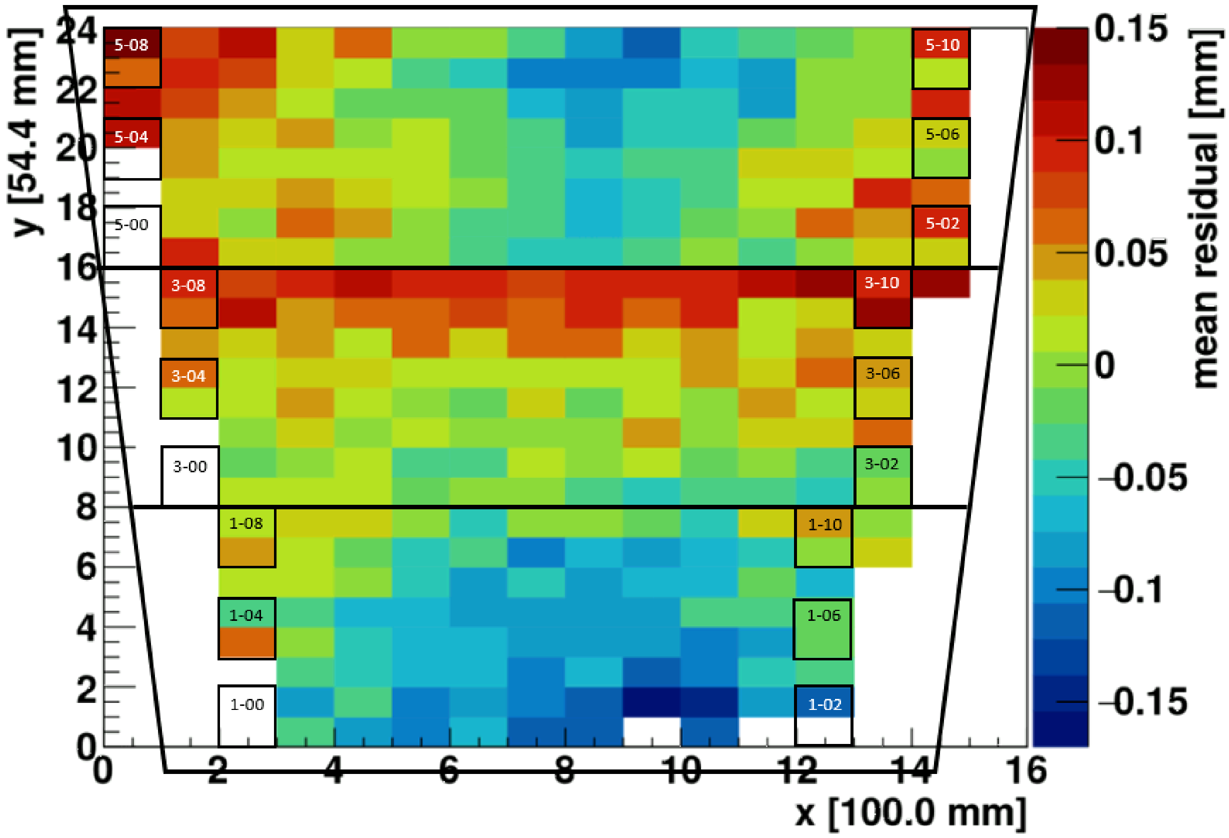

Fig. 5.8: Sketch of the panel inside the CRF including the inactive area. The drawn mask positions correspond to the values used for the comparison with the optical reconstruction. This means, values inside the active area reconstructed by cosmic tracks are compared to optical measurements of masks sitting outside the active area. An extrapolation to the mask position is not performed. Only bins with sufficient entries (> 500 muon hits) provide residuals. For comparison the mean value of two bins is used. Positions with single slices use this single residual. Mask positions with no valid entries are skipped.

To estimate the error arising from the strip shape of the readout strips the fit done in figure 5.5 is used. The fit is evaluated at the x positions 0 and 1. The difference of the residuals is an estimate of the strip bending inside the slice. The resulting residual error with parameters p_0, p_1 and p_2 from fig. 5.5 is:

$$\begin{aligned} \Delta Y_{\text{stripshape}} &= \frac{1}{2} \cdot (Y_1 - Y_0) \\ &= \frac{1}{2} \cdot ((p_0 + 1 \cdot p_1 + 1^2 \cdot p_2) - (p_0 + 0 \cdot p_1 + 0^2 \cdot p_2)) \\ &= \frac{1}{2} \cdot (119\,\mu\text{m} - 174\,\mu\text{m}) \\ &= -27.5\,\mu\text{m} \end{aligned} \tag{5.1}$$

5.5.1 In-plane alignment reconstruction: Comparison jig - CRF

Since both optical in-plane alignment reconstruction methods (jig, CMM) show consistent results (see sec. 3.6), the residuals reconstructed with the jig are compared to the CRF alignment reconstruction using the reference track. This comparison is done for all four readout layers in precision direction (see figures 5.9 and 5.10).

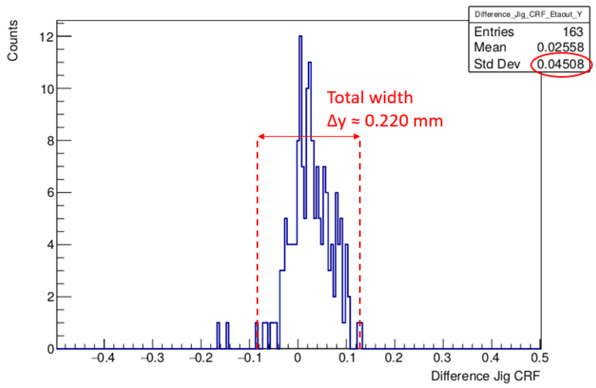

(a) Differences between the residuals of the jig and CRF reconstruction of the Eta_out layer (GS2). The standard deviation of 45 μm exceeds the calculated error of 43.1 μm by 1.9 μm. One possible reason for this is the difference in humidity and temperature that is not recorded. The distribution has a narrow total width of $\Delta Y = 220\,\mu\text{m}$. A central value of 26 μm shows a constant offset between the two methods.

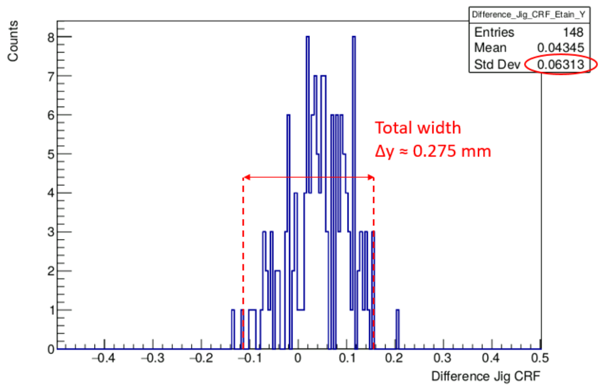

(b) Shown are the differences between the jig and CRF for the Eta_in layer (GS1). A standard deviation of 63 μm is not within the error of 43.1 μm. The distribution has a total width of $\Delta Y = 275\,\mu\text{m}$. The constant offset between the two methods is 43 μm.

Fig. 5.9: Residual differences in **precision** direction between the in-plane alignment using the jig and the CRF for the two Eta layers. The constant offsets arise from the different evaluation positions on the readout panel for the masks and the readout strips. Systematics of the CRF analysis are a second possible explanation of the different constant offset for different layers.

The total error of the comparison is the sum of the errors of the jig and CRF residual reconstruction. ΔY_{track} corresponds to the reference track error discussed in 5.1.

$$\begin{aligned}
\Delta Y_{\text{total}} &= \sqrt{\left(\Delta Y_{\text{jig}}\right)^2 + (\Delta Y_{\text{track}})^2 + \left(\Delta Y_{\text{stripshape}}\right)^2} \\
&= \sqrt{\left(29.6\,\mu\text{m}\right)^2 + \left(10.0\,\mu\text{m}\right)^2 + \left(27.5\,\mu\text{m}\right)^2} \\
&= 41.6\,\mu\text{m}
\end{aligned} \tag{5.2}$$

The standard deviations for the Eta_out (45 µm) and Eta_in (63 µm) layer residual difference distributions exceed the error of 41.6 µm by 1.9 µm and 19.9 µm, respectively. The main reason for this is the unknown uncertainty arising from different humidity and temperature conditions for both measurements. Total widths of 220 µm (Eta_out) and 275 µm (Eta_in) indicate a comparability of the two approaches within the 6σ limit of a normal distribution. The constant offsets of 26 µm and 43 µm for Eta_out and Eta_in respectively, result from the different evaluation positions of the residuals. The residuals of the optical alignment method are obtained outside of the active area. For the CRF alignment reconstruction the residuals are reconstructed inside the active volume. A second explanation are systematics in the CRF analysis for different layers. The wider distributions for Eta_in and the residual differences for the two Stereo layers (see fig. 5.10) arise from the positioning inside the CRF. The Eta_out layer is positioned at the interception point of the two reference tracks. This leads to the best agreement between the optical and cosmic alignment reconstruction.

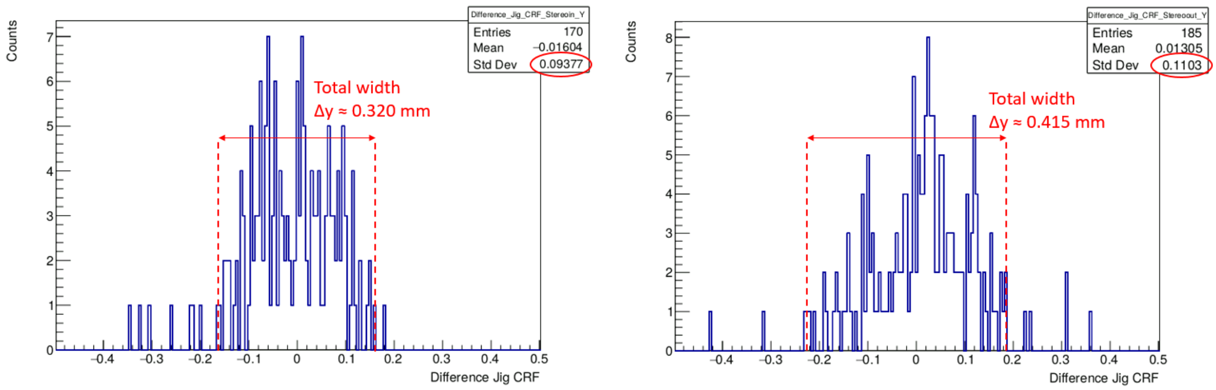

(a) Distribution of the differences between the residuals of the Stereo_in layer (GS1). The distribution has a total width of ΔY = 320 µm with a standard deviation of 94 µm. An agreement within the error (41.6 µm) is not visible.

(b) Differences between jig and CRF for the Stereo_out layer (GS2). A total width of ΔY = 415 µm and a standard deviation of 110 µm result not in an agreement of the methods within the error of 41.6 µm.

Fig. 5.10: Residual differences in **precision** direction for the two Stereo layers between the optical alignment reconstruction method using the jig and the CRF alignment reconstruction. Constant offsets result from the different evaluation positions of the mask residual and the readout strip residual. The main reason for the disagreement of the two methods is an additional rotation of the readout strips to their nominal rotation of ±1.5° (see subsec. 2.2.3). Different temperature and humidity environments for the jig and CRF reconstruction may also influence this.

The comparison for the Stereo layers shows no agreement within the error of 41.6 µm. The standard deviations of both (94 µm and 110 µm for Stereo_in and Stereo_out) distribution exceed this limit. The main reason is the problematic residual reconstruction inside the CRF for the Stereo panels. As described in subsec. 2.2.3 are the readout strips of Stereo boards rotated by ±1.5° to provide a coarse position resolution in non-precision direction. This rotation is not uniform for all boards and therefore differs. These additional rotations can not yet be determined precisely and need further investigations.
A perfect agreement between the two approaches is not visible for any readout layer. The main influence on this are the different humidity and temperature environments for the jig and CRF measurement. Also the position of the module inside the CRF compared to the interception of the two reference tracks influences the comparability. Layers further away from this point show a wider spread (with Stereo_out furthest away). Problems with the residual reconstruction of the Stereo boards inside the CRF need further investigations to improve their comparability.

5.5.2 Layer-to-layer alignment reconstruction: Comparison Rasfork-CRF

The layer-to-layer comparison is done for the Eta panels. Stereo panels are excluded due to the problematic in the correct position reconstruction inside the CRF described in the prior subsection. This results in an exclusion of the position residuals between the Stereo and Eta panel as well. For the comparison the residuals reconstructed using the four-fold Rasfork are used. As described in section 4.3 both Rasfork types (four-fold and two-fold) reconstruct the same residuals in precision direction.
An error estimation is done by adding the error of the Rasfork (see eq. 4.1) residual reconstruction to the error arising from the strip shape. Since two layers are compared and the strip shape of two different layers is not necessarily the same, the error from the strip shape is accounted twice. This leads to an error of:

$$\begin{aligned}
\Delta Y_{\text{total}} &= \sqrt{(\Delta Y_{\text{Fork}})^2 + \left(\sqrt{2}\cdot\Delta Y_{\text{stripshape}}\right)^2} \\
&= \sqrt{\left(\sqrt{2}\cdot 7\,\mu\text{m}\right)^2 + \left(\sqrt{2}\cdot 27.5\,\mu\text{m}\right)^2} \\
&= 40.1\,\mu\text{m}
\end{aligned} \tag{5.3}$$

Figure 5.11 shows the differences for the residuals in precision direction of the Eta panels between the four-fold Rasfork and the CRF layer-to-layer alignment reconstruction. The distribution has a total width of $\Delta Y = 290\,\mu$m and a standard deviation of 54 µm. The wider spread of the distribution compared to the expected error of 40.1 µm results only in a correlation and not in an agreement. The Gaussian shape of the distribution containing all values besides one in the 6σ limit supports this. A mean difference of 51.1 µm between the two approaches results from the different position the residuals are obtained from.

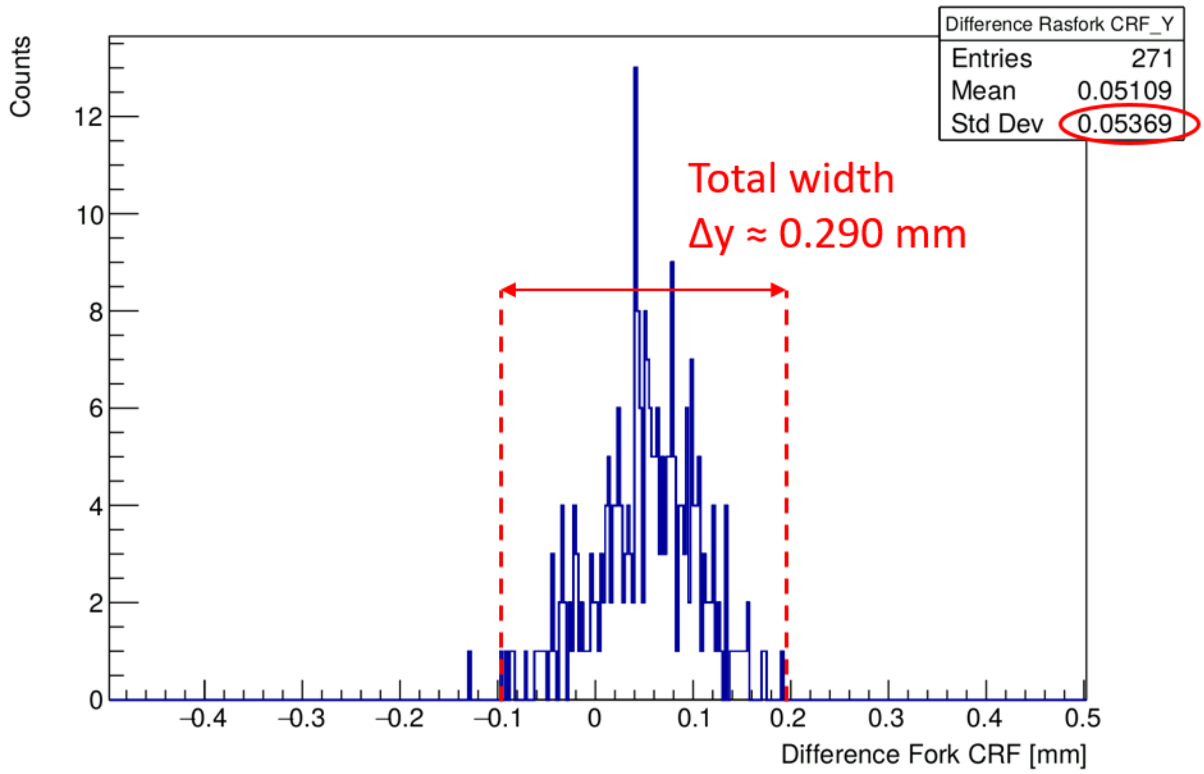

Fig. 5.11: Differences between the residuals in **precision** direction reconstructed by the four-fold Rasfork and the CRF. Displayed are the differences for the Eta panels. The distribution has a total width of ΔY = 290 µm and a standard deviation of 54 µm. This exceeds the expected error of 40.1 µm. A mean difference of 51 µm results from the different position evaluation outside (Rasfork) and inside (CRF) the active area.

Chapter 6

Conclusion

The SM2 Micromegas modules built for the NSW Upgrade of the ATLAS detector system require a precise alignment ($\approx 40\,\mu$m, see [**Kawamoto et al. 2013, p.106**]) in their precision direction. Alignment measurements regarding the alignment of the individual readout layers of the module as well as the alignment of the four readout layers with respect to each other were performed. To reconstruct the alignment of the SM2 modules two different approaches are used. These methods are an optical alignment reconstruction of the modules and an alignment reconstruction using the Cosmic Ray Facility (CRF) in Garching near Munich.
The optical alignment reconstruction based on coded chessboard-like masks (Rasmasks) analysed using CCDs is capable of reconstructing the absolute alignment of individual readout layers as well as the relative positioning of the layers with respect to each other. The optical in-plane alignment is performed with two different tools. The jig and the Coordinate Measuring Machine (CMM) are used as a large scale tool to position the fine measurement tool exactly and reproducibly. The fine tools for precision measurement ($\Delta Y_{\text{fine-tool}} < 10\,\mu$m) are a Contact-CCD (jig) and a telecentric camera (CMM). Both measurement approaches were calibrated by using reference measurements from Saclay to ensure a correct position reconstruction. Temperature studies of the jig were done to investigate the thermal expansion of the jig compared to the thermal expansion of the readout panel. Given enough time (>1 h) for acclimatisation the residual measurements can be done independently of the room temperature. The thermal expansion of the jig and the panel are correlated to be almost identical.
The jig reconstruction is done with a precision of $17.5\,\mu$m. For the CMM alignment reconstruction a resolution of $22.0\,\mu$m is achieved. A comparison of the two methods showed an agreement of the reconstructed residuals slightly exceeding the calculated error of $28.1\,\mu$m by $1.6\,\mu$m. One problem affecting the comparability of the two methods is the occasional mechanical deformation of the jig as well as the different temperatures and humidity during the measurements. The problem caused by the deformation can be solved by a recalibration of the jig.
The layer-to-layer alignment reconstruction based on Rasmasks is a combination of multiple optical prisms for simultaneous measurement of the Rasmasks of different layers. Therefore two versions of the so-called Rasforks were developed in Saclay. The two-fold Rasfork is used for the alignment of single panels (Eta and Stereo). The module alignment reconstruction is performed

by the four-fold Rasfork. This second fork is also capable of panel alignment. A comparison of the two forks shows an agreement of both forks of 10.6 μm with a measurement precision of 7 μm. A different approach of alignment reconstruction is using precise cosmic muon tracks in the CRF. A reference track determined by two Monitored Drift Tube reference chambers is compared to the measured position inside the detector volumes. This allows an alignment reconstruction for the individual layers and for the different layers with respect to each other. A residual reconstruction with a precision of 31.3 μm for the in-plane alignment and with a precision of 38.9 μm for the layer-to-layer alignment is achieved. Investigations using the CRF lead to the result of bent readout strips for some readout boards. Also the readout strips of the Stereo boards show an additional rotation to their nominal rotation of ±1.5°, that needs further investigations.

A comparability of the in-plane alignment reconstruction using the CRF and the jig could be achieved for the Eta layers. Uncertainties arising from systematics in the CRF analysis as well as different temperatures and humidity for the jig and CRF reconstruction lead to standard deviations for the two Eta layers of 45 μm (Eta_in) and 63 μm (Eta_out) exceeding the expected error of 43.1 μm. The agreement of additionally rotated Stereo layers is worse with standard deviations of 94 μm (Stereo_in) and 110 μm (Stereo_out) and show a wider spread of 94 μm and 110 μm.

The standard deviation of the layer-to-layer comparability between the CRF and the Rasfork exceeds the expected error of 40.1 μm by 12.4 μm. The Gaussian shape of the comparison distribution indicates a comparability of the two approaches, yet no perfect agreement has been achieved.

Optical alignment reconstruction methods and alignment reconstruction using cosmic muon tracks are implemented in the series production of SM2 quadruplets. They have been calibrated and are capable of reconstructing panels and modules with the desired resolution of < 100 μm.

Appendix A

ATLAS and NSW Upgrade

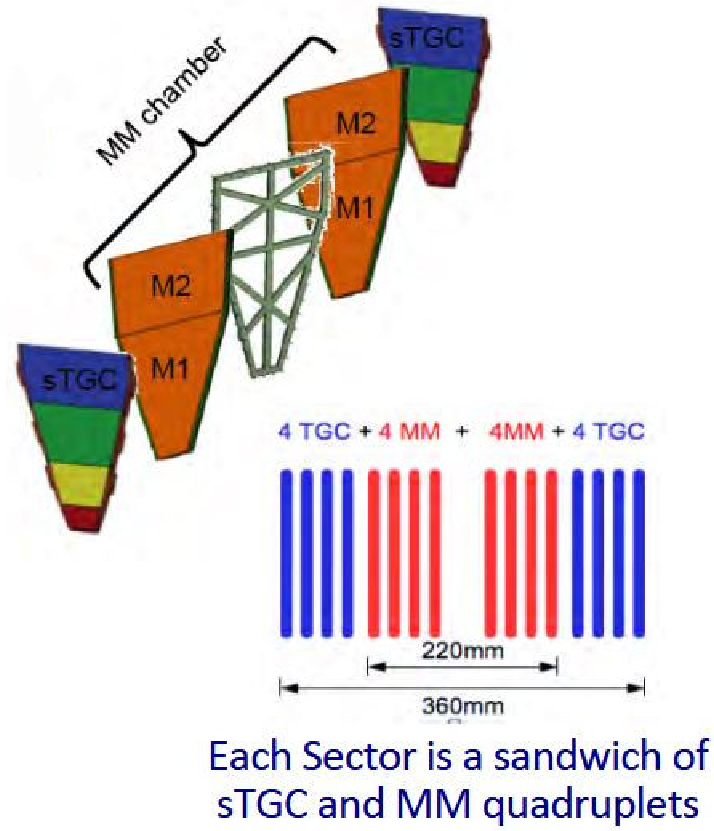

Fig. A.1: Slide from a presentation of [**Sampsonidis 2017**] showing the stacking of the Micromegas Modules (MM) and small-strip Thin Gap Champers (sTGC) for the NSW upgrade to maximise the distance between the two layers of sTGCs.

Appendix B

Optical in-plane reconstruction

B.1 Rasnik and LWDAQ for SM2 alignment

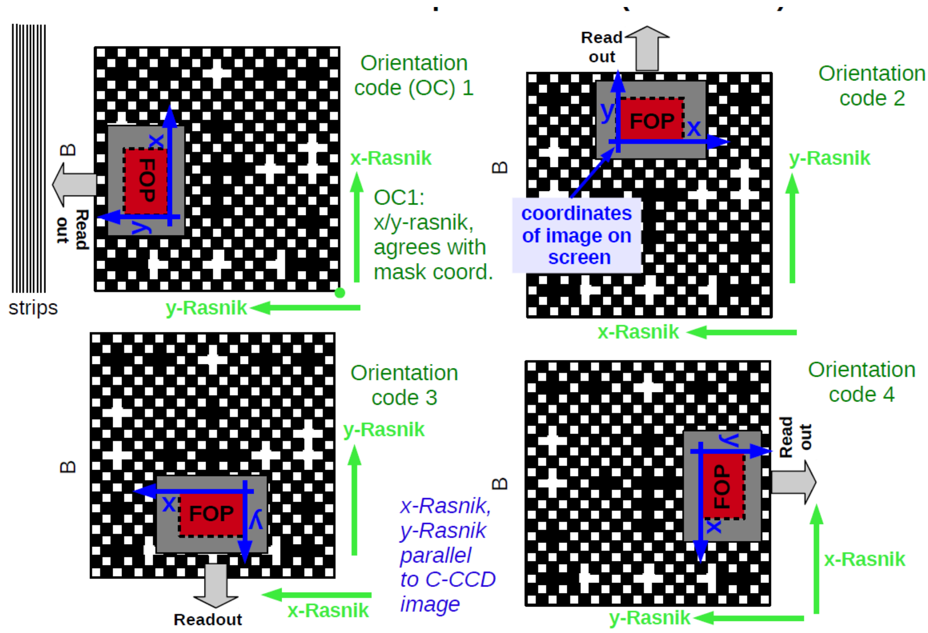

Fig. B.1: Figure showing the four different orientation codes, that are used for the analysis of Rasmasks with their according coordinate system orientation in the readout software[1].

[1]taken from Optical alignment tool with C-CCD (Hermann Wellenstein Tool), Micromegas Meeting 8.11.2016, p.21, Jeannine Wagner-Kuhr

B.2 Jig

```
510     65299.32 125017.56 1.001631 0.999607 -10.114 0.423 220.0 7.4 2 2590.0 1924.0
506     65603.18 77520.91 1.002931 0.998652 -7.878 0.574 220.0 7.4 2 2590.0 1924.0
506b    27423.02 51062.53 1.001432 0.999068 -9.575 0.564 220.0 7.4 2 2590.0 1924.0
502     66039.45 29709.00 1.002138 0.999462 -3.413 0.303 220.0 7.4 2 2590.0 1924.0
310     41456.75 125157.97 1.001901 1.000115 -13.233 0.582 220.0 7.4 2 2590.0 1924.0
306     41755.05 77472.81 1.001106 0.999638 -9.441 0.536 220.0 7.4 2 2590.0 1924.0
306b    27774.08 51200.29 1.002034 1.000297 -9.459 0.521 220.0 7.4 2 2590.0 1924.0
302     40905.98 29776.65 1.001615 0.999104 -17.461 0.422 220.0 7.4 2 2590.0 1924.0
110     18211.14 124504.57 1.002149 0.998304 -7.962 0.530 220.0 7.4 2 2590.0 1924.0
106     18820.86 77242.09 1.001773 0.999243 -1.893 0.414 220.0 7.4 2 2590.0 1924.0
106b    27625.36 51130.85 1.001935 0.999937 -7.563 0.476 220.0 7.4 2 2590.0 1924.0
102     17289.04 29693.71 1.001636 0.998761 -19.343 0.508 220.0 7.4 2 2590.0 1924.0

100     17602.53 6078.00 1.001349 0.999668 -6.145 0.465 220.0 7.4 2 2590.0 1924.0
104     18193.03 53439.97 1.001879 0.999616 -1.924 0.586 220.0 7.4 2 2590.0 1924.0
104b    27065.65 51040.07 1.001617 0.999639 -7.222 0.439 220.0 7.4 2 2590.0 1924.0
108     16994.81 100939.92 1.001544 0.999119 -15.393 0.470 220.0 7.4 2 2590.0 1924.0
300     41479.14 6076.09 1.001815 0.999717 -8.763 0.588 220.0 7.4 2 2590.0 1924.0
304     41464.85 53467.03 1.002178 0.999201 -8.703 0.548 220.0 7.4 2 2590.0 1924.0
304b    26990.21 50875.54 1.001837 0.999194 -9.128 0.485 220.0 7.4 2 2590.0 1924.0
308     41484.89 100937.35 1.001910 0.999881 -8.060 0.747 220.0 7.4 2 2590.0 1924.0
500     65834.58 380168.76 1.001737 0.999643 -7.824 0.444 220.0 7.4 1 2590.0 1924.0
504     65546.78 53289.09 1.001168 0.998872 -5.073 0.514 220.0 7.4 2 2590.0 1924.0
504b    27464.70 50738.56 1.001414 0.999454 -9.532 0.544 220.0 7.4 2 2590.0 1924.0
508     65100.90 100914.65 1.001534 0.998575 -10.164 0.919 220.0 7.4 2 2590.0 1924.0
```

Fig. B.2: Dataset for Eta 10 GS1 from July 2019 used for the calibration of the jig. The first column specifies the measured mask. Mask names containing a lower case b are small masks, that are dismissed for the alignment reconstruction analysis.

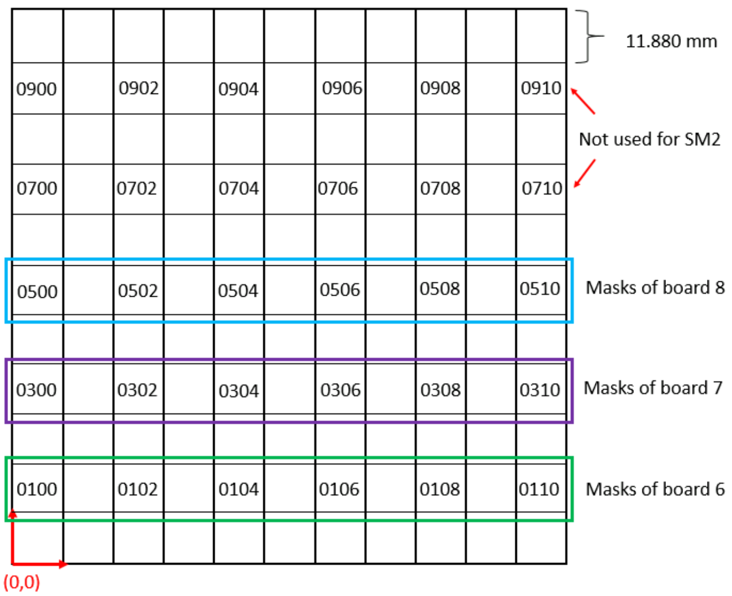

Fig. B.3: Sketch of the large mask containing all masks used for the SM2 alignment reconstruction. The length of one small square is the mask width of 11.880 mm. Using this individual offsets for the different masks can be calculated.

Mask Name	Eta 10 GS1		Eta 10 GS2		Stereo 11 GS1		Stereo 11 GS2	
510	-0.361	-0.097	-0.177	-0.043	-0.670	-0.072	-0.198	-0.011
506	-0.371	-0.074	-0.140	-0.017	-0.673	-0.051	-0.216	-0.005
506b	-0.367	-0.055	-0.130	-0.007	-0.666	-0.049	-0.199	0.016
502	-0.371	-0.046	-0.115	0.014	-0.677	-0.027	-0.208	0.018
310	-0.089	-0.009	-0.161	-0.011	-0.653	-0.038	-0.181	-0.046
306	-0.077	0.013	-0.169	-0.002	-0.682	-0.006	-0.185	-0.014
306b	-0.076	0.013	-0.166	0.000	-0.689	-0.003	-0.189	-0.005
302	-0.044	0.035	-0.150	0.016	-0.688	0.029	-0.156	0.034
110	-0.056	0.039	-0.069	-0.013	-0.146	-0.005	-0.482	-0.022
106	-0.046	0.055	-0.106	0.012	-0.157	0.024	-0.551	-0.003
106b	-0.041	0.047	-0.102	0.023	-0.144	0.040	-0.531	0.029
102	-0.001	0.080	-0.120	0.045	-0.140	0.055	-0.601	0.016
100	+0.085	+0.056	-0.011	+0.041	+0.540	+0.058	-0.024	+0.047
104	+0.126	+0.034	-0.010	+0.009	+0.566	+0.036	+0.005	+0.004
104b	+0.126	+0.032	-0.020	+0.017	+0.550	+0.044	-0.007	+0.026
108	+0.148	+0.024	-0.046	-0.007	+0.563	+0.005	+0.016	-0.026
300	+0.149	+0.007	-0.038	-0.005	-0.043	-0.000	+0.518	+0.036
304	+0.177	-0.010	-0.003	-0.015	-0.004	-0.025	+0.521	-0.005
304b	+0.172	-0.011	-0.005	-0.014	-0.025	-0.024	+0.505	+0.010
308	+0.177	-0.032	-0.014	-0.029	+0.008	-0.073	+0.520	-0.047
500	+0.079	-0.023	+0.400	+0.017	-0.009	-0.007	+0.444	-0.005
504	+0.117	-0.040	+0.436	-0.010	+0.017	-0.026	+0.459	-0.026
504b	+0.111	-0.033	+0.427	-0.003			+0.444	-0.017
508	+0.121	-0.052	+0.453	-0.034	+0.042	-0.050	+0.461	-0.062

Table B.1: Reference Residuals from Saclay full dataset. In the first column for each readout layer is the non-precision direction, whereas the second entry is in precision direction.

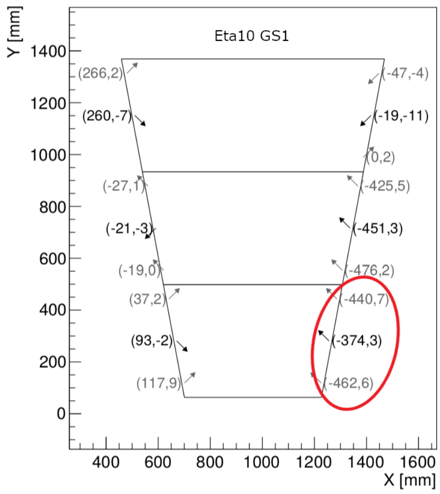

(a) Differences between calibration measurements and reference measurements from Saclay for each mask for Eta 10 GS1. The first number is in non-precision direction, the second number in precision direction

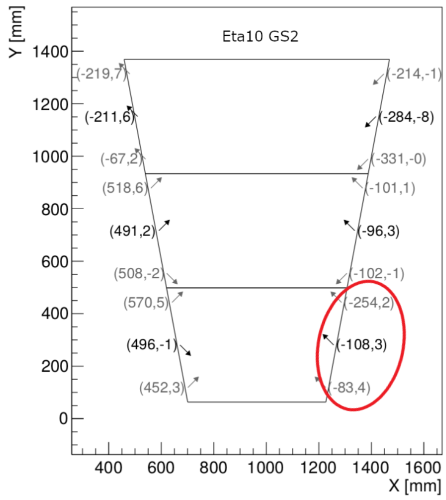

(b) Differences between calibration measurements and reference measurements from Saclay for each mask for Eta 10 GS2. The first number is in non-precision direction, the second number in precision direction

Fig. B.4: Difference between calibration measurements from July 2019 and reference measurements from Saclay for each individual mask for Eta 10. In the red circle are the measurements discussed in 3.4.3

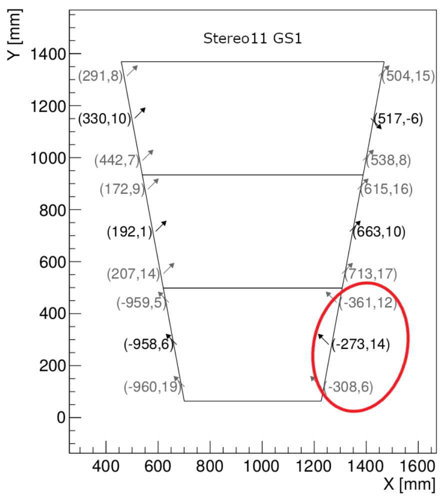

(a) Differences between calibration measurements and reference measurements from Saclay for each mask for Stereo 11 GS1. The first number is in non-precision direction, the second number in precision direction

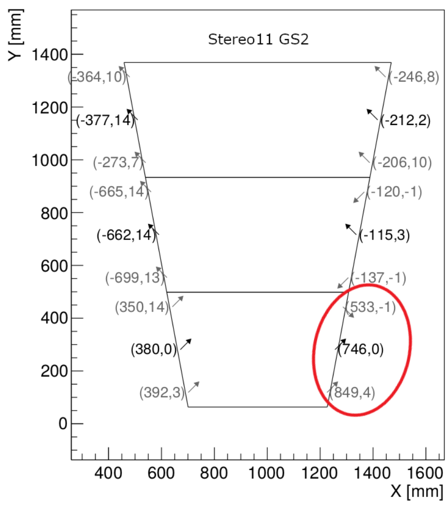

(b) Differences between calibration measurements and reference measurements from Saclay for each mask for Stereo 11 GS2. The first number is in non-precision direction, the second number in precision direction

Fig. B.5: Difference between calibration measurements from July 2019 and reference measurements from Saclay for each individual mask for Stereo 11. In the red circle are the measurements discussed in 3.4.3

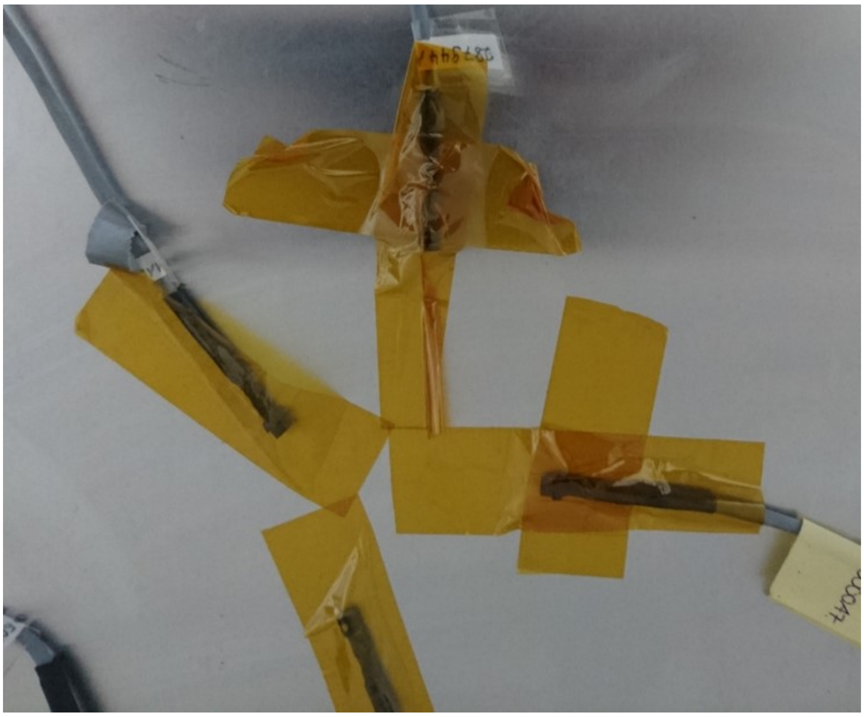

Fig. B.6: Four temperature sensors placed close to each other to check their comparability.

Maskname	mean value [μm]	standard dev. [μm]
100	68	26
102	74	30
104	27	23
106	16	24
108	-13	33
110	-19	38
300	34	23
302	46	25
304	-3	19
306	2	21
308	-35	22
310	-26	27
500	-6	25
502	-20	34
504	-30	21
506	-30	27
508	-95	42
510	-80	46

Table B.2: Mean values and standard deviations of the residual distributions in precision direction of all masks for all measured gluing sides (98) using the jig.

B.3 CMM

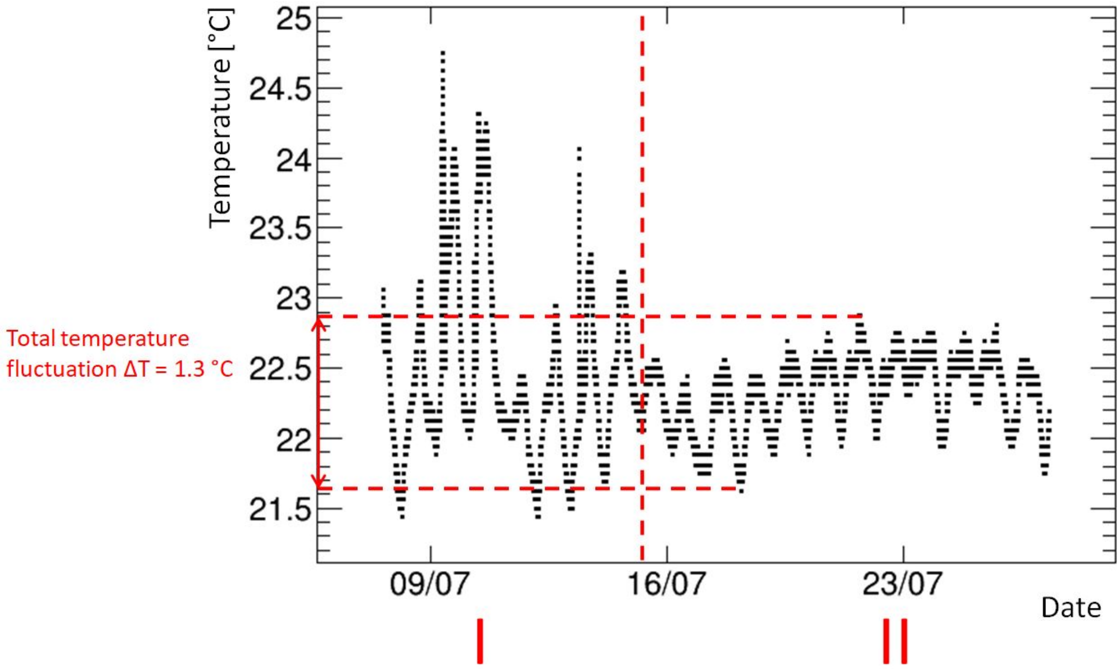

Fig. B.7: Temperature of the hall in which the CMM is located, monitored over about three weeks. The large fluctuations in section I correspond to open windows and doors close to the temperature sensors. Section II is a more controlled time period, with a temperature fluctuation of 1.3°C. Picture credits Sebastian Trost (LMU).

marker	2	0	124.81813	65.44572	0.43514	-0.00354	0.00077	0.00077	0.00000	0.00000	0.220	2
marker	3	0	77.30220	65.45215	0.43503	-0.00345	0.00081	0.00081	0.00000	0.00000	0.220	2
marker	4	0	51.25510	27.28565	0.43522	-0.00457	0.00097	0.00097	0.00001	0.00001	0.220	2
marker	5	0	29.78461	65.44579	0.43518	-0.00400	0.00106	0.00106	0.00000	0.00000	0.220	2
marker	6	0	124.81936	41.72454	0.43533	-0.00556	0.00000	0.00000	0.00000	0.00001	0.220	2
marker	7	0	3.36308	91.20335	0.43555	-0.00389	0.00087	0.00087	0.00000	0.00001	0.220	2
marker	8	0	51.24922	27.29139	0.43519	-0.00460	0.00203	0.00203	0.00001	0.00001	0.220	2
marker	9	0	285.00520	289.40518	0.43610	-0.00380	0.00334	0.00334	0.00000	0.00001	0.220	2
marker	10	0	124.83431	17.93877	0.43547	-0.00404	0.00103	0.00103	0.00000	0.00001	0.220	2
marker	11	0	77.29696	17.92437	0.43517	-0.00509	0.00410	0.00410	0.00000	0.00001	0.220	2
marker	12	0	51.25944	27.28469	0.43556	-0.00477	0.00038	0.00038	0.00001	0.00002	0.220	2
marker	13	0	29.80582	17.94835	0.43537	-0.00596	0.00000	0.00000	0.00000	0.00001	0.220	2
marker	14	0	6.07728	17.92539	0.43511	-0.00561	0.00092	0.00092	0.00000	0.00001	0.220	0
marker	15	0	53.59388	17.93085	0.43570	-0.00318	0.00240	0.00240	0.00000	0.00001	0.220	0
marker	16	0	51.05359	27.48710	0.43554	-0.00336	0.00146	0.00146	0.00001	0.00003	0.220	0
marker	17	0	101.10798	17.91391	0.43480	-0.00065	0.00103	0.00103	0.00001	0.00001	0.220	0
marker	18	0	6.07703	41.69455	0.43528	-0.00401	0.00121	0.00121	0.00000	0.00001	0.220	0
marker	19	0	53.60040	41.69289	0.43538	-0.00344	0.00160	0.00160	0.00000	0.00001	0.220	0
marker	20	0	51.05087	27.49435	0.43526	-0.00333	0.00134	0.00134	0.00001	0.00002	0.220	0
marker	21	0	101.11917	41.69404	0.43527	-0.00392	0.00079	0.00079	0.00000	0.00001	0.220	0
marker	22	0	6.07473	65.45300	0.43507	-0.00353	0.00097	0.00097	0.00000	0.00000	0.220	0
marker	23	0	53.60011	65.45103	0.43504	-0.00369	0.00097	0.00097	0.00000	0.00000	0.220	0
marker	24	0	51.05690	27.49179	0.43495	-0.00351	0.00120	0.00120	0.00001	0.00001	0.220	0
marker	25	0	101.10895	65.44918	0.43517	-0.00386	0.00064	0.00064	0.00000	0.00000	0.220	0

Fig. B.8: Typical dataset analysed by the online Rasnik analysis. From left to right: measurement order, analysis code, x-position (in mm), y-position (in mm), magnification, rotation (in rad), x-position error (in mm), y-position error (in mm), magnification error, rotation error (in rad), squaresize (in mm), rotation used on picture before analysis (0 is no rotation, 2 is rotation by 180°). In the red circle is the largest position error of this measurement. Measurements of other panels show errors of the same order.

Appendix C

Rasfork

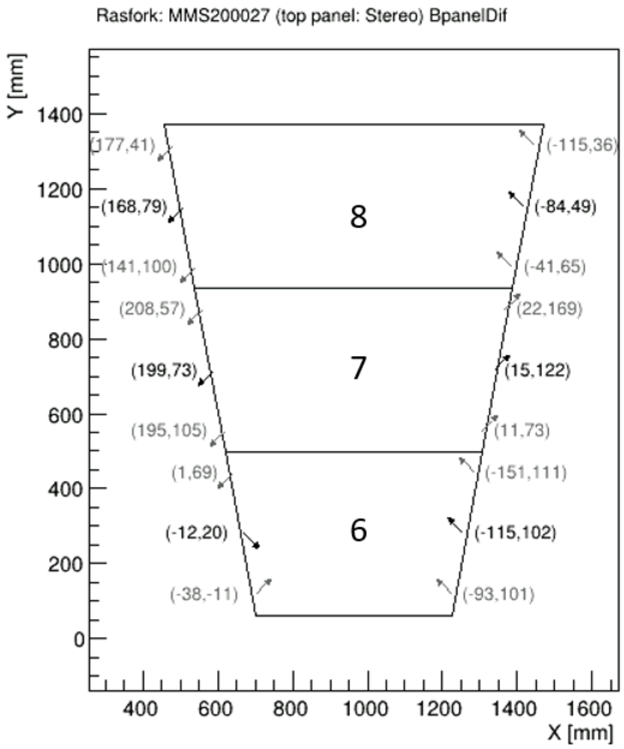

Fig. C.1: Four-fold Rasfork alignment results for the distortion between the two Stereo layers. Board 6 and 7 are strongly rotated. Board 8 of the Stereo in layer is shorter than the Stereo out board 8.

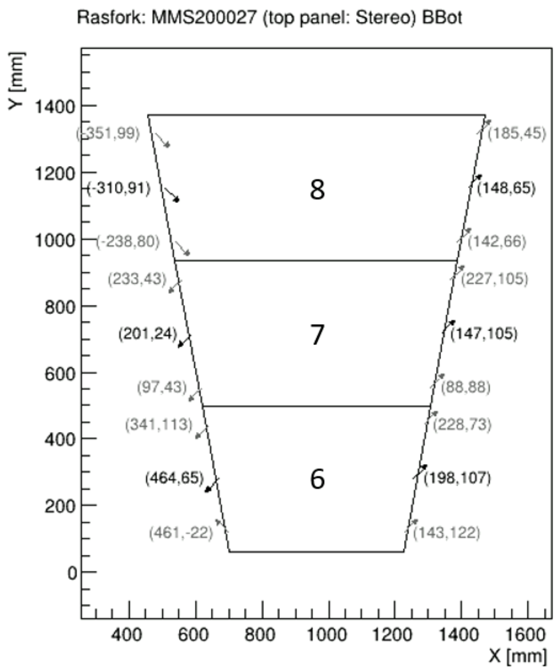

Fig. C.2: Alignment results of the four-fold Rasfork measurements. Measured is the alignment between the Eta in layer and the Stereo in layer. A rotation for board 7 is visible. Board 6 (left) shows a length difference between the two layers.

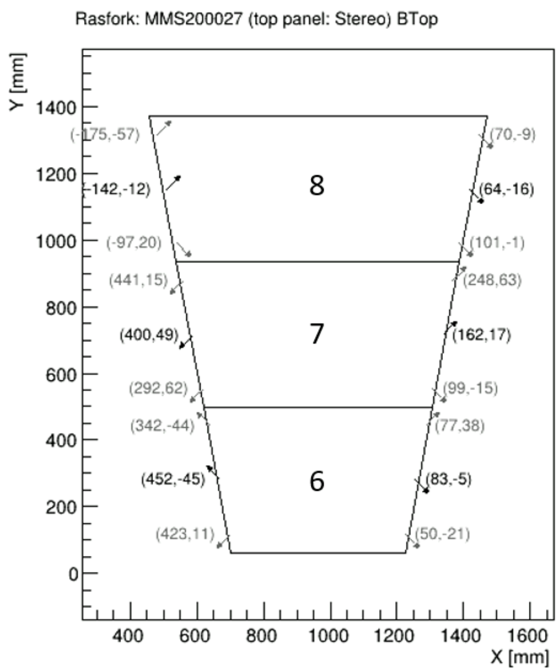

Fig. C.3: Alignment results of the four-fold Rasfork measurements. Measured is the alignment between the Eta in layer and the Stereo out layer. The left side of board 6 and 8 of the Stereo layer are shorter, the right side of board 6 and 7 are longer than the corresponding boards of the Eta layer.

Appendix D

CRF

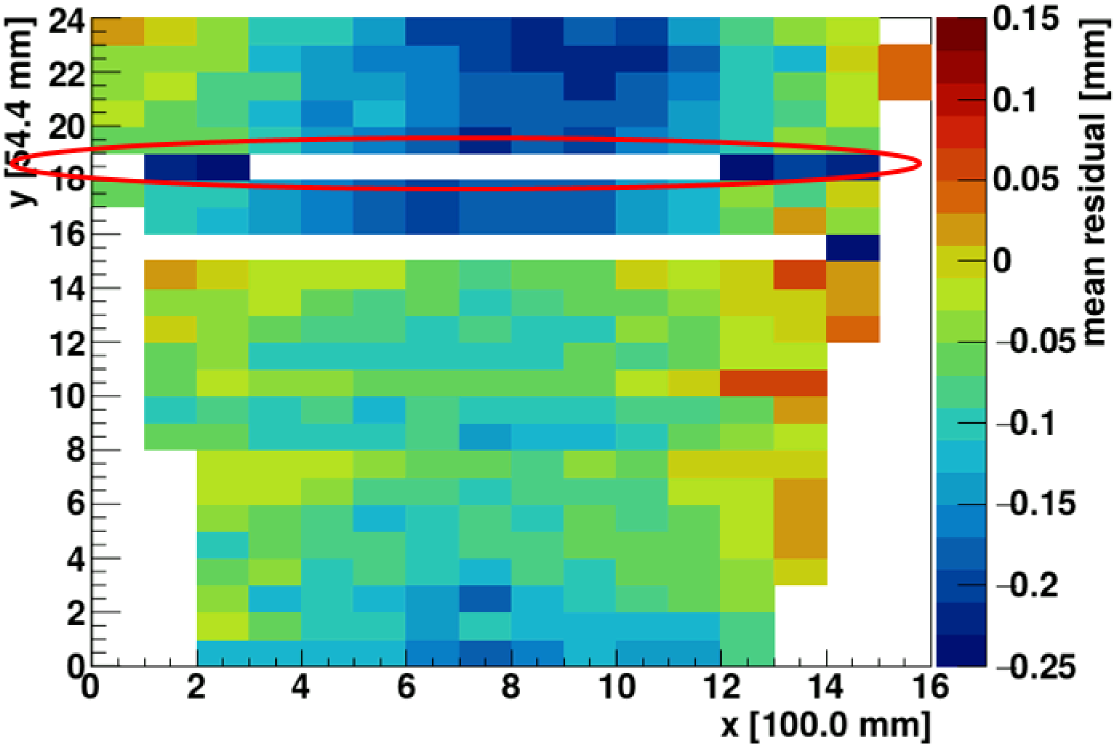

Fig. D.1: Residuals between the reconstructed position and the MDT reference track of the Eta_in layer of module 18. Board 8 shows similar shaped readout strips as the corresponding Eta_out layer (see fig. 5.4). Problematic readout electronics are visible for the y-slices 16 and 19.

Abbreviations

ATLAS	A Toroidal LHC ApparatuS
BSM	Beyond Standard Model
$C - CCD$	Contact-Charged Coupled Device
CMM	Coordinate Measuring Machine
CRF	Cosmic Ray Facility
FOP	Fiber Optical Plate
GS	Gluing Side
LHC	Large Hadron Collider
LED	Light-Emitting Diode
MDT	Monitored Drift Tube
Micromegas	Micro Mesh Gaseous Structure
MM	Micromegas Module
NSW	New Small Wheel
PCB	Printed Circuit Board
PMT	Photomultiplier Tube
Rasmask	Rasnik Mask
$SM2$	Small Micromegas 2

Bibliography

Alexopoulos, T. et al. (2011). „A spark-resistant bulk-micromegas chamber for high-rate applications". In: *Nuclear Instruments and Methods in Physics Research Section A: Accelerators, Spectrometers, Detectors and Associated Equipment* 640.1, pp. 110–118. ISSN: 0168-9002. DOI: `https://doi.org/10.1016/j.nima.2011.03.025`. URL: `http://www.sciencedirect.com/science/article/pii/S0168900211005869`.

Bianco, M. (2016). *Micromegas detectors for the muon spectrometer upgrade of the ATLAS experiment*. URL: `https://www.sciencedirect.com/science/article/pii/S0168900215014503` (visited on September 1, 2020).

CERN (2020a). *Calorimeters*. URL: `https://atlas.cern/discover/detector/calorimeter` (visited on September 1, 2020).

— (2020b). *Muon Spectrometer*. URL: `https://atlas.cern/discover/detector/muon-spectrometer` (visited on September 1, 2020).

— (2020c). *The HL-LHC project*. URL: `https://hilumilhc.web.cern.ch/content/hl-lhc-project` (visited on September 1, 2020).

— (2020d). *The Inner Detector*. URL: `https://atlas.cern/discover/detector/inner-detector` (visited on September 1, 2020).

Flierl, B. (2018). *Particle Tracking with Micro-Pattern Gaseous Detectors*. URL: `https://www.etp.physik.uni-muenchen.de/publications/theses/download/phd_bflierl.pdf` (visited on September 1, 2020).

Gillies, J. (2011). *Luminosity? Why don't we just say collision rate?* URL: `https://home.cern/news/opinion/cern/luminosity-why-dont-we-just-say-collision-rate` (visited on September 1, 2020).

Giomataris, Y., G. Charpak, et al. (1996). „MICROMEGAS: a high-granularity position-sensitive gaseous detector for high particle-flux environments". In: *Nuclear Instruments and Methods in Physics Research, Section A* 376, pp. 29–35.

Giraud, P.-F. (2017). *The RASFORK tool for checking MM alignment quality*. URL: https://indico.cern.ch/event/633240/contributions/2560619/subcontributions/230270/attachments/1469151/2275232/rasfork_PFG.pdf (visited on September 1, 2020).

Hashemi, K. (2007-2017). *Rasnik Analysis*. URL: http://alignment.hep.brandeis.edu/Devices/RASNIK/Analysis.html (visited on September 1, 2020).

Herr, W. and B. Muratori (2006). *Concept of Luminosity*. URL: http://cds.cern.ch/record/941318/files/p361.pdf (visited on September 1, 2020).

Herrmann, M. (2016). *Methods and Techniques for Construction of large area Micromegas*. URL: https://www.etp.physik.uni-muenchen.de/publications/theses/download/master_mherrmann1.pdf (visited on September 1, 2020).

— (2019). *Series Calibration of segmented and multi-layered Micromegas Modules for ATLAS*. URL: https://www.etp.physik.uni-muenchen.de/publications/theses/download/phd_mherrmann.pdf (visited on September 1, 2020).

Hertenberger, R. (2016). *Micromegas: Gaseous Micropattern Detectors*. URL: https://indico.ph.tum.de/event/3598/attachments/2078/2212/Hertenberger.pdf (visited on September 1, 2020).

Kawamoto, T. et al. (2013). *ATLAS New Small Wheel Technical Design Report*. URL: https://cds.cern.ch/record/1552862/files/ATLAS-TDR-020.pdf (visited on September 1, 2020).

Kleinknecht, Konrad (2005). *Detektoren für Teilchenstrahlung*. 4th ed. Teubner Studienbücher Physik. Vieweg+Teubner Verlag. DOI: 10.1007/978-3-322-82205-5.

Lide, D.R. (2003). *CRC Handbook of Chemistry and Physics, 84th Edition*. CRC HANDBOOK OF CHEMISTRY AND PHYSICS. Taylor & Francis. ISBN: 9780849304842.

Lösel, P. (2017). *Precision Calibration of Large Area Micro Pattern Gaseous Detectors*. URL: https://www.etp.physik.uni-muenchen.de/publications/theses/download/phd_ploesel.pdf (visited on September 1, 2020).

Müller, R. (2017). *Quality Control of Micromegas Detectors for the ATLAS New Small Wheel Upgrade Project and Opimization of the Spatial Resolution of PoSSuMuS Detectors in two Dimensions*. URL: https://www.etp.physik.uni-muenchen.de/publications/theses/download/phd_rmueller.pdf (visited on September 1, 2020).

Sampsonidis, D. (2017). *The ATLAS New Small Wheel Upgrade and the construction of Micromegas at AUTH*. URL: https://docplayer.net/48091222-The-atlas-new-small-wheel-upgrade-and-the-construc9on-of-micromegas-at-auth-sampsonidis-dimos-aristotle-university-of-thessaloniki-greece.html (visited on September 1, 2020).

Sidiropoulou, O. (2018). *Characterization of the ATLAS-type Micromegas Detectors*. URL: https://opus.bibliothek.uni-wuerzburg.de/opus4-wuerzburg/frontdoor/deliver/index/docId/16732/file/Sidiropoulou_Ourania_thesis.pdf (visited on September 1, 2020).

Steerenberg, R. (2018). *LHC Report: Protons: mission accomplished*. URL: https://home.cern/news/news/physics/lhc-report-protons-mission-accomplished (visited on September 1, 2020).

Stelzer, B. (2016). *The New Small Wheel Upgrade Project of the ATLAS Experiment*. URL: https://www.sciencedirect.com/science/article/pii/S2405601415006719 (visited on September 1, 2020).

Tanabashi, M. et al. (August 2018). „Review of Particle Physics". In: *Phys. Rev. D* 98 (3), p. 030001. DOI: 10.1103/PhysRevD.98.030001. URL: https://link.aps.org/doi/10.1103/PhysRevD.98.030001.

Vogel, F. (2017). *Studien zur optischen Ausrichtungsmethode für Myondetektoren beim ATLAS Detektor*. URL: https://www.etp.physik.uni-muenchen.de/publications/bachelor/download_auth_etp/bac17_fvogel.pdf (visited on September 1, 2020).

Danksagung

Abschließend möchte ich mich bei einigen Leuten bedanken, ohne die diese Arbeit nicht möglich gewesen wäre. Bei

- Herrn Prof. Dr. Otmar Biebel für die Möglichkeit meine Masterarbeit bei Ihm zu schreiben und das Korrekturlesen meiner Arbeit.
- Herrn Dr. Maximilian Herrmann für die exzellente Betreuung und Unterstützung über den kompletten Zeitraum meiner Arbeit und dafür, dass er immer ein offenes Ohr bei Fragen hatte.
- Herrn Dr. Ralf Hertenberger für das Korrekturlesen meiner Arbeit und die konstruktiven Anregungen.
- allen weiteren Mitgliedern des Hardwareteams, das während meiner Masterarbeit aus Dr. Bernhard Flierl, Christoph Jagfeld, Dr. Felix Klitzner, Katrin Penski, Maximilian Rinnagel, Sebastian Trost und Dr. Chrysostomos Valderanis bestand, für die durchwegs positive Atmosphäre und Hilfsbereitschaft bei jeglicher Art von Problemen.
- meinen Freunden Karl-Heinz, Maria, Patrick, Anna, Anka und Alina, die mich immer unterstützt und angetrieben haben und für viele unvergessliche Abende gesorgt haben.
- meiner Familie, die mir immer den Rücken freigehalten hat.

Erklärung zur Abschlussarbeit

Hiermit wird erklärt, dass die Arbeit mit obigem Thema selbständig verfasst und noch nicht anderweitig für Prüfungszwecke vorgelegt wurde. Weiterhin sind keine anderen als die angegebenen Quellen oder Hilfsmittel verwendet und wörtliche sowie sinngemäße Zitate als solche gekennzeichnet worden.

Ampfing, den 8. September 2020

____

Unterschrift